MULTISCALE ELECTRO-THERMAL MODELING OF AlGaN/GaN HETEROSTRUCTURE FIELD EFFECT TRANSISTORS

A Thesis
Presented to
The Academic Faculty

by

Fatma Nazli Donmezer

In Partial Fulfillment
of the Requirements for the Degree
Doctor of Philosophy in the
Woodruff School of Mechanical Engineering

Georgia Institute of Technology
December 2013

MULTISCALE ELECTRO-THERMAL MODELING OF AlGaN/GaN HETEROSTRUCTURE FIELD EFFECT TRANSISTORS

Approved by:

Professor Samuel Graham, Advisor
Woodruff School of Mechanical Engineering
Georgia Institute of Technology

Professor Srinivas Garimella
Woodruff School of Mechanical Engineering
Georgia Institute of Technology

Professor Satish Kumar
Woodruff School of Mechanical Engineering
Georgia Institute of Technology

Professor Douglas Yoder
School of Electrical and Computer Engineering
Georgia Institute of Technology

Professor John Cressler
School of Electrical and Computer Engineering
Georgia Institute of Technology

Date Approved: 11/11/2013

To my family:

Barış, Mom, Dad, and Hazal

ACKNOWLEDGEMENTS

First, I would like to express my deepest gratitude to my thesis advisor Dr. Samuel Graham for giving me the chance to fulfill one of my biggest dreams. Without his profound belief in my work, his valuable guidance, and patience this would not be possible. I would also like to express my deepest appreciation to my committee, for reviewing my work, giving helpful advice, and sharing their constructive criticism.

I am also grateful to Dr. Anusha Venkatachalam for supporting and mentoring me patiently whenever I needed her support. I will always remember her as a great mentor and friend. Also, many thanks to William James and Dr. Adam Christensen for their useful contributions to my research with their earlier work, valuable knowledge on field, and suggestions. Thanks should also go to Office of Naval Research and Schlumberger 'Faculty for the Future' program for their financial support.

I cannot leave Georgia Tech without mentioning the support of my friends Katie, Bana, David, Giray, Toby, Adrienne, Sarp, and Shweta. Also I had a great pleasure of working with past and present EMRL group members and would like to thank all of them for their insightful suggestions during our meetings.

I cannot begin to express my thanks to my mom, dad, and sister, for being patient and teaching me patience. Their faith in me, encouragement, and efforts to make me happy despite the thousands of miles between us is unforgettable. I cannot wait to be closer to them. Finally, I want to thank to love of my life, Barış. He helped me many times, in many ways to get through the most difficult journey of my life and made me realize that I am blessed to be no longer alone in my journey.

TABLE OF CONTENTS

LIST OF TABLES

LIST OF FIGURES

SUMMARY

There has been growing interest in AlGaN/GaN Heterojunction Field Effect Transistors (HFETs) that can operate in high power and high frequency applications. However, due to its large phononic band gap and the Fröhlich interaction of electrons with high energy polar optical phonons, intense heating and a phonon bottleneck occurs that impacts the ability to dissipate heat locally near the transistor's gate. Thus, an intense hotspot occurs which can impact the overall device reliability. While numerous studies have modeled AlGaN/GaN transistors to estimate the hotspot temperature, little attention has been given to the phonon transport physics which occurs in the devices. In general, these models fail to capture ballistic-diffusive phonon conduction which can result in an elevated temperature rise that is not predicted by other models used to analyze AlGaN/GaN HEMTs. Such models will provide greater insight into the thermal transport process and thermal response of the self heating of these technologically important devices.

To build a thermal model that will capture these ballistic effects, first the methods that can be used for phonon transport modeling were presented. Later, the appropriate method was picked by comparing the performance of two common methods using a gray approximation in ballistic to diffusive regimes. After the method was chosen for the ballistic-diffusive thermal simulations, a multiscale model was suggested. This multiscale model allows modeling geometries other than the die while still including the ballistic effects at the hotspot with reasonable computational cost. In the meantime, a non-gray approach that included the effects of the different relaxation times and the thermal conductivities of phonon modes in the crystal was introduced.

Later, using this multiscale electro-thermal model, device simulations at different biasing conditions were performed on two-finger HFETs grown on SiC substrates and mounted on RF packages. To obtain the Joule heating distribution that might have an impact on device temperature, electrical simulations were performed using hydrodynamic and Monte Carlo simulations. After the electrical Joule heating distribution was obtained, it was used in gray and non-gray multiscale thermal simulations and the temperature distribution within the device and the hotspot was obtained.

With this thesis, an electro-thermal approach to investigate the ballistic-diffusive nature of the heating in AlGaN/GaN HFETs is presented as well as the impact of electrical bias conditions on the heat generation distribution. This effort is the first to employ such a scheme for the analysis of AlGaN/GaN devices for temperature modeling. Finally, this method allowed us to capture the deviation from purely diffusive transport. In general, this deviation lasted over 5 to 10 μm around the device and the temperature deviation ranged from 5K to 50K at the maximum point depending on the mean free path of phonons, power density, and the biasing condition.

CHAPTER I

INTRODUCTION

1.1 AlGaN/GaN Heterostructure Field Effect Transistors

AlGaN/GaN Heterostructure field effect transistors (HFETs) or high electron mobility transistors (HEMTs) are technologically important devices for high power and frequency applications [18, 19]. As a result, these devices are frequently used for high performance radars, commercial ground base stations, satellite communication, and high power switches to name a few applications [20, 21]. Their high power handling capability is due the superior material properties of GaN compared to other semiconductors. The material properties of GaN, GaAs, Si and SiC are listed in Table 1. Gallium nitride has a high thermal conductivity (k=150W/mK), which enables more effective heat removal from active regions. Moreover, it has high critical breakdown field(3MV/cm) as a result of its wide band gap(3.4eV). Breakdown occurs in a material when the electric field is strong enough to liberate electrons or holes from the atoms of the semiconductor crystal. This causes the surge in the current that eventually leads to device burn out. Thus, a large breakdown field is always desirable if higher voltages are applied over very small dimensions as in the case of HFETs[18].

The high frequency capabilities of AlGaN/GaN HFETs are attributed to the characteristics of the AlGaN/GaN heterojunction which is formed by pseudomorphic growth of AlGaN on GaN layers. Properties that allows high frequency operations

Table 1: Material Characteristics of GaN, Si, Sic, and GaAs.

Characteristic	Unit	GaN	Silicon	GaAs	SiC
Thermal Conductivity	W/mK	>150	150	50	450
Bandgap	eV	3.49	1.1	1.42	3.26
Critical Breakdown Field	MV/cm	3.0	0.3	0.4	4.5

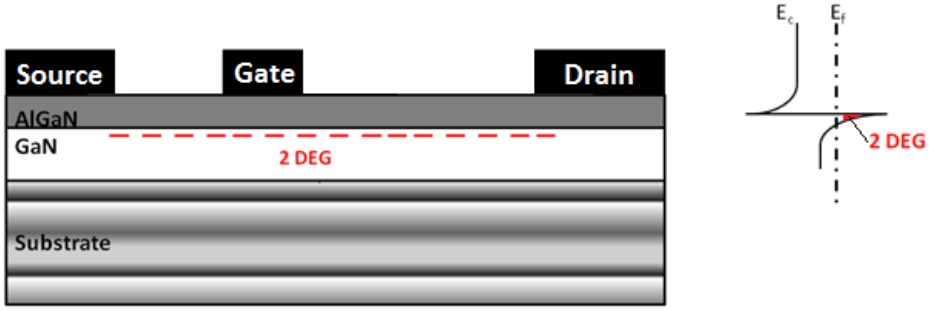

(a) (b)

Figure 1: (a)Schematic of an AlGaN/GaN HFET and the 2DEG formation. (b)Band diagram at the interface.

such as high sheet charge density and the electron mobility are attributed to this heterojunction. A typical AlGaN/GaN transistor, as shown in Fig. 1(a), is formed from a thin layer ($\sim 30nm$) of AlGaN deposited on a thicker ($\sim 2-3\mu m$)GaN. These layers form a very unique junction due to their band gap difference and spontaneous piezoelectric polarizations.

As shown in the band diagram given in Fig. 1(b) the electrons in the AlGaN layer move into the GaN layer with lower conductive energy band and they become trapped in the quantum well which is formed at the GaN side of the heterojunction [1]. This one-dimensional confinement of electrons generates a two-dimensional electron gas structure (2DEG) with sheet carrier concentrations $10^{13}cm^{-2}$ or higher [3].

The high spontaneous and piezoelectric polarizations in wurtzite GaN and AlN are responsible for the significant increase of sheet carrier concentration[3]. Figure 2 shows the crystal structure of wurtzite Ga- and N-faced GaN grown along a direction normal to the 0001 basal plane. Depending on the type of the atom (Ga or N) present at the basal plane crystal is a given one of the names Ga- or N-faced.

Figure 3 is the schematic representation of the polarizations and the polarization induced sheet charge density in Ga- and N-faced AlGaN/GaN heterostructures. The polarity of the Ga- or N-faced wurtzite GaN's are different. Moreover, as shown in the

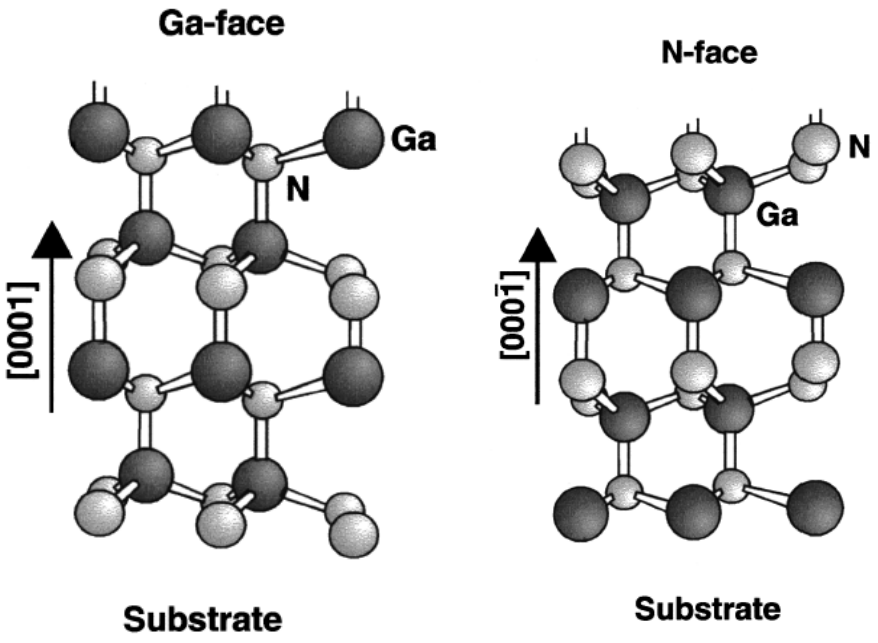

(a) (b)

Figure 2: Schematic drawing of the (a)Ga-face and (b)N-face wurtzite GaN crystal[3].

Fig. 3 the spontaneous and piezoelectric strain are found to be parallel when AlGaN layers are under tensile strain. Therefore, the total polarization in the AlGaN layer can be found by adding these two polarizations. Moving from AlGaN to GaN polarization change and a gradient of polarization is observed. This gradient is responsible for polarization induced charge density given as $\sigma_P = \nabla P$ [3]. If the polarization induced sheet charge density is positive ($+\sigma$) then electrons move to heterojunction to compensate this charge, later move to the GaN layer due to the bandgap difference to form 2DEG. For AlGaN/GaN HFETs the polarization gradient is found to be high, thus the sheet carrier density. Electrons in 2DEG move much faster than electrons in silicon transistors since they experience very little impurity scattering due to the undoped GaN layer.

When a positive voltage is applied to the drain VDS>0, the electrons in the 2DEG region move, thus devices are normally ON unless a negative gate voltage VGS<0 is applied to them. A negative gate voltage creates a depletion region in

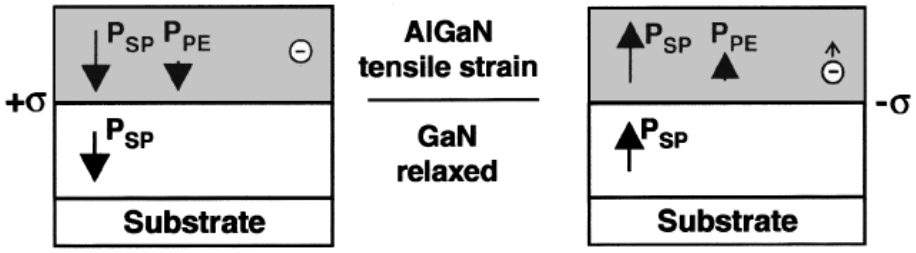

(a) (b)

Figure 3: Directions of the spontaneous and piezolectric polarization and polarization induced charge density in (a)Ga-face and (b)N-face AlGaN/GaN heterostructure (AlGaN under tensile strain)[3].

the channel that hinders the electron movement. When the gate voltage is below a certain threshold, the depletion region is big enough to block the entire electron movement. Thus, the device is OFF or in a state called "pinch-off" condition. As a result, the power output and electrical performance of a given AlGaN/GaN HFET depends on the combination of drain and gate voltages. The typical current voltage characteristic of an AlGaN/GaN HFET is given in Fig. 4(a).

For both the fresh and degraded devices, as the gate voltage increases the current output at a given drain voltage also increases. When the device is ON and the drain voltage is low, the device current voltage relationship is linear. This region, where the device current changes linearly due to changing drain voltage, is the linear region. As the drain voltage increases, the relationship between the current and the voltage is no longer linear and the current reaches a plateau. This region is called the saturation region and the drain voltage at the start of this region is called the knee voltage V_{knee}.

Velocity saturation due to high electrical fields is the main reason of the device saturation. Devices should exhibit low resistance and high saturation current characteristics to operate at high powers. Both the saturation current and the resistance are strongly affected by the temperature. The saturation current is a strong function

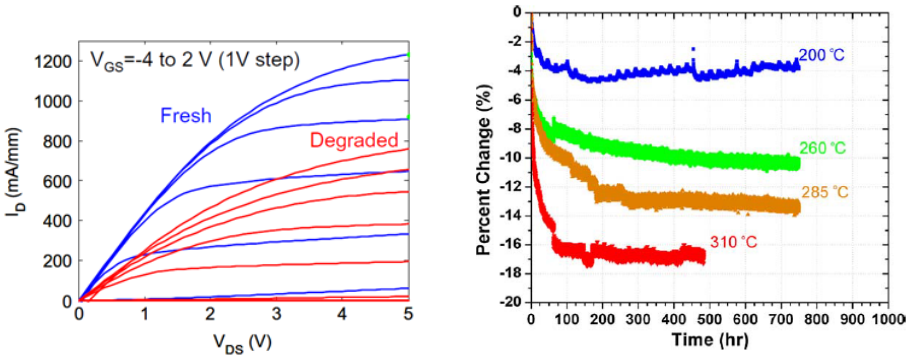

(a) (b)

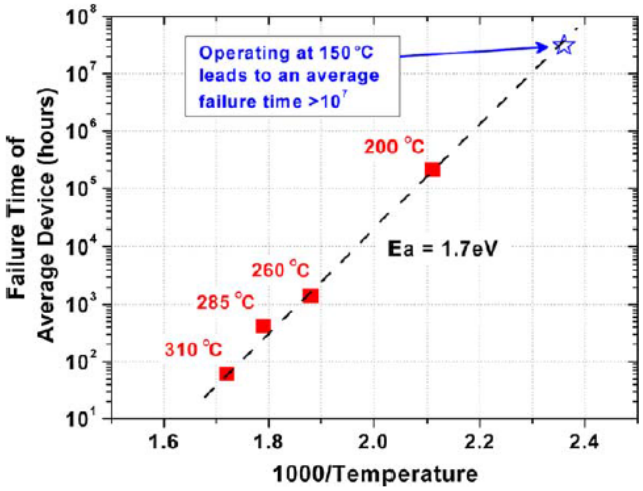

(c)

Figure 4: (a)Current voltage characteristics of fresh and degraded devices[4]. (b)Drain current percent change of GaN-on Si HEFTs with respect to time during a DC current stress test at different junction temperatures[5]. (c)Average device failure time with respect to inverse junction temperature[5].

of saturation velocity which decreases due to increasing frequency of electron scattering at high temperatures. Device resistance is determined by the carrier mobility which decreases with temperature too. Figure 4(b) shows the percent change of drain current with respect to time at different temperatures. Although these devices can withstand temperatures as high as 200 °C, it is observed that as the temperatures increase, the device performance, in this case drain current, decreases due to decreasing carrier mobility with temperature. Therefore, to achieve high performance devices that have high power output, high temperatures should be avoided.

1.2 Reliability Issues of AlGaN/GaN HFETs

Although AlGaN/GaN HFETs are very promising, their limited reliability is still a concern [22]. Figure 4(a) also illustrates the electrical performance difference between a fresh and a degraded device. To explain this behavior, electrical reliability studies have focused on the degradation mechanisms of these devices. An important degradation mechanism is the defect formation caused by the high electrical field present in the devices[23]. These defects act as traps for electrons and cause a phenomenon called current collapse [24, 25]. Current collapse in a device reduces the maximum drain current, which is also known as the saturation current, increases the knee voltage and the gate leakage current[22, 26, 23]. This effect is seen in degraded devices whose electrical performance is shown in Fig.4(a). Degraded devices have reduced overall microwave power and increased resistance. Thus, current collapse can be considered as one of the reasons for the limited reliability of these devices.

Crystallographic defect or trap formation under high electric fields can be partly explained by the inverse piezoelectric effects on high piezolectric GaN and AlGaN materials[27]. That is, under high voltage, large stresses can be induced in devices. It has been observed that high stresses generated by high voltages produce active defects in the AlGaN barrier in the vicinity of the gate edge. Even more, a number

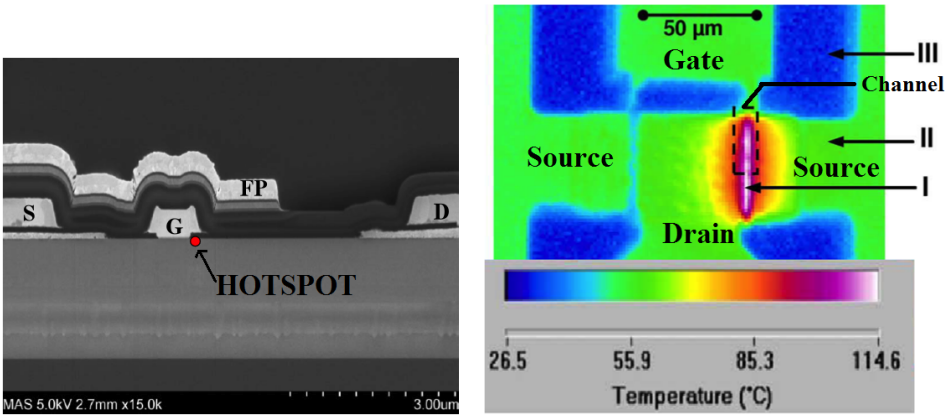

(a) (b)

Figure 5: (a)The SEM image of the cross section of an AlGaN/GaN HFET(hotspot location is marked on the image)[6].(b)The micro-Raman temperature map of the surface of an operating device. Numbers represent (I)hotspot, (II)area covered by metal contacts, and (III)area free from metal contacts[7].

of studies have shown cracking and pit formation in the AlGaN layer are caused by the inverse-piezoelectric effect[28].

Crystallographic defects causing gate leakage can also be generated due to other factors. For instance, the surface defects that are inherent in material surface can act as traps and cause high gate leakage current [29, 30]. This effect can be reduced by depositing a passivation layer under the metal gate electrode to fill the surface defects [31, 32].

Although the dominant effect causing the device degradation is not well known thermal effects are extremely important since they contribute not only to mechanical stresses but also to chemical reactions and electron transport changes in the devices. The effect of temperature on the reliability of devices can be seen in Fig.4(c) where the mean time to failure is shown with respect to junction temperature. These thermal effects, which are very intense near the gate of the AlGaN/GaN HEMTs, result in the acceleration of device degradation and are thus a concern for their use in various applications. Figure 4(c) shows that a temperature increase of 50 to 60 C can cause a 2 to 3 order of magnitude decrease in the lifetime of these devices. Thus, relatively small

changes in device operating temperature can greatly impact the expected reliability and remains a concern in the thermal management of these HFETs.

The hotspot of an AlGaN/GaN HFET initiates in the 2DEG region and is located under the drain side edge of the gate. The location of the hotspot is marked on the SEM image of the cross section of a typical HFET in Fig.5(a). In Fig.5(b), the infrared temperature map of an operating device, shows the localized heating within the device channel.

Formation of hotspots is due to localized Joule heating along the gate edge caused by the high electric field gradients. The electric field changes rapidly in this region due to the formation of the depletion region. The device current is controlled by the depletion region whose size is controlled by the gate voltage. When the depletion region is large, the electrons have to pass through a narrower region (i.e. high electrical field gradients) and gets accelerated. These hot electrons are the cause of the localized Joule heating of the devices.

Localized heating in the device starts with the Fröhlich interaction of electrons with high-energy crystallographic lattice vibrations (i.e., phonons). These vibrations, along with other crystallographic vibrations help diffusion of heat away from the hotspot. However, for GaN the extremely small size of the heat generation region, which can be on the order of 50nm[1] and the slow energy transfer between different types of vibtations slows down the heat removal process. This impacts the ability to dissipate local heat near the transistor gate causing the high temperatures of the hotspot [33].

To design and produce highly reliable AlGaN/GaN HFETs that will overcome these heating problems electrical, thermal, and mechanical modeling are extremely important. In general, focus has been placed on fully coupled electro-thermal simulations [34, 35, 36, 37] which aim to understand the effect of temperature on the electrical performance of the devices. However, these models fail to accurately predict

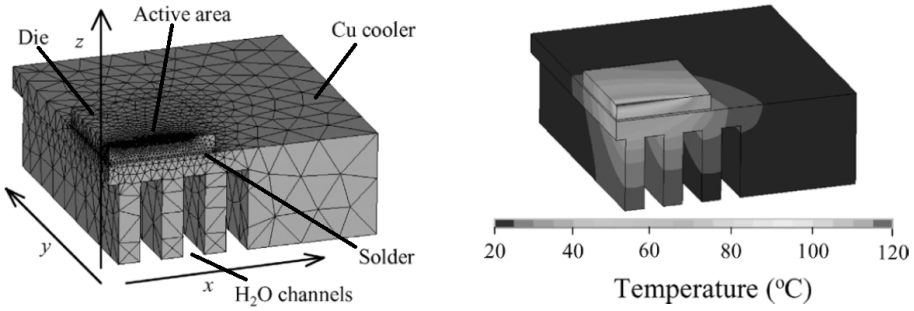

(a) (b)

Figure 6: (a)Finite element mesh for the SiC die on a copper microchannel cooler configuration (due to symmetry only 1/4 of the geometry is shown). (b)Temperature distribution when the power density is 5W/mm and gate spacing is $50\mu m$ [8].

the hotspot temperature and its effect on electrical performance due to two reasons. First, some of these thermal simulations only concentrate to the active region and do not include the additional thermal effects of outer geometries such as the substrates, package, heat sink, etc. Moreover, they use Fourier's diffusion equation in the entire lattice that is modeled and ignore the ballistic phonon effects.

For example, Calame et al. investigated the cooling effects of a copper microchannel heat sink on the devices using a finite element solution of Fourier's diffusion equation to model the temperature distribution in devices[8]. Figure 6 presents the finite element mesh used to model the temperatures of a microschannel cooled device and the associated results. Although, such works are improvements to simple electrical performance studies by including other thermal effects the ballistic effects have been ignored by using Fourier's diffusion equation. Although, recently more detailed analysis including coupled electro-thermal-mechanical analysis of devices has been performed in literature[38], similar to the previous models they neglect the ballistic thermal effects.

In GaN HFET depending on the biasing conditions, the size of the hotspot can vary and can have critical dimensions on the order of 50nm [1]. This is much

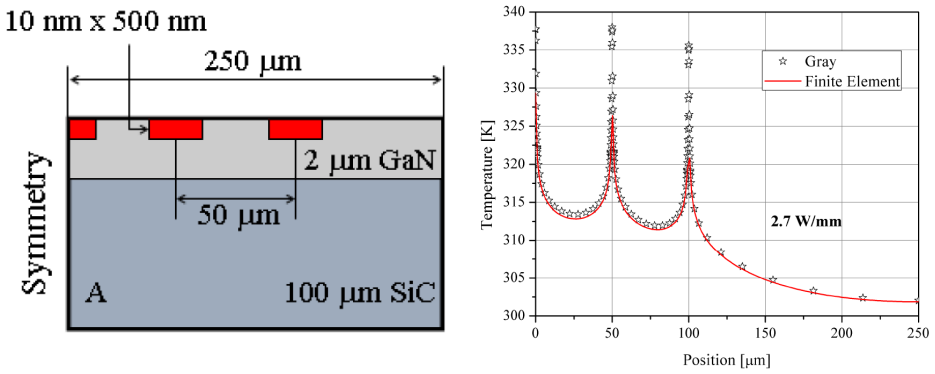

(a) (b)

Figure 7: (a)Geometry of the 6 finger device modeled using ballistic diffusive techniques (only half of the device is shown due to symmetry). (b)Temperature distribution along the surface of device operating at 2.7W/mm [9].

smaller than the mean free path(Λ) of dominant energy carriers, lattice vibrations (i.e. phonons), in GaN. Localized heating from heat generation sources smaller than the phonon mean free path in silicon devices have been investigated and found to be the reason of increased device temperatures due to the ballistic heat transport effects they generate[39], but no such studies have been performed in GaN devices.

Overall, this effect can not be observed using Fourier's diffusion approximation. To understand the thermal transport in such small scales it is necessary to use thermal models accounting for ballistic diffusive phonon transport in devices. There were several attempts to model the ballistic effects at the hotspot of AlGaN/GaN HFETs[9, 40]. Figure 7 shows a 6 finger device modeled using ballistic-diffusive phonon transport and Fourier's diffusion equation as well as the comparison of temperature results along the surface. As evident from Fig.7(b), higher temperatures were observed at hotspots when ballistic-diffusive effects were included in the thermal simulations.

Even though there were several attempts in the literature, a coupled electro-thermal model where the thermal transport is addressed using multi-scale thermal models accurately accounting for ballistic-diffusive phonon transport in the devices

has not been presented[41]. These models are important for device reliability studies since they can provide a better estimate of the hotspot temperature using a sub-continuum approach coupled to the macroscopic heat transfer equations.

1.3 Motivation and Objective

The first objective of this study is to investigate numerical techniques that will allow for the modeling of ballistic-diffusive phonon transport in AlGaN/GaN HFETs using gray and non-gray models. The second objective is to build up a multiscale thermal model that can model the ballistic-diffusive phonon transport near the device channel while still capturing the diffusive transport in the remainder of the device to provide more accurate temperature predictions of AlGaN/GaN HFETs. The third objective is to combine the multiscale thermal model with an electrical model to create a coupled electro-thermal model accounting for multiscale transport effects in devices and to investigate the impact of the substrate, the device geometry, and the biasing conditions on the heating of the devices.

1.4 Outline of Thesis

This thesis is outlined in five main sections. Chapter 2 covers the electron and phonon physics associated with the Joule heating in AlGaN/GaN HFETs. First, the experimental studies and decay rates of electron to phonon relaxation processes are summarized in this section. Later, different phonons in GaN are discussed using a phononic dispersion curve. Moreover, the interaction of phonons with different phonon modes during the Joule heating process are discussed. Finally, the need for phonon transport modeling is highlighted and several simplifications used for phonon transport modeling are discussed.

In Chapter 3, the two popular numerical techniques: Lattice Boltzmann and Discrete Ordinates methods, used for the solution of the phonon Boltzmann transport equation (BTE) are explained. The performance of these two methods are compared

for 1D and 2D problems in ballistic to diffusive regimes using a gray approximation. At the end of this comparison, appropriate method to be used for device simulations is determined.

The non-gray approach that includes the effects of interaction between phonons and their intrinsic relaxation times in the phonon BTE solutions is constructed in Chapter 4. This is done by finding the individual scattering strength of phonon modes, splitting the phonon dispersion into bands and calculating the band to band interaction strengths using these individual scattering strengths.

Chapter 5 discusses the multiscale model that can be used for thermal simulations of the devices with more realistic boundary conditions and larger device geometries. In this chapter a closer inspection of the region where ballistic phonon transport is significant is performed. Some dimensional effects, such as the size of the heat generation region with respect to phonon mean free path and proximity of a boundary on ballistic phonon transport are analyzed using gray multiscale model.

In Chapter 6, multiscale device simulations are presented. The electrical device simulations that provide the energy relaxation distribution in active devices are summarized. The effects of multi-fingered devices, the biasing conditions, substrate, and package on the hotspot temperature of the device are investigated using a gray and non-gray multiscale models presented in previous chapters.

The final portion of this thesis, Chapter 7, summarizes the findings of this thesis and discusses future research directions.

CHAPTER II

LOCALIZED JOULE HEATING IN AlGaN/GaN HFETS

Localized hotspots are recognized as one of the most significant concerns for device reliability. These hotspots, which have dimensions on the order of a few tens to hundreds of nanometers in certain directions are created due to the localized Joule heating in devices. Joule heating is the name given to the energy exchange between the electrons and the lattice. The hotspot temperature is strongly affected by these complex energy decay mechanisms and the size effects caused by the extremely small size of the domain where these interactions take place. In this chapter the physics of the energy decay mechanisms between the carriers is discussed.

2.1 Dominant Energy Carriers in GaN: Phonons

Bulk Gallium Nitride crystal is thermodynamically stable in the wurtzite structure shown in Fig.2. Wurtzite is the name given to the crystal structure of various binary compounds in hexagonal shape. The dominant energy carriers in GaN are lattice vibrations (i.e. phonons). The total number of phonon modes in GaN is 12. Three of these phonon modes are acoustic phonons: 1 longitudinal (LA) and 2 transverse (TA). Rest of these phonon modes are optical: 6 transverse (TO) and 3 longitudinal (LO). The phonon dispersion curves for bulk wurtzite GaN is shown in Fig.8.

The dispersion plot gives the frequency and wavevector relationship of phonon modes in the crystal. The wavevector axis (x-axis) of the dispersion curve is marked with letters representing the vertices of the irreducible Brillouin zone shown in Fig.9. Γ represents the zone center where the wavevector, $\mathbf{k}$ is equal to zero. Acoustic phonons can be easily identified in the dispersion curve since they have zero frequency (energy) at $\mathbf{k}$=0. Phonon modes in GaN are represented by special names. A1 and

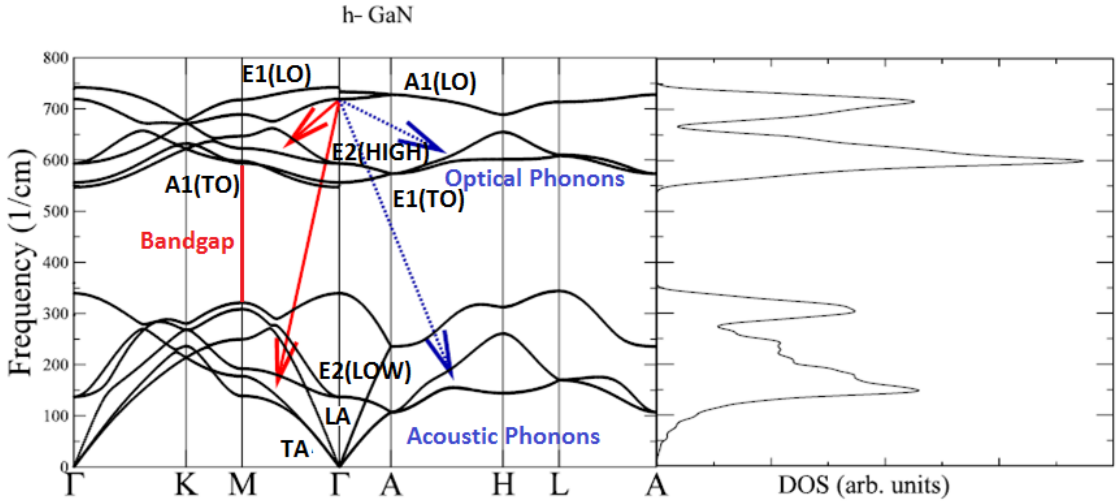

Figure 8: Phonon dispersion and density of states in wurtzite GaN (Ridley channel, which is the most common decay channel is also shown by arrows.) [10].

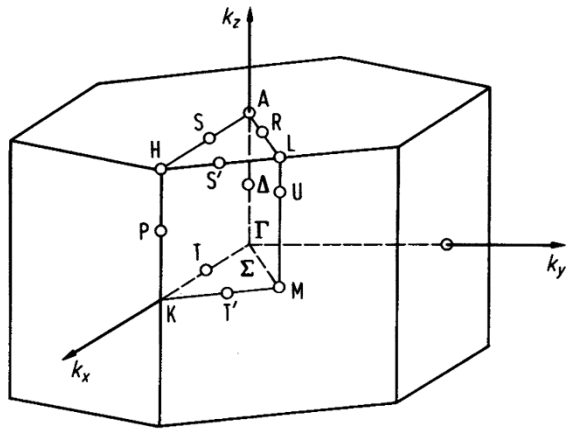

Figure 9: Brillouin and Irreducible Brillouin zone of wurtzite GaN.

E1 are the longitudinal and transverse acoustic modes respectively. A1, B1(low), and B1(high) are longitudinal acoustic modes. E1(TO), E2(low), and E2(high) are the transverse optical modes. At the zone center only 8 phonons are visible since all the transverse phonons are degenerate at this point.

2.2 Electron-Phonon and Phonon-Phonon Scattering

Electrons in the 2DEG region of an AlGaN/GaN HFET go through different scattering mechanisms depending on their energies. This energy is strongly related to the

electrical field distribution in the device that is responsible for the kinetic energy of electrons. The accelerated electrons are often called hot electrons and get scattered by crystal defects, other electrons, and phonons. The strength of the energy decay from electrons to the lattice is determined by the strength of these electron-phonon scattering events. Therefore to understand the Joule heating occurring in these devices electron-phonon scattering should be understood.

The scattering events between the electrons and phonons depends on the kinetic energy of electrons. The hot electron energy relaxation studies show the ultrafast response of electrons to the applied electric fields with extremely short relaxation times [42]. Other than cryogenic temperatures under moderate and weak electric fields electron-phonon energy relaxation occurs through high energy longitudinal optical (LO) phonon emissions [42]. The LO phonon emission rate measurements and calculations at room temperature revealed the ultrafast relaxation time not exceeding 0.4ps [42, 43, 44].

As soon as the first LO phonon emitted by hot electrons, energy is deposited into the lattice and the heat transfer in the crystal begins. Although the LO phonon emission is extremely fast LO phonon relaxation is relatively slow. Optical phonon relaxation can occur through one of the below channels:

$$\text{Ridley: } Optical \rightarrow Optical + Acoustic$$

$$\text{Klemens: } Optical \rightarrow Acoustic + Acoustic$$

$$\text{Barman-Srivastava: } Optical \rightarrow Optical + Optical$$

The dominant decay routes of optical phonons in group-III nitrides have been investigated both experimentally and theoretically. In general, optical phonons in GaN follow the Ridley channel and decay into an optical mode of a lower branch and an acoustic mode, as shown by the arrows in Fig.8. This is due to the large phononic bandgap which prevents the decay of high energy LO phonons from decaying directly into acoustic phonons via the Klemens decay channel. The cation to anion mass ratio,

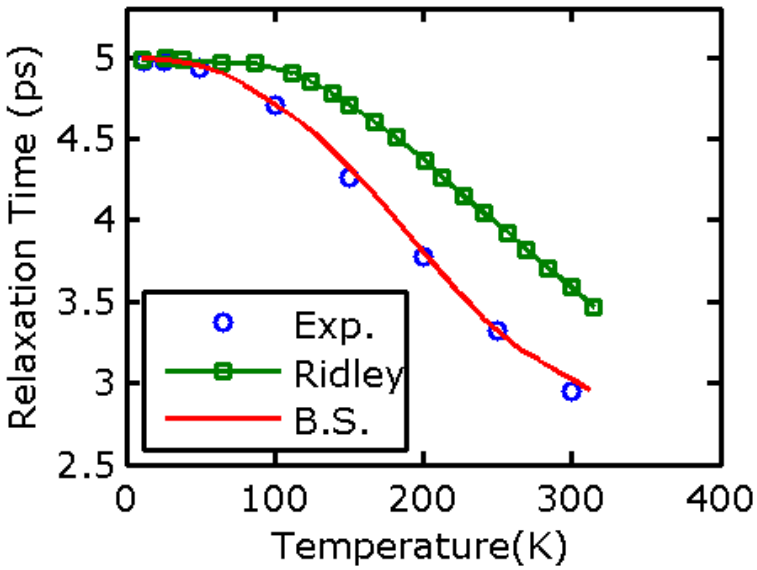

Figure 10: Experimental (shown by circles) and theoretical lifetime variations of A1(LO) phonons in Ridley (shown by squares) and Barman-Srivastava(B.S.) channels with respect to temperature[11].

which is responsible for the energy difference between upper and lower optical and acoustic phonons is responsible for this decay route in GaN. For GaN this ratio is $m_{Ga}/m_N = 4.98$ which is high enough to avoid decay into two acoustic modes through Klemens channel but not high enough to favor decay in two optical phonons through Barman-Srivastava channel [10].

Temperature dependent lifetimes of A1(LO) phonons obtained experimentally and theoretically are shown in Fig.10. Optical techniques such as photoluminescence and time resolved Raman give the relaxation time of LO phonons in GaN as 3-4 ps at room temperature [30, 11]. Since the relaxation of LO phonons is not as fast as the electron relaxation a bottleneck is formed causing energy accumulation in the LO phonon modes. As a result of the high energy of LO phonons, electron scattering rates increase that end up decreasing the drift velocity of electrons in the channel. Such hot phonon effects are undesirable due to their negative effect on the electrical performance of AlGaN/GaN HFETs[30].

2.3 Size Effects of Localized Joule Heating

The ballistic effects caused by the extremely localized heat source in silicon devices has been a popular problem in silicon industry over the years. The motivation to build smaller devices[45] has been the driving factor for detailed investigation of the size effects on thermal properties of devices. Ballistic effects were observed in devices having extremely small heat source regions in the past. These effects were attributed to the physical size of the heat generation region where neither the physical boundaries of the system nor impurities contribute to ballistic scattering of phonons[46, 47].

When the heat source is small in size, the phonons propagating through this region cannot scatter or exchange energy with the high energy phonons generated inside this region effectively. As a result, heat removal from the heated region is slowed down and the thermal conductivity is reduced. Therefore, such ballistic transport effects are responsible for higher temperatures in devices.

In order to observe this effect, the size of the heat generation region should be comparable or smaller than the mean free path of phonons of the semiconductor[48]. The heat carrying phonons in silicon have mean free paths in the range of 40-300nm[48]. Thus any heat source with a size on the order of a few tens of nanometers will lead to ballistic behavior of phonons as observed in previous studies performed on Si devices[46, 47].

For wurtzite GaN it has been experimentally shown that 50% of the heat is carried by phonons with mean free paths larger than 500nm [9].Thus, the localized heating in AlGaN/GaN HFETs which can be as small as 50nm [1] will cause the ballistic effects and should be included in thermal simulations. However, such effects cannot be simulated using Fourier's diffusion theory which assumes instanteneous propagation of heat and that no delays from such energy exchange between propagating modes exists.

2.4 Modeling Phonon Transport

In order to simulate the size effects and the electron-phonon and phonon-phonon scattering events in devices, phonon transport should be modeled. The approaches that can be used for the microscopic study of phonon transport are listed as: molecular dynamics simulations, atomistic green's function and the solution of phonon Boltzmann transport equation.

2.4.1 Molecular Dynamics

In classical molecular dynamics simulations Newton's equations of motion are solved numerically for all the atoms or molecules in the system. Interatomic potentials couple the equations of motions of different atoms or molecules. Inaccurate interatomic potential might lead to erroneous results even the solution is numerically accurate. Another drawback of the molecular dynamics simulations is their computational burden.

2.4.2 Atomistic Green's Function

Non-equilibrium Green's function is initially developed to simulate electron ballistic transport[49]. Later, an approach is presented for the atomistic study of phonon transport in real dielectric nanowires via Green's functions [50, 51]. Green's functions are used to determine the solutions of linear operators, $\mathbf{L}[\mathbf{u}] = 0$. System of equations of motion of atoms in a chain is an example of such linear operator. Green's function solution, $\mathbf{g}$, is the solution that is obtained as a result of a perturbation, $\boldsymbol{\delta}$, to the problem, $\mathbf{L}[\mathbf{g}] = \boldsymbol{\delta}$.

Similar to molecular dynamics simulations interatomic potentials and equilibrium positions of the atoms are required for these simulations. Moreover, although these simulations are performed well for the thermal modeling of monoatomic or diatomic chains, they will not be practical for more complex and bigger systems.

2.4.3 Phonon Boltzmann Transport Equation

The phonon Boltzmann transport equation is used to solve for the phonon distribution function when phase coherence effects are unimportant [52, 53]. Phonon BTE describes the rate of change of the statistical distribution function for phonons and is given as [54]:

$$\frac{\partial f}{\partial t} + \vec{v} \cdot \nabla f = \left(\frac{\partial f}{\partial t} \right)_{scatt} \tag{1}$$

here f is the phonon distribution function, $\vec{v}$ is the phonon group velocity based on the dispersion relationship. The scattering term on the right hand side represents the change in particle distribution function due to the energy carrying particle collisions with other phonons, isotopes, electrons, crystal defects and boundaries. The distribution function f, is a function of the phonon position, direction, frequency, and polarization. Therefore, solution of Eq.1 is not straightforward and even computationally expensive. As a result of this, several approximations have been made and computationally less expensive methods have been suggested. The phonon Boltzmann transport equation has been solved for the thermal modeling of semiconductors using some of these approximations in the past [55, 46, 56]. The approximations used for the solution of the phonon BTE are explained next.

2.4.3.1 Ballistic-Diffusive Equations

The essence of the ballistic-diffusive approximation is to divide the distribution function at any internal point into two parts, one that originates from the boundaries (f_b) and one from rest of the carriers at this point f_m. The phonon BTE is solved for the ballistic part (f_b) and the modified hyperbolic heat equation is solved for the carriers scattered from other internal points (f_m). However, it is shown that the performance of the ballistic-diffusive equations is poor when used for domains with internal nanoscale heat source [48].

2.4.3.2 Gray Model

The gray model is the simplest of all phonon models. In the gray model, all phonons are grouped into a single phonon group with a single group velocity v_g. In the gray model, first Eq.1 is changed into an energy density form:

$$\frac{\partial e}{\partial t} + \vec{v_g} \cdot \nabla e = \left(\frac{\partial e}{\partial t}\right)_{scatt} \tag{2}$$

The energy form of Eq.1 is obtained by replacing the distribution function with integrated phonon energy density based on the Eq.3[52]:

$$e(T) = f\hbar\omega D(\omega) \tag{3}$$

In Eq.3, f is the phonon frequency, $\hbar$ is the reduced Planck's constant and $D(\omega)$ is the phonon density of states. The integrated energy density, e, is a function of spatial position and direction but not of the wavevector and the polarization. Now the dispersion information is lost and the phonon BTE given in Eq.2 is solved for only one type of phonon with a group velocity of $\vec{v_g}$.

Relaxation time approximation is often used to simplify the scattering events of phonons represented by the right hand side of 2. In this approximation, it is assumed that phonons out of equilibrium with energy density e relax into equilibrium energy, e_0, in a given time, τ. Under the relaxation time approximation, Eq.2 takes the form:

$$\frac{\partial e}{\partial t} + \vec{v_g} \cdot \nabla e = \frac{e - e_0}{\tau} + q''' \tag{4}$$

Using the constant specific heat assumption, equilibrium energy density, e_0 can be related to the lattice temperature as:

$$e_0 = CT \tag{5}$$

Using the kinetic theory phonon properties can be related to bulk thermal conductivity of the material in the diffuse regime as:

$$k = \frac{1}{3} C v_g^2 \tau \tag{6}$$

To solve Eq.4 both the group velocity and the relaxation time of the material are required. The most common way to obtain these parameters is to first obtain the group velocity of the most active phonon and then use this v_g, the specific heat C and thermal conductivity of the bulk material k in Eq.6 to obtain the relaxation time τ.

Although they are simple to use, gray models cannot distinguish between different phonon polarizations. The energy exchange between different phonon groups cannot be accurately identified by using a gray model since all the phonons are grouped and relaxation time approximation is used. Therefore, in systems where the phonon relaxation mechanisms are important non-gray models should be preferred.

2.4.3.3 Non-Gray Models

Non-gray models that have been used so far can be divided into two categories as semi-gray and full dispersion models. With the semi-gray model (also called two-fluid model), phonons are divided into propagating and reservoir modes. Propagating mode phonons are responsible for transporting energy while the reservoir mode phonons are purely capacitive.

Full dispersion models are the most complicated and detailed of all phonon models discussed before. The idea of a full dispersion model is to model different phonon modes as well as their interactions with each other in a more detailed fashion. An example for this is the model suggested by Narumanchi et al. that accounts for transverse and longitudinal acoustic phonons as well as optical phonons[53]. The

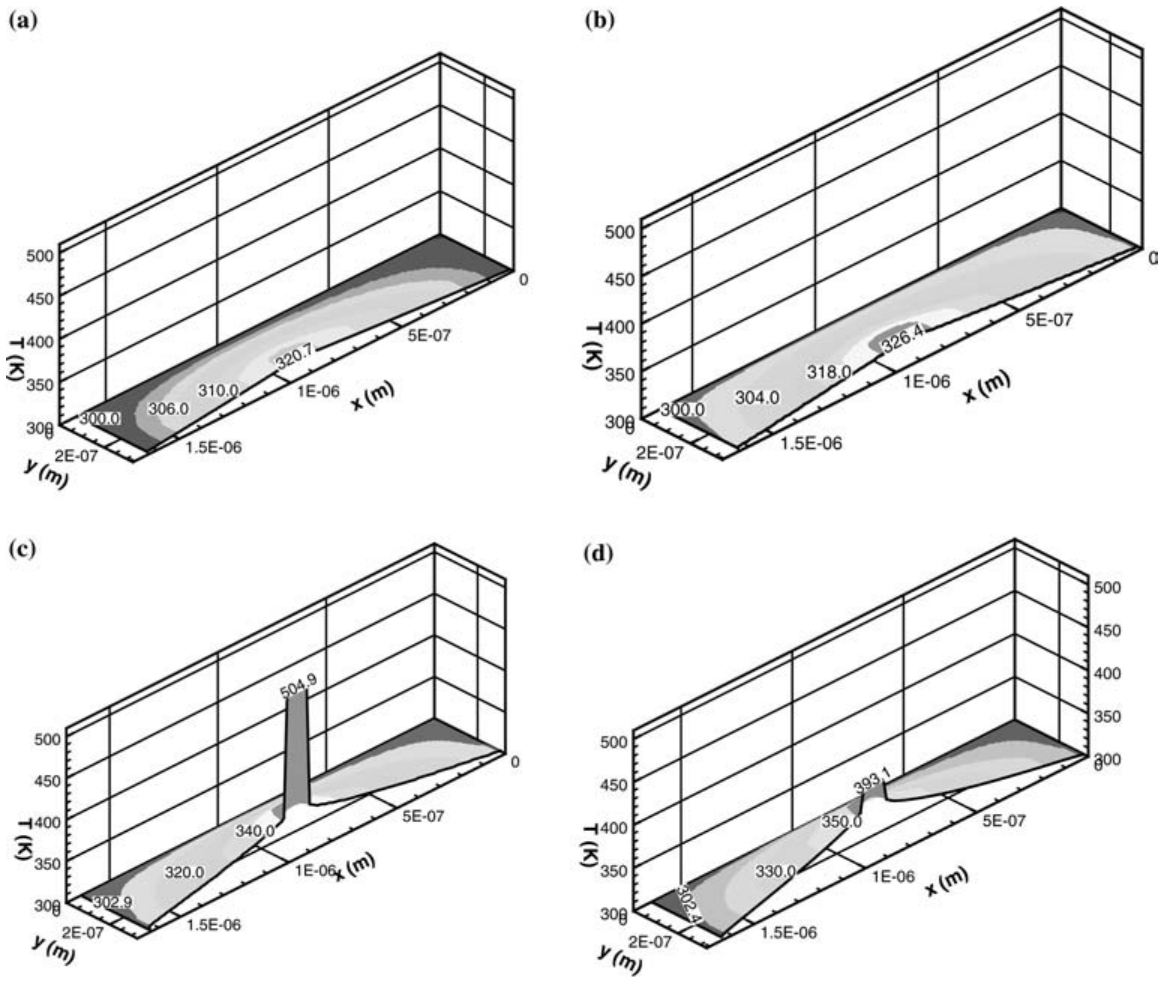

Figure 11: Lattice temperature distribution in silicon obtained using (a)Fourier (b)Gray (c)Two-Fluid (d)Full Dispersion models [12].

interactions between different phonon branches and frequencies are described by frequency dependent relaxation times that are obtained by perturbation techniques[53].

2.4.3.4 Comparison of Gray and Non-gray Models

Narumanchi et al. investigated the hotspot temperature of a silicon-on-insulator(SOI) transistor by modeling a 2D domain approximating the device and buried oxide layers[12]. Figure 11 shows the comparison of temperature contour plots of this domain obtained using Fourier, gray, and non-gray models[12].

Figure 11 shows that significantly higher temperatures are observed when two fluid

method is used. Figure 11 also shows that temperatures obtained by full-dispersion models are higher than the gray model but lower than the two-fluid model. Knowing that a full-dispersion model accounts for more of the phonon-phonon scattering and transport physics, it can be concluded that gray models may underestimate the temperature while two-fluid models over predict the temperatures in silicon[12].

2.5 Modeling Electron Transport

The electrical modeling of the heat dissipation region in AlGaN/GaN HFETs is very important for accurate modeling of the temperature distribution in these devices. In the past, focus has been placed on fully coupled electro-thermal simulations to show the negative effects of temperature on electrical performance[36, 35, 34, 37].

In most of these simulations, the thermal energy equations are solved using Fourier's diffusion equation in the entire lattice that is modeled. Some more detailed thermal models included package, substrate or size effects on the thermal response. However, the Joule heating is treated in a simplified way either through the use of a uniform heat source or surface heat flux under the gate edge or through the channel [57, 58, 36, 59, 60, 9]. However, most of these simulations neglect the non-Fourier effects caused by the extreme localization of heat generation in devices. To include such effects in thermal simulations Joule heating distribution should be obtained from the electron transport models.

Some methods used for modeling electron transport include 1)the self-consistent solution of the Shrödinger-Poisson equations, 2)solving macroscopic transport equations by using drift-diffusion or hydrodynamic models and 3)Monte Carlo solutions of the BTE for electrons[61].

2.5.1 Self-consistent Solutions of Shrödinger - Poisson Equations

The self-consistent solutions of Shrödinger-Poisson equations has been used for GaN HFET modeling in the past [62, 63, 64]. The Poisson equation gives the electric

potential for a given charge distribution:

$$\bigtriangledown \cdot \epsilon \bigtriangledown \phi(x) = \rho(x) \tag{7}$$

where ϵ is the electrical permittivity, ϕ is the electrical potential, and ρ is the charge density. Shrödinger equation gives the electron wave function or the charge distribution for a given potential. One dimensional steady-state Shrödinger equation is given as:

$$-\frac{\hbar^2}{2}\left[\frac{d}{dx}\left(\frac{1}{m^*}\right) + V(x)\right]\Psi(x) = E\Psi(x) \tag{8}$$

here m^* is the effective mass, E is the electrical field, $\Psi(x)$ is the electron wavefunction, and $V(x)$ is the potential energy constraint which is a function of electrical potential $\phi(x)$. Thus, the Poisson equation and Shrödinger equation are coupled, and numerical solution of the system of equations is required. However even the 1D Shrödinger equation is the most physically sophisticated quantization model. Thus, simulations performed with this model tend to be slow and often lead to convergence problems. As a result, the Shrödinger equation is used mainly for the validation and calibration of other quantization models [65].

2.5.2 Solution of Macroscopic Transport Equations

Just like phonons electron distribution can also be modeled by the Boltmann Transport Equation (BTE). Drift Diffusion and Hydrodynamic equations are obtained from the BTE by the method of moments and provide results with reasonable accuracy [66]. Rousseau et al., and Benbakhti et al., came up with their own solvers [66, 36] and even tested the accuracy of hydrodynamic model solver compared to Monte Carlo simulations [66]. The commercial device simulation software Sentaurus by Synopsys and also its solver: Device Simulation For Smart Integrated Systems (DESSIS) [65] have been popular tools for GaN HFET modeling [37, 67, 68, 69].

Sentaurus is capable of modeling the electron, phonon, and lattice dynamics solving the Poisson equation, the electron and hole continuity, and energy conservation equations [65]. There are three main models in Sentaurus: drift diffusion, thermodynamic, and hydrodynamic. Since the purpose is to obtain the Joule heating distribution, thermodynamic and hydrodynamic models can be used for device simulations.

2.5.2.1 Thermodynamic Model

The thermodynamic (or nonisothermal) model used by Sentaurus extends the drift-diffusion approach to account for thermal effects [65]. The thermodynamic model solves the Poisson and electron/hole continuity equations to obtain the electron and hole current densities. The Poisson equation solved in thermodynamic model is given as:

$$\bigtriangledown \cdot \epsilon \bigtriangledown \phi = -q(p - n + N_D + N_A) - \rho_{trap} \tag{9}$$

here q is the elementary ionic charge, n and p are the electron and the hole densities, N_D is the concentration of ionized donors, N_A is the concentration of ionized acceptors, and ρ_{trap} is the charge density due to traps and fixed charges[65]. The electron and the hole continuity equations are given as:

$$\bigtriangledown \cdot \vec{J_n} = qR_{net} + q\frac{\partial n}{\partial t} \tag{10a}$$

$$\bigtriangledown \cdot \vec{J_p} = qR_{net} + q\frac{\partial p}{\partial t} \tag{10b}$$

here R_{net} is the electron hole recombination rate, $\vec{J_n}$ is the electron current density, and $\vec{J_p}$ the hole current density. While using this model, it is assumed that the charge carriers are in thermal equilibrium with the lattice. With this assumption, the carrier temperatures and the lattice temperature are described by a single temperature, T. In thermodynamic model electron current density, $\vec{J_n}$, and the hole current density,

$\vec{J}_p$, are given as functions of temperature. In other words, the temperature gradient is included as a current driving force using P_n and P_p which are the absolute thermo-electric powers[65]. Moreover, the lattice temperature depends also on the electron, hole current densities and should be computed using the Eq.11[65].

$$\begin{aligned}\frac{\partial C_L T}{\partial t} - \nabla \cdot k \nabla T = &- \nabla \cdot \left[\left(P_n T + \Phi_n \right) \vec{J}_n + \left(P_p T + \Phi_p \right) \vec{J}_p \right] \\ &- \left(E_C + \frac{3}{2} kT \right) \nabla \cdot \vec{J}_n - \left(E_V + \frac{3}{2} kT \right) \nabla \cdot \vec{J}_p \\ &+ q R_{net} (E_C - E_V + 3KT)\end{aligned} \tag{11}$$

where k is the thermal conductivity and C_L is the lattice heat capacity. E_c and E_v are the conduction and valence band energies, Φ_n and Φ_p are the electron and hole quasi-Fermi potentials and R_{net} is the net electron hole recombination rate. The summation of the terms on the right hand side of the equation can be treated as the volumetric heat generation.

It has been suggested to use the hydrodynamic (or energy balance) model instead of drift diffusion when the characteristic dimensions of the semiconductor devices reach the submicron regime[65]. The drift-diffusion approach cannot reproduce sub-micron effects such as velocity overshoot, which happens when the transit times of a charge carriers are shorter than the time required to emit optical phonons[70]. In HFETs, submicron electron and lattice dynamics become important due to confinement of electrons and decreasing device dimensions. Thus, the hydrodynamic model should be used for the investigation of Joule heating of these devices.

2.5.2.2 Hydrodynamic Model

The hydrodynamic model solves the energy conservation equations for electrons, holes, and the lattice in addition to Poisson and continuity equations. The energy conservation equation for the electrons, holes, and the lattice are described as[65]:

$$\frac{\partial W_n}{\partial t} + \nabla \cdot \vec{S}_n = \vec{J}_n \cdot \nabla E_C \frac{\partial W_n}{\partial t}|_{col} \tag{12a}$$

$$\frac{\partial W_p}{\partial t} + \nabla \cdot \vec{S}_p = \vec{J}_p \cdot \nabla E_V \frac{\partial W_p}{\partial t}|_{col} \tag{12b}$$

$$\frac{\partial W_L}{\partial t} + \nabla \cdot \vec{S}_L = \frac{\partial W_L}{\partial t}|_{col} \tag{12c}$$

where W_n, W_p, and W_L are the electron, hole, and lattice energy densities, $\vec{S_n}$, $\vec{S_p}$, and $\vec{S_L}$ are the electron, hole, and lattice heat flux vectors, and t is time. The terms on the left hand side of the Eq.12 are the collision terms and represent the energy transfer within the carriers through the collision and the relaxation events. The collision term for the lattice is given as below[65]:

$$\frac{\partial W_L}{\partial t}|_{coll} = H_L + \zeta_n \frac{W_n - W_{n0}}{\tau_{ep}} + \zeta_p \frac{W_p - W_{p0}}{\tau_{ep}} \tag{13}$$

here H_L is the energy loss/gain rate due to generation/recombination events. W_n and W_p are the electron and hole energy densities, while W_{n0} and W_{p0} are the corresponding equilibrium energy densities. τ_{en} and τ_{ep} are the energy relaxation times between lattice and electrons and holes respectively, ζ_n and ζ_p are the parameters used for the numerical stability[65]. Finally the temperature of the lattice can be computed from the lattice energy density using the equation below:

$$W_L = C_L T \tag{14}$$

It has been noted that, the lattice temperature calculated this way in electrical simulations is not accurate since such electrical models generally include the active layers but not the surrounding geometries such as the substrate and the package. Although the effects of these geometries on electrical performance are negligible[1], their effects on thermal performance are significant.

2.5.3 Monte Carlo Simulations

The Monte Carlo method can be used for simulating the electron transport in semiconductor devices. Using the Monte Carlo method, the trajectories and the individual scattering events of carriers can be modeled using classical mechanics. Random numbers are used to determine the scattering events and the distance traveled by the carrier between successive scattering events. If large ensembles of carriers are simulated instead of individual carriers, the simulations are often named Ensemble Monte Carlo simulations. Ensemble Monte Carlo simulation is an established stochastic numerical method to study non-stationary and non-equilibrium transport in semiconductor materials and devices [71, 72, 73].

Although computationally expensive, electron dynamics in AlGaN/GaN HFETs have been modeled using Monte Carlo simulations in the past as well [74, 33, 35, 75, 76]. The electro-thermal simulations performed using Monte Carlo simulations can be categorized in two groups. The first group executes Monte Carlo simulations for electrons and then uses the steady state heat diffusion equation for thermal modeling [35, 75]. In the second group thermal transport is also modeled using Monte Carlo simulations for acoustic and optical phonons in the lattice [33, 76]. The latter group is especially important since it provides information of the energy decay pathway that can be used to describe the phonon bottleneck in the GaN HFET devices.

Although Monte Carlo simulations are computationally demanding compared to Sentaurus device simulations, they provide important information about the carrier scattering, such as the percentage of energy given to different phonon modes in the crystal.

2.6 Conclusion

In this chapter the complex energy decay in AlGaN/GaN HFETs is discussed. The electron-lattice interactions that starts with the Fröhlich interaction of electrons with

high energy optical phonons and continues with the slow relaxation of optical phonons into optical and acoustic phonons via Ridley channel has been explained. Moreover, the different techniques used to model the lattice vibration and electron physics in devices has been discussed.

CHAPTER III

NUMERICAL SOLUTION OF PHONON BTE

For the solution of the phonon BTE, Monte Carlo simulations can be used[77]. However, due to the large number of collision interactions that must be computed, Monte Carlo simulations are not computationally favorable for domains with length scales of 1 μm or greater [78]. On the other hand, numerical solutions of the phonon BTE permit the analysis of complex domains, varying boundary conditions and are relatively easy to implement[52].

In recent years, numerical techniques based on the finite difference lattice Boltzmann method (LBM) and the finite volume discrete ordinates method (FVDOM) have been used to solve both gray and non-gray ballistic-diffusive phonon transport in semiconductor devices [46, 55, 79, 53, 80]. Despite their general success, a number of computational issues including some limitations of LBM still remain. In this chapter, the two methods, LBM and FVDOM, are introduced and their predictions to simple cases with known solutions and to each other for systems with various phonon Knudsen numbers are compared. The goal is to determine the limits of applicability of the two methods which have not been presented in this field of research.

3.1 Lattice Boltzmann Method

LBM has been developed from a collection of cells on a grid of specified shape called cellular automata [81]. The cell states evolve through a number of discrete time steps according to rules based on the neighboring cells' states (i.e., energies). Although, LBM was developed mostly for the analysis of fluid mechanics, it has recently been used for the solution of phonon transport equations for the sub-continuum heat transport [82, 83, 84, 79]. Eq.4 can be transformed into a discrete Boltzmann equation

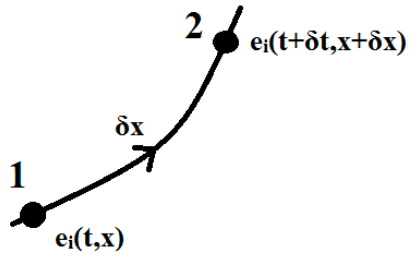

Figure 12: Free flight of phonon along direction i.

by discretizing the velocity space by introducing a finite set of velocities, $\vec{v_i}$'s and associated energy densities, e_i's along those directions as [81]:

$$\frac{\partial e_i}{\partial t} + \vec{v_i} \cdot \nabla e_i = \frac{e_{i0} - e_i}{\tau} + q_i''' \tag{15}$$

Here e_i is the non-equilibrium phonon energy density, $\vec{v_i}$ is the velocity, e_{i0} is the local equilibrium energy of phonons propagating in the ith direction,and τ is the relaxation time which is independent of the direction [85].

In LBM, it is assumed that phonons are ballistic between lattice sites and scatter when they reach lattice sites[9]. Figure 12 illustrates a free flight of phonon from point 1 to 2. To ensure collisions to occur at lattice sites and satisfy stability, the lattice spacing should be chosen smaller than the mean free path [9]. Due to previously stated reasons, non-uniform node spacing and non-gray models with a spread of relaxation times is not easily handled in LBM.

Using a first order Taylor series expansion energy density at point 2 in a given direction can be written as:

$$e_i(x + \vec{v_i}\delta t, t + \delta t) = e_i(x,t) + \frac{\delta e_i}{\delta t}\delta t + \frac{\delta e_i}{\delta x}\delta x \tag{16}$$

Subtracting $e_i(x,t)$ from both sides and dividing both sides by δt right hand side of the equation can be equated to $\frac{\delta e_i}{\delta t} + \frac{\delta x}{\delta t}\frac{\delta e_i}{\delta x}$. This term becomes equal to the total derivative (left hand side of Eq.15 when the nodal spacing is linked to the time step

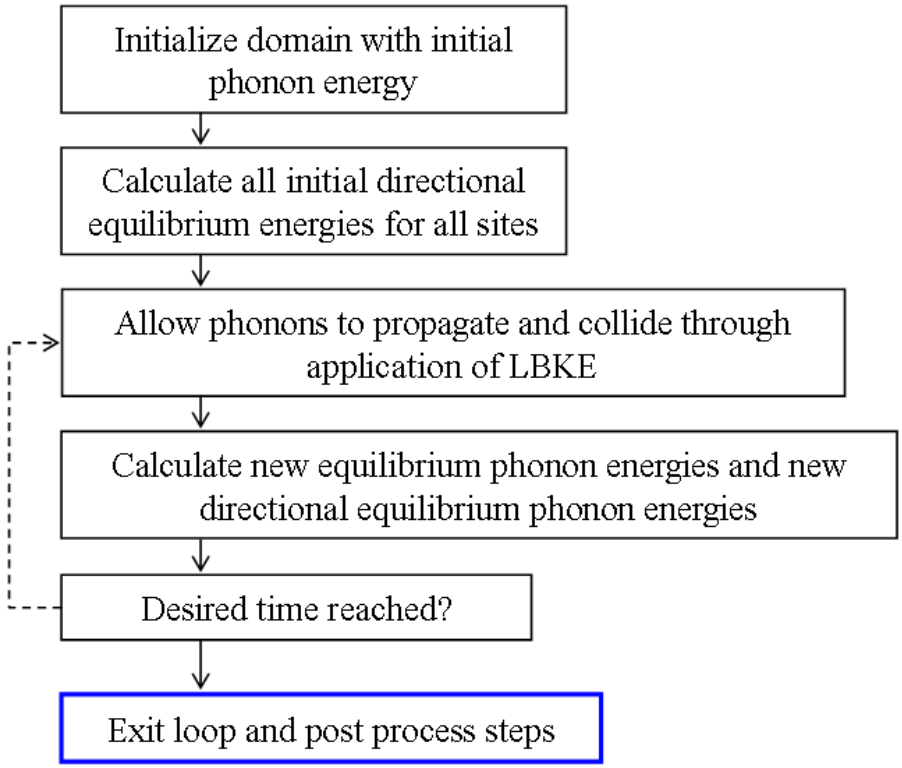

Figure 13: Flow chart explaining the time evaluation of phonon energies[9].

by $\delta x = v_g \delta t$. Thus for a discrete time step Δt Eq.16 becomes:

$$\frac{e_i(x + \vec{v_i}\Delta t, t + \Delta t) - e_i(x,t)}{\Delta t} = \frac{\Delta e_i}{\Delta t} + v_g \frac{\Delta e_i}{\Delta x} = \frac{\partial e_i}{\partial t} + \vec{v_i} \cdot \nabla e_i \tag{17}$$

Replacing the left hand side of Eq.15 with Eq.17 and further simplifying it, the Lattice Boltzmann Kinetic Equation(LBKE) is obtained as[86]:

$$e_i(x + \vec{v_i}\Delta t, t + \Delta t) = (1 - \Gamma_i) e_i(x,t) + \Gamma_i e_i^0(x,y) + q_i''' \Delta t \tag{18}$$

In Eq.18, e_i's are the non-equilibrium phonon energy of a phonon propagating along the ith direction and Γ_i's are the associated phonon scattering weight factors, given by $\Gamma_i = \Delta t/\tau$.

The flow chart explaining the numerical solution of the LBKE is given in Fig.13. In a typical implementation, the numerical solution of the LBKE is done in two steps. For each direction i, at each time step, there is a streaming phase during

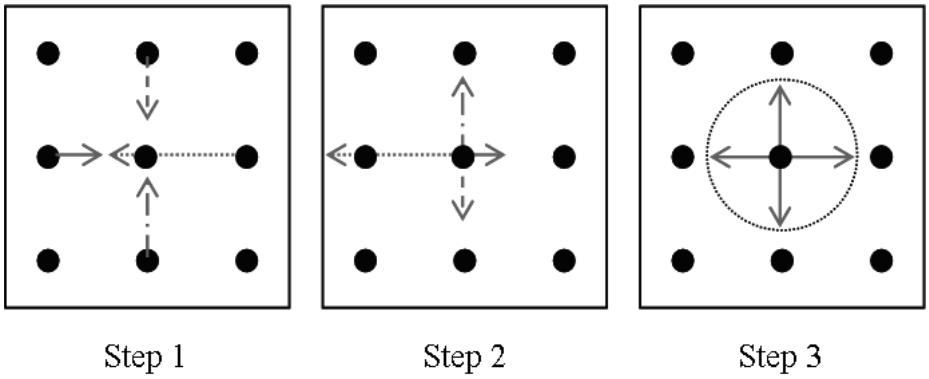

Figure 14: The representation of the propagation and collision steps of LBKE. Step 1 shows the directional phonon energy (the magnitude is represented by the arrow length) at time t. Step 2 shows how the phonons have propagated to time $t + \Delta t$. In step 3 the new directional equilibrium phonon energies have been calculated[9].

which the phonon is allowed to propagate at its assigned velocity. This is followed by a collision step during which phonons in different lattice directions are allowed to exchange energies according to Eq.18 [9]. Phonon propagation an collision steps are represented in Fig.14. The phonon scattering weight factor, Γ_i in Eq.18 is a measure of the fraction of phonons that arrive at the new lattice site which is represented with arrow lengths in Fig.14 in an equilibrium energy state within a time step of Δt.

All grid points in space are covered in this way for each direction. Directions are traversed and the procedure is repeated until the desired simulation time is reached. At the end of each time step, total energy should be computed. Based on conservation of energy, the energies propagating in all directions at a given lattice point should add up to total energy, $e(x,t)$ as [84]:

$$e(x,t) = \sum_n e_i(x,t) = C(T(x,t) - T_{ref}) \tag{19}$$

Since in LBM phonons are allowed to propagate only along the grid lattice directions, the choice of lattice structures is an important issue in implementing LBM techniques. Conventional lattices are designated as 'DdQn' (for example, D2Q9) where 'd' refers to the dimensionality and 'n' refers to number of directions to be

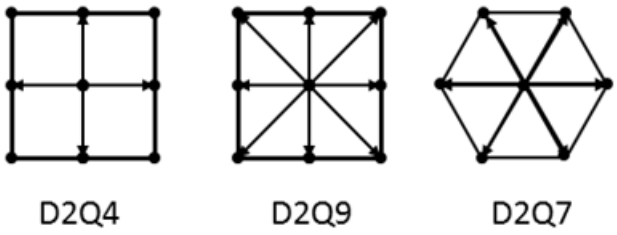

Figure 15: D2Q4, D2Q7, and D2Q9 lattice structures used in LBM simulations.

used. Figure 15 shows the lattice structure and the phonon propagation directions for D2Q4, D2Q9 [9] and D2Q7 [87] lattice types that can be used for 2D simulations. In D2Q9 the phonon speeds in diagonal directions are larger to ensure that the same number of phonons arrive at all neighboring nodes in a given time step, Δt. Using different phonon velocities is a known problem of the method [80] and as a solution to this problem, D2Q7 lattices are suggested [87]. Phonons travel equal distances in every direction of the hexagonal lattice at a given time step while all phonons travel at the same velocity. However, with this lattice type, regular rectangular geometries cannot be easily modeled.

In LBM, the local equilibrium energy along a given direction is defined by partitioning the total energy using the directional weight along that direction according to Eq.20 [84]:

$$e_i^0(x,t) = w_i e(x,t) \tag{20}$$

where w_i's are directional weights. Most of the time, directional weights, are taken to be equal to each other while their summation is equal to unity. An exception to this is the conventional D2Q9 lattice which has a stationary particle. In the past, researchers using LBM for phonon dynamics assumed the weight of the stationary particle, in this case phonons, to be equal to zero and all other weights to be equal [84, 82].

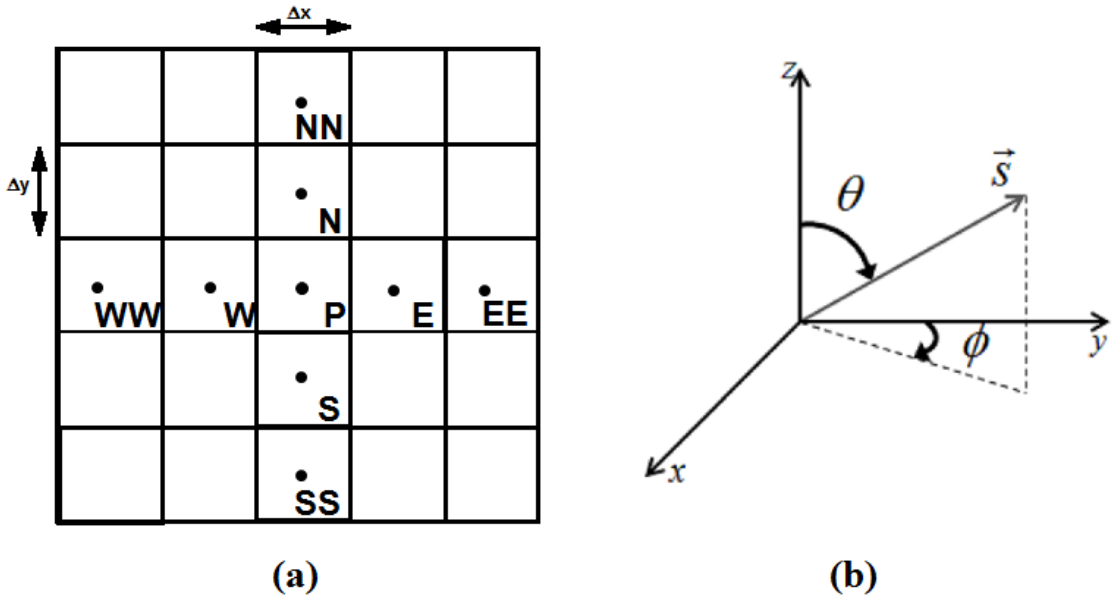

Figure 16: a)Spatial and (b)angular discretization of the phonon BTE by DOM.

3.2 Discrete Ordinates Method

The Discrete Ordinates Method (DOM) is another method commonly used for the solution of phonon BTE. Unlike LBM, the spatial and angular discretization of the domain are independent of each other in the DOM. Both discretization schemes are shown in Fig.16. In this method, the spatial discretization of Eq.4 is performed using a control volume technique and angular discretization is performed using discrete ordinates.

The discrete ordinates method (DOM) was introduced by Chandrasekhar [88] for neutronics and then developed by Lathrop and Carlson [89]. Later, DOM was used for radiative heat transfer [90, 91] and for phonon transport modeling [92]. The basic outline of the technique used to discretize the phonon BTE is given next.

3.2.1 Angular Discretisation

The angular space at any lattice location is discretized into solid angles to allow phonon propagation. The steady state, gray phonon transport equation in Eq.4 when

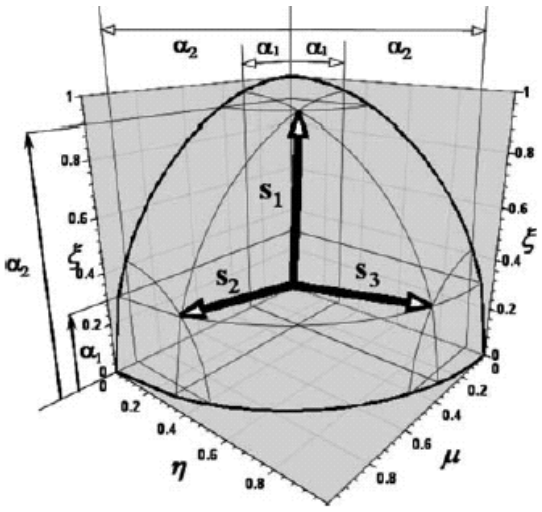

Figure 17: Angular discretization of an octant with S4 quadratures [13].

discretized in the angular space can be rewritten as[13]:

$$\vec{s_i} \cdot \nabla v_{gi} e_i = \frac{e_i^0 - e_i}{\tau} + q_i''' \tag{21}$$

Here, $\vec{s_i}$ is the unit vector in the direction i, v_{gi} is the phonon speed in that direction. The discrete values of e, denoted by e_i in direction i, are stored at the cell centroids. The choice of phonon propagation directions,i's depend on the angular discretization scheme used. The different methods used for angular discretization are Gauss Legendre [39], S_N, and control angle discretization.

3.2.1.1 S_N Quadratures

S_N quadratures have been used for multidimensional problems[2, 93]. In S_N, no direction of propagation is favored, thus strict symmetry conditions are satisfied by them. Figure 17 is the representation of 3 phonon propagation directions in an octant of solid angle when S4 quadratures are used.

When the unit vector along direction i in S_N quadratures is given as $\vec{s_i} = (\mu_i, \gamma_i, \xi_i)$ all the directions $\vec{s_i} = (\pm\mu_i, \pm\gamma_i, \pm\xi_i)$ are also considered to be in the quadrature. Total number of directions in S_N quadrature, M is calculated as $M = N(N+2)$.

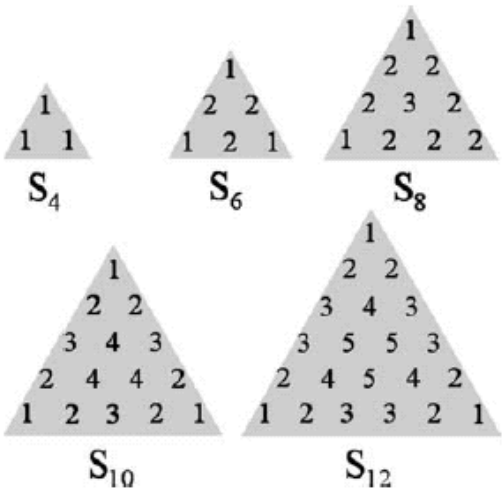

Figure 18: Schematic representation of one octant of quadratures S_4 to S_{12}. Directions with same weights are marked with same numbers [13].

Figure 18 is the schematic representation of one octant of quadratures S_4 to S_{12}. Directions numbered the same share the same weight, w_i. To determine the weights several constraints are required for example:

$$\sum_{m=1}^{M} w_i = 4\pi \tag{22}$$

Other constraints used to determine weights of higher order S_N quadratures are conservation of first and second moment even with the lowest number of quadratures. The first moment condition is satisfied when:

$$\sum_{m=1}^{M} |\mu_i w_i| = \pi \tag{23}$$

As a result of conservation of first moment accurate heat flux is calculated even when lower number of directions are used [13]. Moreover with the conservation of second moment given in Eq.24 rotational invariance is guaranteed. And finally it is observed that ray effects caused by insufficient number of phonon propagations are not as significant as it is with other quadratures.

$$\sum_{m=1}^{M} |\mu_i^2 w_i| = \pi \tag{24}$$

Directions and weights of S_4, S_6, and S_8 quadratures used in this study are given in Appendix A. When S_N quadratures are used to solve the phonon BTE, the lattice energy, e and the temperature T can be found from directional energies, $e_i's$, as:

$$4\pi e^0 = C(T - T_{ref}) = \sum_{m=1}^{M} e_i w_i \tag{25}$$

3.2.1.2 Control Angles

When control angle discretization was used for discretizing the angular domain, each octant is divided into $M = N\theta \times N\phi$ uniform solid angles. Here θ and ϕ are the polar and azimuthal angles shown in Fig.16[94]. The directional unit vector, $\vec{s_i}$ associated with each solid angle is given as:

$$\vec{s_i} = sin(\theta_i)sin(\phi_i)i + sin(\theta_i)cos(\phi_i)j + cos(\theta_i)k \tag{26}$$

When Eq.21 is integrated over the discrete angular control volume it takes the form:

$$\vec{S_i} \cdot \nabla v_g e_i = \frac{e_i^0 - e_i}{\tau} \Delta\Omega_i + q_i''' \Delta\Omega_i \tag{27}$$

where $\vec{S_i}$ is the direction cosine and $\Delta\Omega_i$ is the solid angle associated with direction i. These are given as [55]:

$$\vec{S_i} = \int_{\phi-\Delta\phi\backslash 2}^{\phi+\Delta\phi\backslash 2} \int_{\theta-\Delta\theta\backslash 2}^{\theta+\Delta\theta\backslash 2} \vec{s_i} sin(\theta) d\theta d\phi \tag{28}$$

$$\Delta\Omega_i = \int_{\phi-\Delta\phi\backslash 2}^{\phi+\Delta\phi\backslash 2} \int_{\theta-\Delta\theta\backslash 2}^{\theta+\Delta\theta\backslash 2} sin(\theta) d\theta d\phi \tag{29}$$

When control angles are used the lattice equilibrium energy and temperature can be found from directional energies:

$$4\pi e^0 = C(T - T_{ref}) = \sum_{i=1}^{M} e_i \Delta\Omega_i \tag{30}$$

3.2.2 Spatial Discretisation

After the angular discretization, spatial discretization will be handled. First, the spatial domain is discretized into structured rectangular control volumes as in Fig.16(a) and then Eq.27 is integrated along this control volume to get Eq.31:

$$v_g e_i^e \Delta y S_{i,x} - v_g e_i^w \Delta y S_{i,x} + v_g e_i^s \Delta x S_{i,y} - v_g e_i^n \Delta x S_{i,y} = \frac{e^0 - e_i}{\tau} \Delta V \Delta\Omega_i \tag{31}$$

where $S_{i,x}$ and $S_{i,y}$ are the x and y components of the direction cosine $\vec{S_i}$. The first four terms of Eq.31 require directional energies at the east, west, south and north faces: e_i^e, e_i^w, e_i^s, and e_i^n respectively. Figure 19 shows the spatial discretization of the domain and the directional energies at east, west, north, and south faces of node P along $i(+x)$ and $i'(+y)$ directions.

To define these face values certain approximations can be used. First order upwind scheme, linear upwind scheme (LUS)[95], Sharp And Monotonic Algorithm for Realistic Transport (SMART)[96], or Quadratic Upwind Interpolation for Convective Kinematics (QUICK) [40] are some examples to such approximations. In order to get accurate and realistic results the approximation used should exhibit three fundamental properties [97]:

• Conservativeness: An approximation is conservative if the flux leaving a control volume is equal to flux entering the adjacent control volume.

• Boundedness: This property is satisfied when the resulting matrix of coefficients is

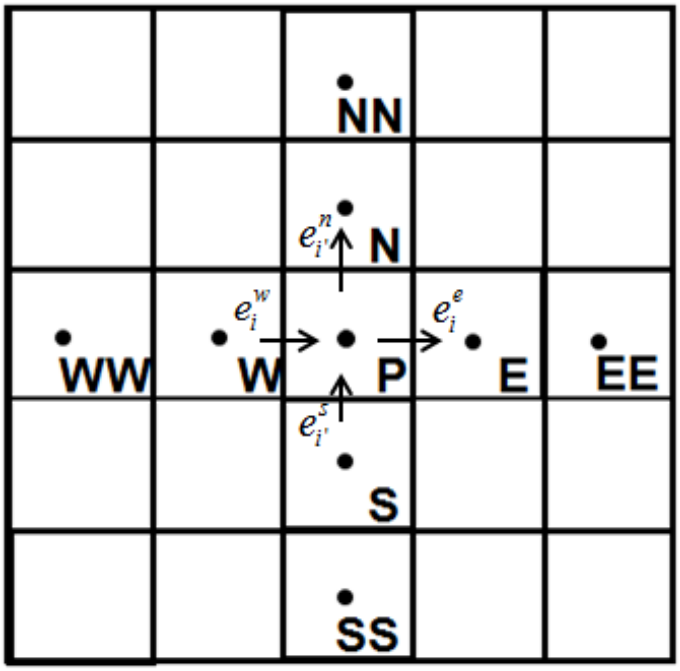

Figure 19: Spatial discretization and the face values of directional energies along the $i(+x)$ ans $i'(+y)$ directions.

diagonally dominant, thus numerical convergence is guaranteed.

• Transportiveness: Approximation has transportiveness property if it accounts for the direction of flow.

3.2.2.1 First Order Upwind Scheme

This is the simplest technique that can be used to define a face value. Moreover, it possesses all the fundamental properties listed above. When first order upwind scheme is used, east face value of phonon energy density along direction i in Fig.19 can be found from those at the cell centroids as:

$$e_i^e = e_i^P \tag{32}$$

Although this technique is simple to implement it becomes highly diffusive in space giving erroneous results[97]. This phenomenon is often known as 'false diffusion'.

3.2.2.2 Central Differencing Scheme

Central differencing scheme (CDS) is second order accurate while first order upwind is first order accurate. Moreover, it eliminates 'false diffusion'. When it is used the energy density at the east face along direction i is given as:

$$e_i^e = \frac{e_i^P + e_i^E}{2} \tag{33}$$

However, it was observed that when CDS is used calculations were unstable. This can be explained with the boundedness property. It is known from computational fluid dynamics that when Peclet number, which defines the strength of advection to diffusion, is greater than 2 ($Pe > 2$) boundedness property is not satisfied any longer. Thus, CDS calculations tend to become unstable.

Analogous to this, when this scheme is used for ballistic-diffusive heat transfer and as the ballistic effects become more pronounced CDS gives unrealistic solutions. To solve this hybrid techniques can be used with certain types of problems. However, to completely eliminate these errors higher order upwinding techniques involving higher order terms beyond simple nearest neighbors should be used.

3.2.2.3 Quadratic Upwind Interpolation for Convective Kinematics (QUICK)

A popular higher order upwinding technique is the QUICK scheme. Both QUICK and the QUICKEST (QUICK with Estimated Streaming Terms) schemes were presented by Brian P. Leonard in 1979[98]. The QUICK scheme is a linear scheme to represent cell face values using the second neighbors, denoted by WW, NN, SS and EE in Fig.16(a). QUICK scheme representation of the east face value of phonon energy density along direction i, e_i^e is:

$$e_i^e = 6/8e_i^P + 3/8e_i^E - 1/8e_i^W \tag{34}$$

One of the disadvantages of the QUICK schemes is the oscillation of results at

the boundaries and the regions where steep gradients exist, which can be a source of error for problems with highly localized heat generation. It has been shown that for a 1-dimensional domain with localized heat generation the heat flux calculated using the QUICK scheme has an oscillatory behavior at the boundaries and neat the heat generation region[40].

3.2.2.4 Linear Upwind Scheme (LUS)

The linear upwind scheme (LUS) developed by Price [95] is another higher order technique and has a relatively simple implementation, higher order accuracy, and numerical stability. When it is used, the energy at the east face is given as [95]:

$$e_{ie} = e_i^P + \frac{e_i^P - e_i^W}{2} \tag{35}$$

3.2.2.5 Sharp And Monotonic Algorithm for Realistic Transport(SMART)

SMART is a non-linear scheme used to estimate the cell face values. Non-linear schemes analyze the solution and change the cell face value approximations to avoid any unwanted behavior, such as unboundedness. However, linear schemes are easier to implement on code.

When one of the above mentioned linear upwinding techniques is used the Eq.31 takes the form:

$$\begin{aligned} &a_i^P e_i^P - a_i^E e_i^E - a_i^W e_i^W - a_i^N e_i^N - a_i^S e_i^S - a_i^{EE} e_i^{EE} - \\ &a_i^{WW} e_i^{WW} - a_i^{NN} e_i^{NN} - a_i^{SS} e_i^{SS} + \sum K_{ii'} e_{i'}^P + q''' = 0 \end{aligned} \tag{36}$$

where $a_i's$ depend on the direction and the upwinding scheme used. In this chapter, a first order upwinding technique is used to compare the performance of LBM and DOM methods for relatively simple problems. Thus the Eq.36 will take the form:

$$a_i^P e_i^P - a_i^E e_i^E - a_i^W e_i^W - a_i^N e_i^N - a_i^S e_i^S + \sum K_{ii'} e_{i'}^P + q''' = 0 \tag{37}$$

where $a_i's$ are given as:

$$a_{gi}^{E} = max(\frac{-v_g\mu_i}{\Delta x}, 0) \qquad (38a)$$

$$a_{gi}^{W} = max(\frac{v_g\mu_i}{\Delta x}, 0) \qquad (38b)$$

$$a_{gi}^{N} = max(\frac{-v_g\eta_i}{\Delta y}, 0) \qquad (38c)$$

$$a_{gi}^{S} = max(\frac{v_g\eta_i}{\Delta y}, 0) \qquad (38d)$$

$$a_{gi}^{P} = max(\frac{v_g\mu_i}{\Delta x}, 0) + max(\frac{-v_g\mu_i}{\Delta x}, 0) + max(\frac{v_g\eta_i}{\Delta y}, 0) + max(\frac{v_g\eta_i}{\Delta y}, 0) \qquad (38e)$$

A sequential marching solution is employed to solve Eq.37. At the start of each iteration, the value of e^0 at node P is computed from prevailing values of e_i at node P using the relation in Eq.30. At the end of the iteration, e^0 and the temperature T at every point may be calculated using the same relation with constant specific heat assumption.

3.3 Performance Comparison

Both DOM and LBM are numerical solution techniques for the phonon BTE which allow phonons to scatter and propagate within a discretized domain. The major difference between them is the approach they use to address the discretization of angular space. Angular discretization is especially important in regions where ballistic phonon transport is significant. It is expected that for small domains, where ballistic effects are present, view factors between the boundaries become especially important. When angular discretization is not fine enough, the view factors are not captured properly thus errors can be observed. This is often called ray effect[99].

To compare the performance of the two methods in ballistic-diffusive limits the two boundary value problems (i.e., two test cases) shown in Fig.20 were used. First, the

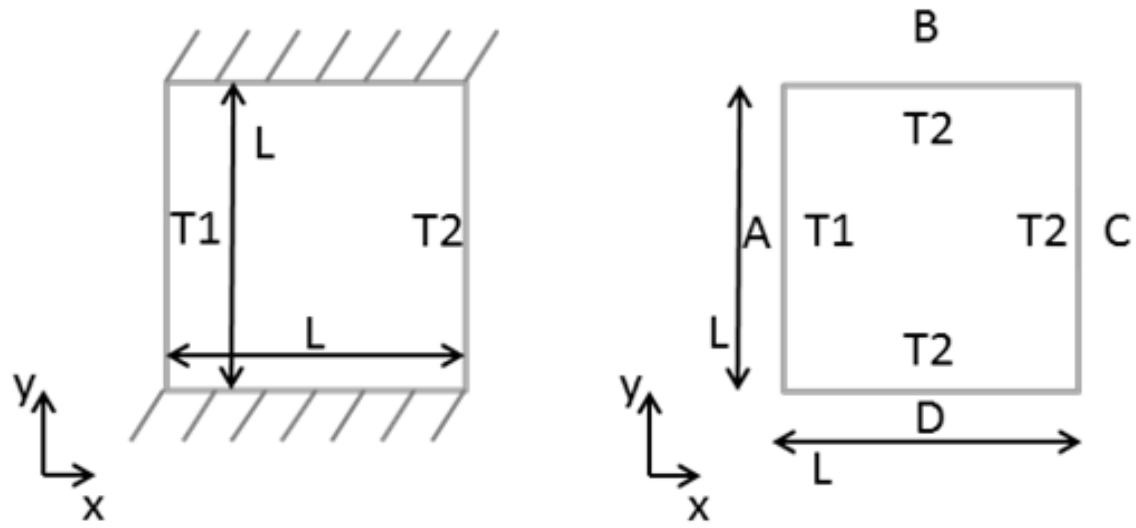

(a) (b)

Figure 20: The test cases used for the LBM, DOM comparison: (a)Case1: 1D phonon transport across a slab. (b)Case 2: 2D phonon transport with given temperature boundaries.

one dimensional phonon transport problem, shown in Fig.20(a), was used to understand the behavior of LBM and DOM when used to model one dimensional problems. Moreover, this problem acts also as a verification case for the numerical results since an analytical solution exists from the mathematically analogous radiative transfer in a gray medium[90]. The objective of the second problem, shown in Fig.20(b), was to investigate the performance of LBM and DOM in modeling two dimensional problems and to examine the effect of angular resolution when there were spatially-varying thermal boundary conditions. This is particularly important since two dimensional models can be used in AlGaN/GaN HFET modeling.

For both of these test cases, the domain size, L with respect to mean free path of phonons, Λ was changed to investigate the ballistic to transport regimes. Ratio of mean free path to the characteristic domain size is called Knudsen(Kn) number, Kn($Kn = \Lambda/L$). Knudsen number was varied between 0.01 to 100 to cover the range of diffusive to ballistic transport for this study.

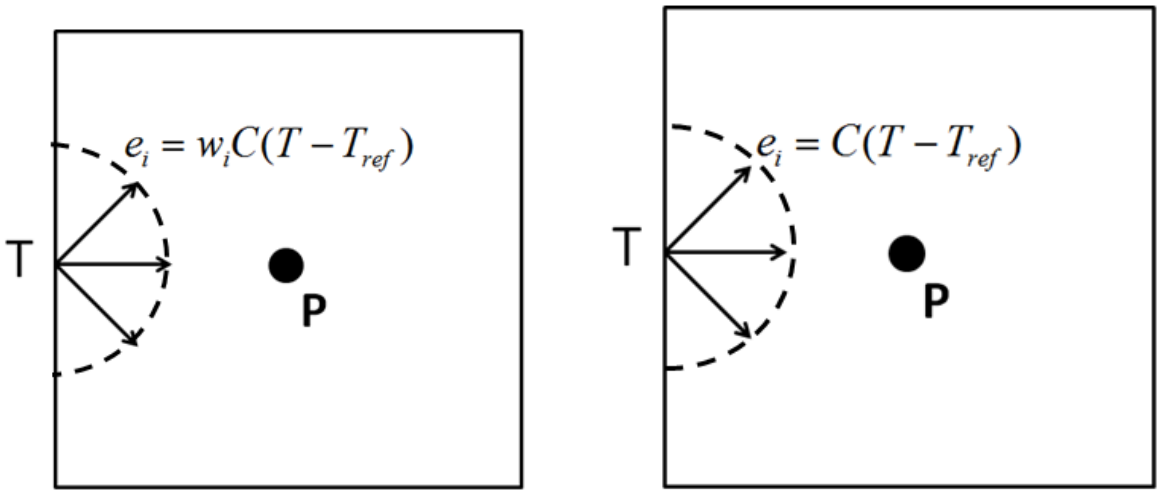

(a) (b)

Figure 21: Schematic of the temperature boundary condition in: (a)LBM and (b)DOM.

The group velocity used for simulations was $\vec{v_g} = 1000m/s$, and the relaxation time was $\tau = 100ps$ giving the mean free path of phonons as $\Lambda = 100nm$. Bulk thermal conductivity was assumed to be $k = 254W/mK$ which provides properties related to high quality GaN materials [9].

The effects of domain sizes (L), the number of angular directions, different types and non-uniformity of boundary conditions were investigated using these two boundary value problems. Angular discretization effects were observed using LBM with lattice types D2Q4 and D2Q9 and DOM with angular discretization of $(N\theta \times N\phi)$:1×1, 2×2, 4×4, and 8×8 per octant. Finally, a spatial mesh of 251×251 was used with all simulations to ensure convergence.

3.3.1 Case 1: 1D Phonon Transport

In this test case, Case 1, which is shown in Fig.20(a), the top and the bottom walls were specular adiabatic to represent symmetry boundary conditions whereas the right and the left boundaries were given temperature boundary conditions, $T1 = 301K$ and $T2 = 300K$, to impose a temperature gradient. The details about how to apply the

boundary conditions is given next.

3.3.1.1 Temperature Boundary Condition

In LBM the temperature boundary condition at the walls was specified by setting the inward moving non-equilibrium phonon energy densities that are shown in Fig.21 to the partitioned energy density calculated using:

$$e_i = w_i C(T - T_{ref}) \tag{39}$$

In DOM the inward moving non-equilibrium phonon energy densities were calculated using:

$$e_i = C(T - T_{ref}) \tag{40}$$

where T was the temperature of the boundary, T_{ref} was a reference temperature, and C was the specific heat of the lattice.

3.3.1.2 Reflection Boundary Condition

There are two types of reflective boundary conditions that can be used in phonon transport modeling: specular and diffuse. In this work specular reflection boundary condition was used to represent the symmetry plane. On the other hand, since it is know that reflection of phonons from real boundaries or interfaces are partially diffuse[86] diffuse reflection boundary condition was used to represent boundaries. Figure 22 represents these two different types of reflective boundary conditions.

The specular adiabatic boundary conditions was applied using the assumption that the phonons reaching the specular boundary will be reflected to the domain. Thus the inward phonon energy densities at the boundaries were equated to the outward moving phonons along the mirror directions as shown in Fig.22(a).

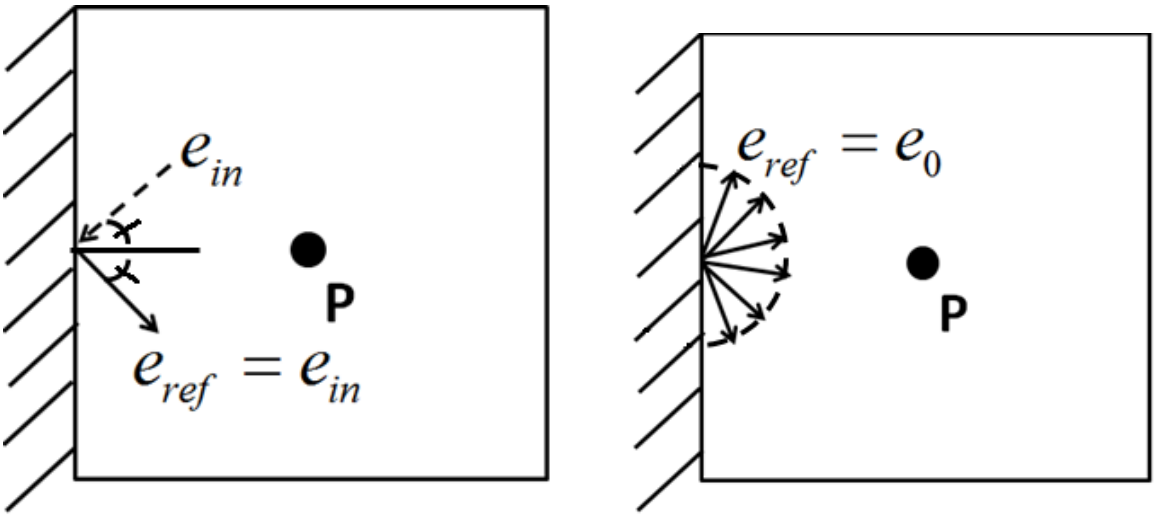

(a) (b)

Figure 22: Schematic of the (a)specular and (b)diffuse reflection boundary condition at the west boundary.

Diffuse reflection boundary condition assumes that all inward facing phonon energies to be equal to equilibrium phonon energy which will be computed from phonon energies in all directions at the boundary. This is represented in Fig.22(b).

3.3.1.3 Case 1: Results

Results were obtained using DOM with a 1st order upwinding scheme and with LBM for the case shown in Fig.23(a). Figure 23(a) shows the midline temperature obtained for a domain with Kn=100. LBM simulations with two different lattice configurations (D2Q4 and D2Q9) and DOM simulations yielded similar temperature profiles i.e., a nearly constant temperature of $(T1 + T2)/2$ through the domain and large temperature jumps at the boundaries. This was an expected result as the critical dimensional length scale was much smaller than the phonon mean free path and bulk scattering was nearly absent to cause any temperature decay through the domain. Neither the changes in angular discretization in DOM nor the lattice configuration in LBM altered this result. This trend could be observed in lower Kn numbers as well. Figure 23(b) is the plot of temperature along the midline for a domain with

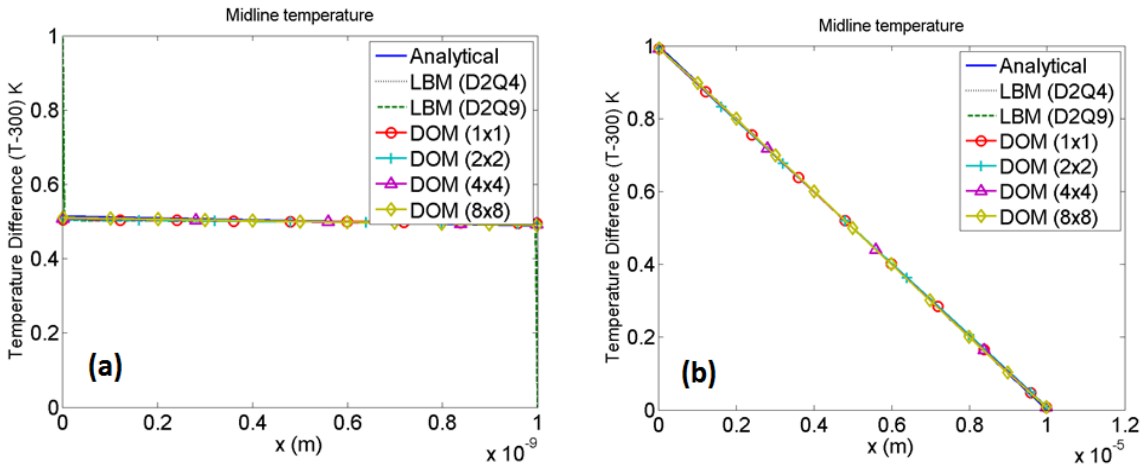

(a) (b)

Figure 23: Temperature profile on the midline(y/L=0.5) for (a)Kn=100 and b)Kn=0.01.

Kn = 0.01. For Kn=0.01, temperature drop is equally divided between the bulk domain and at boundaries. Figure 23(b) shows that temperature profiles using different angular discretizations in DOM are identical and those computed using LBM D2Q9 also agree with these.

3.3.2 Heat Flux Correction in LBM

From the analysis of two test cases it is shown that LBM calculated accurate temperature distributions for one-dimensional ballistic to diffusive problems and two-dimensional diffuse problems. However, in certain applications, the heat flux is as important as temperature. When it was calculated from the directional energy densities using the Eq.41, there were inconsistencies with the analytical results.

$$\vec{q''} = \sum \vec{v_i} e_i \tag{41}$$

This is a known issue and to correct this issue, a correction factor of 2/3 was applied to the heat flux computed with LBM codes that discretize the solid angle in two dimension only[80]. Yet, applying the heat flux correction yields accurate heat

flux only in the diffuse limit but not in the ballistic limit. To address this issue, several other approaches were developed to eliminate the need for a correction factor while giving satisfactory results in both the diffuse and ballistic limits.

3.3.2.1 Alternate Approach 1: Utilizing the concept of stationary phonons

As shown in Fig.15 D2Q9 has 9 directions associated with it with the 0th direction representing a particle at rest, or particles which do not contribute to propagation within the 2D space. It has been noted that in phonon transport modeling the stationary phonon has been neglected and the all weights are assumed to be equal with their summation equal to unity[84, 82].

However, in fluid dynamics simulations performed with LBM these stationary particles are not neglected, moreover different weights are used for different directions [81]. These weights are calculated using some constraints like conservation of angular momentum and isotropy of lattice tensor of rank 4. For reasons of symmetry, weights of directions with identical velocities should be the same, these are:

- w_0=weight of stationary phonon (direction 0)=4/9
- w_1=weight of phonons with lattice speed v(directions 1,3,5,7)=1/9
- w_2=weight of phonons with lattice speed $v\sqrt{2}$ (directions 2,4,6,8)=1/36

When these weights were used, the need for a correction factor with heat flux was eliminated in the diffuse limit. However, using these weights and a stationary phonon could not recover the thermal conductivity in the fully ballistic limit. To recover the thermal conductivity in ballistic limit a new constraint was introduced in alternate approach 2.

3.3.2.2 Alternate Approach 2: Utilizing the concept of phonon lattice speed

In this approach, instead of isotropy of lattice tensor of rank 4, ballistic constraint was used in addition to the constraint to recover the bulk thermal conductivity in diffuse limit.

For this new constraint, weights were determined based on the fact that the BTE in the diffuse limit should recover the bulk thermal conductivity. In the diffuse limit, using the Eq.4, Eq.41, and the Fourier's law, we obtained:

$$-\sum_i \tau C w_i \vec{v_i} \vec{v_i} - \Delta T = -k\Delta T \tag{42}$$

where k is the thermal conductivity of the bulk lattice. Substituting Eq.6 in to Eq.42 following constraint on weight factors and directional velocities was obtained:

$$\sum_i w_i \vec{v_i} \vec{v_i} = \frac{v_g^2}{3} \tag{43}$$

To derive the ballistic constraint we considered the case of a 1-D heat transfer in a 2-D domain with boundary temperatures set at T1 and T2 as in Fig.20(a). In the ballistic limit, a constant temperature of $\frac{T1+T2}{2}$ should be observed in the entire domain and the heat flux should be:

$$q_x'' = \sum_i w_i \vec{v_i} e_i = \frac{(T1 - T2) C v_g}{4} \tag{44}$$

In the ballistic limit for any point in the domain the directional energies were written as $e_{1,2,8} = CT1w_{1,2,8}$ and $e_{4,5,6} = CT2w_{4,5,6}$. Using the given directional energies, the bulk thermal recovery constraint given by Eq.43 and ballistic heat flux recovery constraint given by Eq.44 as well as the equal weight and no stationary phonon assumptions the lattice phonon speed was found to be $|\vec{v_{1,3,5,7}}| = \frac{2}{3}v_g$ and $|\vec{v_{1,3,5,7}}| = \frac{2}{3}v_g\sqrt{2}$. When the lattice phonon speed were set to these value, both constraints on heat flux (in the diffusive and ballistic limits) were satisfied.

Table 2: Directional weights and lattice phonon speeds used with different schemes of LBM D2Q9.

Approach	w_0	w_1	w_2	$\lvert v_{1,\vec{3},5,7}\rvert$	$\lvert v_{2,\vec{4},6,8}\rvert$
Original	0	1/8	1/8	v_g	$v_g\sqrt{(2)}$
Alternative 1	4/9	1/9	1/36	v_g	$v_g\sqrt{(2)}$
Alternative 2	0	1/8	1/8	$\frac{2}{3}v_g$	$\frac{2}{3}v_g\sqrt{2}$

The original and alternative approaches are listed in Table 2. Heat flux obtained for Case 1 by each approach is tabulated for different Kn numbers in Table 3. In the ballistic limit, heat flux in the $+x$ direction must be equal to $4Cv_g(T1 - T2)/4 = 1.90 \times 10^9 W/m^2$ for a temperature difference of 1K between the walls. At finite Kn values, the obtained heat flux must be lower than this value and may be computed using the analytical solution [1]. At $Kn = 100$, the heat flux obtained from the DOM for all angular discretizations adopted here was $1.886 \times 10^9 W/m^2$ and slightly lower than the corresponding ballistic limit. This implies that irrespective of the adopted angular discretization, the heat flux was accurately captured since the view factor between the given temperature boundaries was correctly reproduced. The calculated heat flux for the D2Q4 and D2Q9 lattice configurations (with the weights and lattice speeds specified in the Alternative 2 scheme, Table 3) in the LBM method were $1.891 \times 10^9 W/m^2$. It was observed that computed heat fluxes in the D2Q4 and D2Q9 (Alternative 2) match those obtained from DOM (and the analytical values). However, the D2Q9 lattice fails to reproduce the correct heat flux when the weights and lattice speeds of the original and Alternative 1 discretization are used (Table 2) except in the diffuse limit $Kn \to 0$ where these are calibrated to work. Thus, due to the one-dimensional nature of the problem, the choice of the number of directions does not affect the accuracy of the heat flux.

Finally, simulations of Case 1 show that both LBM and DOM are efficient methods for the estimation of temperature for entire range of Kn when the heat transfer is one-dimensional in nature. The main difference between LBM and DOM is the

Table 3: Case 1: Ratio of heat flux in the x direction calculated at the midline (y/L=0.5) numerically for Kn=100,1 and 0.01 to heat flux calculated analytically. Analytical heat flux is calculated as $\vec{q_x}" = 1.90\times10^9 W/m^2$, $\vec{q_x}" = 10.53\times10^8 W/m^2$,$\vec{q_x}" = 2.54 \times 10^7 W/m^2$ for Kn=100, 1 and 0.01 respectively [1].

Kn	100	1	0.01
LBM(D2Q4)	0.99	1.04	1.00
LBM(D2Q9) Original	0.80	0.91	0.99
LBM(D2Q9) Alternative 1	0.66	0.81	0.99
LBM(D2Q9) Alternative 2	0.99	1.04	1.00

lack of sufficient numbers of propagation directions and the inaccessibility of three dimensional phonon propagation directions which might may cause significant problems when the heat transfer is two- or three-dimensional. We systematically investigated this variation through Case 2.

3.3.3 Case 2: 2D Phonon Transport

In this test case, shown in Fig.20(b), all the boundary temperatures were set to a constant temperature value (T=300K) except the right boundary which was set to a higher value (301 K in this case). Temperature boundary conditions were applied using the notation shown in Fig.21.

3.3.3.1 Case 2: Results

Results were obtained using DOM with a 1st order upwinding scheme and with LBM for the case shown in Fig.20(b). Figure 24 shows the contour plot of temperature for Kn=100 (a,b,c) and Kn=1 (d,e,f) obtained by LBM D2Q9 and DOM with 1×1 and 8×8 directions. The results highlighted the fact that LBM is not successful in eliminating the effects that arise from using a finite number of phonon propagation directions, i.e., ray effects. For both Kn = 1 and Kn = 100, results from the LBM simulations showed significant unphysical temperature jumps and discontinuities within the domain. However, with increased angular resolution, DOM successfully eliminated any of these gradients discontinuities that arise out of choosing an insufficient

Table 4: Case 2: Ratio of the numerically calculated heat transfer rate leaving each boundary to the analytical results for the domain shown in Fig.20(b). The analytically calculated heat transfer rates (in the ballistic limit-Kn=100) are: QA=1.905W, QB=-0.558W, QC=-0.789W, QD=-0.558W.

	QA	QB	QC	QD
LBM(D2Q4)	0.989	0	2.388	0
LBM(D2Q9)	0.993	1.133	0.795	1.133
DOM(1x1)	0.996	1.604	0.137	1.604
DOM(2x2)	0.997	1.002	0.991	1.002
DOM(4x4)	0.997	1.00	0.992	1.00
DOM(8x8)	0.997	1.00	0.994	1.00

number of directions coarse angular discretization. Also due to ballistic propagation these effects were more pronounced for domains with higher Kn numbers.

The error caused by finite number of directions was also seen by comparing heat flux at the boundaries. For Case 2, the heat transfer rate through the boundaries was calculated for $Kn = 100$ using the theory of radiation view factors [38]. We compared the heat flux leaving each boundary for $Kn \to 100$ as $Q_{ij} = A_i \sum_{i \neq j} F_{ij}(J_i - J_j)$, where F_{ij} is the view factor from surface i to surface j, A_i is the surface area and J_i, J_j are the corresponding surface radiosities.

Since the walls were thermalizing boundaries in the present case, the radiosity was $Cv_g(T - T_{ref})/4$ at a given temperature boundary. The computed heat flux using LBM and DOM leaving all four boundaries for Kn = 100 was compared to this analytically-computed ballistic value in Table 4. We found that DOM with an angular discretization of 1×1 per octant failed to account for heat transfer between surfaces and did not adequately resolve the view factors, as evidenced by the errors in QA, QB, QC, and QD. Comparison to the analytical values shows that a high level of accuracy (< 0.1 error) was obtained by a DOM discretization of 2×2 or higher.

Once again, LBM does not capture the view factors between various surfaces (like DOM 1×1) due to a limited number of phonon propagation directions. Errors greater 139% were seen when compared to the analytical solution.

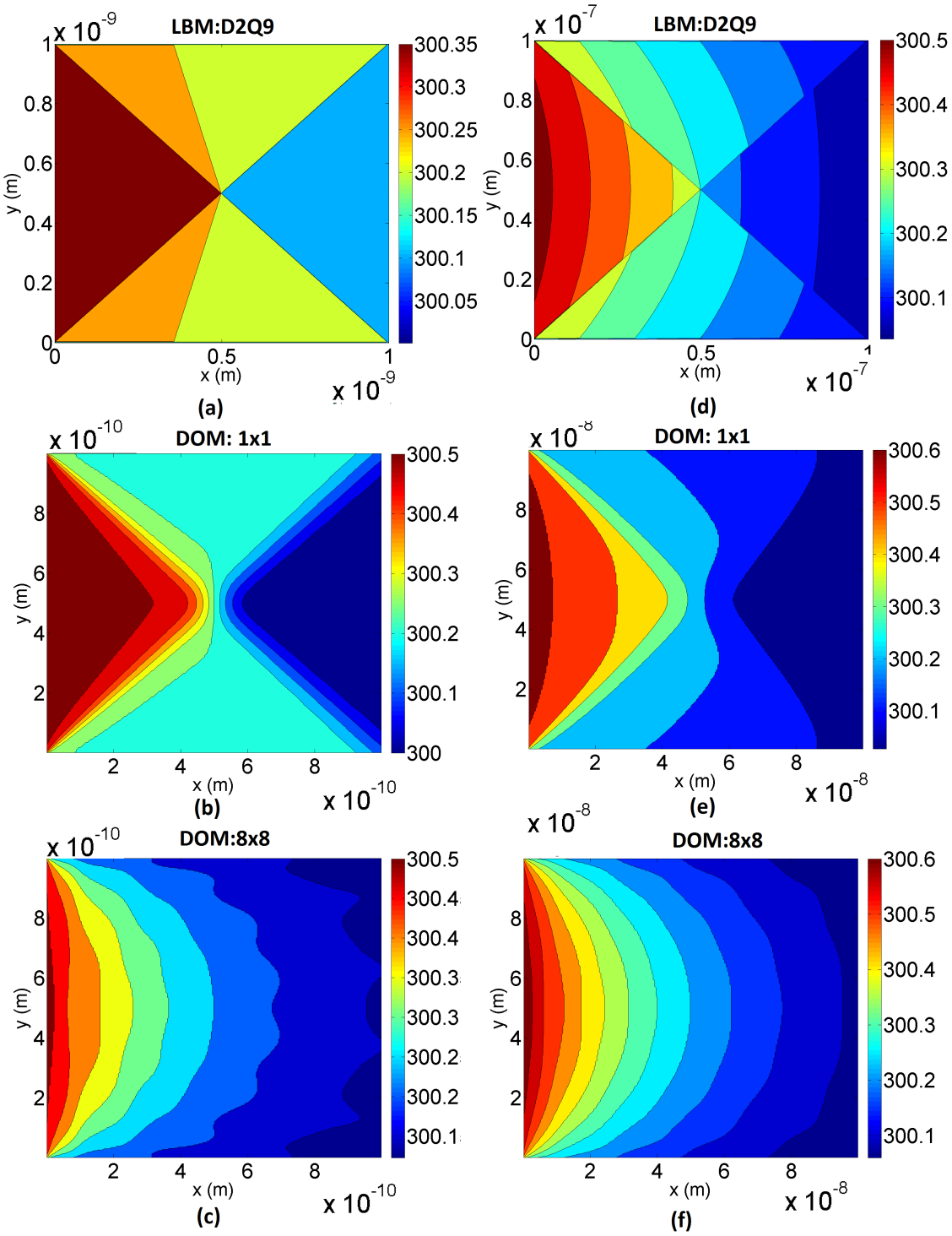

Figure 24: Temperature profiles obtained with LBM(D2Q9), DOM (1×1 directions) and DOM (8×8 directions) for a domain with Kn=100 (a,b,c) and with Kn=1 (d,e,f).

3.4 Conclusion

In this chapter two popular numerical methods used for the solution of phonon BTE, LBM and DOM were introduced. To compare their performances in ballistic to diffusive limits, two different thermal boundary value problems were utilized. It was observed that, DOM approach provided accurate results in the ballistic limit and eliminated ray effects almost entirely when enough number of directions were used. On the other hand, LBM suffered from significant errors due to insufficient number of phonon propagation directions for two-dimensional ballistic-diffusive domains. Moreover, two-dimensional LBM could not accurately calculate the heat flux unless some alternative approaches were used. It was also concluded that even with the alternative approaches presented in this section calculated heat flux in ballistic-diffusive regime will have errors associated with it. Thus, it is suggested to use DOM in order to obtain more accurate and consistent results over the entire range of Knudsen number and also for our device design purposes. However, it is important to consider the computational complexity that increases linearly with the number of directions while doing this.

CHAPTER IV

NON-GRAY PHONON BTE

In chapter 3 the BTE was solved using the gray model. In the gray model approach, all phonons are assumed to have the same group velocity and relax to equilibrium with the same relaxation time, τ. As explained earlier, non-gray models provide better temperature estimates due to the detailed handling of phonon relaxation processes.

Non-gray models that have been used so far can be divided into two categories such as semi-gray and full dispersion models. With a semi-gray model (also called a two fluid model), phonons are divided into propagating and reservoir modes. Propagating mode phonons are responsible for transporting energy while the reservoir mode phonons are purely capacitive.

Full dispersion models are the most complicated and detailed of all phonon models discussed before. The idea behind a full dispersion model is to model different phonon modes as well as their interactions with each other in a more detailed fashion. An example for this is the model suggested by Narumanchi et al. [53] that accounts for transverse and longitudinal acoustic phonons as well as optical phonons. The interactions between different phonon branches and frequencies are described by frequency-dependent relaxation times that are obtained by perturbation techniques [53]. In this work performance of gray, semi-gray and full dispersion models that are used to account for the non-Fourier effects by modeling silicon domains were also compared. It has been concluded that gray models under predict the temperature while semi-gray models over predict the temperatures in silicon and a more detailed modeling of phonon relaxation times with full dispersion model is necessary [53].

For AlGaN/GaN HFETs the localized heating effects have been addressed previously through the use of LBM and DOM solutions to the phonon BTE using a gray approximation and two fluid approximation [9]. However, as mentioned earlier the gray model is the simplest model and it does not accurately account for the energy exchange rates between different types of phonons within the lattice and the two fluid model over predicts the temperature. To solve this problem a full dispersion model should be used for GaN HFETs.

Similar to the full dispersion model applied to silicon, the dispersion effects of GaN were taken into account by splitting the dispersion curve shown in 8 into finite number of bands [40]. This way interactions between different phonon modes or groups can be modeled. Finally, with such a model, the initial electron to lattice energy scattering rates can be distributed accurately within phonon modes and their relaxation can be observed.

4.1 Canonical Form of BTE

In order to build the non-gray model canonical form of the BTE is required. The canonical BTE can be written in terms of energy density of particular phonon mode by multiplying Eq.1 by $\hbar\omega_{\mathbf{q}s}/V$, where $\omega_{\mathbf{q}s}$ is the phonon frequency, $\hbar$ is the reduced Planck's constant, and V is the volume of the unit cell in $\mathbf{k}$ space[100].

$$\frac{\partial e_{\mathbf{q}s}}{\partial t} + \vec{v_{\mathbf{q}s}} \nabla e_{\mathbf{q}s} = \hbar\omega_{\mathbf{q}s} \sum P^{ss'}_{\mathbf{q}\mathbf{q}'} \Psi_{\mathbf{q}'s'} - \mathbf{q}'''_{qs} \tag{45}$$

Here $e_{\mathbf{q}s}$ is the phonon energy density, which is a function of space and time t.

In Eq.45 the scattering term in Eq.1 is replaced by an interaction term which takes care of all the scattering events between different phonon modes. In this term scattering is defined using a scattering matrix $P^{ss'}_{\mathbf{q}\mathbf{q}'}$ that considers 3 phonon interactions only. The scattering matrix is given as [100, 40]:

$$P_{\mathbf{q}\mathbf{q}'}^{ss'} = \sum_{\mathbf{q}''s''}\sum_{\mathbf{q}'''s'''} [\frac{1}{2}\delta_{ss'}\delta_{\mathbf{q}\mathbf{q}'}(\bar{P}^{\mathbf{q}''s''}_{\mathbf{q}s,\mathbf{q}'''s'''} + \bar{P}^{\mathbf{q}'''s''',\mathbf{q}''s''}_{\mathbf{q}s} + \bar{P}^{\mathbf{q}'''s'''}_{\mathbf{q}s,\mathbf{q}''s''}) \\ - \delta_{s's'''}\delta_{\mathbf{q}'\mathbf{q}'''}(\bar{P}^{\mathbf{q}'''s'''}_{\mathbf{q}s,\mathbf{q}''s''} + \bar{P}^{qs}_{\mathbf{q}''s'',\mathbf{q}'''s'''} - \bar{P}^{q''s''}_{\mathbf{q}'''s''',\mathbf{q}s})] \\ = \Gamma_{\mathbf{q}s}\delta_{\mathbf{q}\mathbf{q}'}\delta_{ss'} + \Lambda^{ss'}_{\mathbf{q}\mathbf{q}'} \tag{46}$$

here the $\bar{P}$ terms are the intrinsic transition probabilities in isotropic continuum model and δ 's are delta functions. Γ and Λ are the diagonal and off-diagonal parts of the scattering matrix P. The intrinsic transition probability of a fusion process where $\mathbf{q}s + \mathbf{q}'s' \rightarrow \mathbf{q}''s''$ is given as [100]:

$$\bar{P}^{\mathbf{q}''s''}_{\mathbf{q}s,\mathbf{q}'s'} = \frac{\sqrt{\pi}\hbar}{4\rho^3 N_0 V}\frac{\mathbf{q}\mathbf{q}'\mathbf{q}''}{c_s c_s' c_s''}\left|A^{ss's''}_{\mathbf{q}\mathbf{q}'\mathbf{q}''}\right|^2 \bar{n}_{\mathbf{q}s}\bar{n}_{\mathbf{q}'s'}(\bar{n}_{\mathbf{q}''s''}+1)\delta_{\mathbf{q}+\mathbf{q}'+\mathbf{q}'',G}\delta(\omega_{\mathbf{q}''s''} - \omega_{\mathbf{q}s} - \omega_{\mathbf{q}'s'}) \tag{47}$$

while the transition of a fission process, where $\mathbf{q}s \rightarrow \mathbf{q}'s' + \mathbf{q}''s''$ is given as [100]:

$$\bar{P}^{\mathbf{q}'s',\mathbf{q}''s''}_{\mathbf{q}s} = \frac{\sqrt{\pi}\hbar}{4\rho^3 N_0 V}\frac{\mathbf{q}\mathbf{q}'\mathbf{q}''}{c_s c_s' c_s''}\left|A^{ss's''}_{\mathbf{q}\mathbf{q}'\mathbf{q}''}\right|^2 \bar{n}_{\mathbf{q}'s'}\bar{n}_{\mathbf{q}''s''}(\bar{n}_{\mathbf{q}s}+1)\delta_{\mathbf{q}+\mathbf{q}'+\mathbf{q}'',G}\delta(\omega_{\mathbf{q}s} - \omega_{\mathbf{q}'s'} - \omega_{\mathbf{q}''s''}) \tag{48}$$

where $\bar{n}_{\mathbf{q}s}$ is the equilibrium occupation number of phonon mode $\mathbf{q}s$, N_0 is the number of unit cells, c_s is the modal speed of the phonon, ρ is the solid density, $\delta_{\mathbf{q}+\mathbf{q}'+\mathbf{q}'',\mathbf{G}}$ and $\delta(\omega_{\mathbf{q}''s''} - \omega_{\mathbf{q}s} - \omega_{\mathbf{q}'s'})$ are the delta functions used to conserve energy and momentum respectively. $\mathbf{G}$ is the reciprocal lattice space vector including zero, thus both Umklapp and Normal processes are considered in this representation.

$$\text{Umklapp (U) Process: } \mathbf{q} + \mathbf{q}' = \mathbf{q}'' + \mathbf{G}$$

$$\text{Normal (N) Process:} \mathbf{q} + \mathbf{q}' = \mathbf{q}''$$

$A^{ss's''}_{\mathbf{q}\mathbf{q}'\mathbf{q}''}$ is the scattering strength for the fission and fusion processes involving phonons with polarizations $\mathbf{q}s$, $\mathbf{q}'s'$, and $\mathbf{q}''s''$ and is given as:

$$A^{ss's''}_{\mathbf{qq'q''}} = \frac{4\rho^2}{\bar{c}^2}\gamma c_s^2 c_{s'}^2 c_{s''}^2 \tag{49}$$

where $\bar{c}$ is an average acoustic phonon speed and γ is the Gruneisen parameter, that represents the effect of temperature change on phonon frequencies [100, 9]. Average phonon speed is found from averaging the acoustic phonon speeds using the occupation number information. Therefore average phonon speed varies with respect to temperature. By substituting Eq.49 into equations 47 and 48, using $\omega_{\mathbf{q}s} = c_s \cdot \mathbf{q}$ and replacing the delta functions with Gaussian peaks new intrinsic transition probabilities of fusion and fission processes can be obtained [40]:

$$\bar{P}^{\mathbf{q}''s''}_{\mathbf{q}s,\mathbf{q}'s'} = \frac{\sqrt{\pi}\hbar}{\rho N_0 V}\frac{\omega_{\mathbf{q}s}\omega_{\mathbf{q}''s''}}{\sigma}F^2\bar{n}_{\mathbf{q}s}\bar{n}_{\mathbf{q}'s'}(\bar{n}_{\mathbf{q}''s''}+1)\delta_{\mathbf{q}+\mathbf{q}'+\mathbf{q}'',\mathbf{G}}exp\left[-\left(\frac{(\omega_{\mathbf{q}''s''}-\omega_{\mathbf{q}s}-\omega_{\mathbf{q}'s'})}{\sigma\omega_{\mathbf{q}s}}\right)^2\right] \tag{50}$$

$$\bar{P}^{\mathbf{q}'s',\mathbf{q}''s''}_{\mathbf{q}s} = \frac{\sqrt{\pi}\hbar}{\rho N_0 V}\frac{\omega_{\mathbf{q}'s'}\omega_{\mathbf{q}''s''}}{\sigma}F^2\bar{n}_{\mathbf{q}'s'}\bar{n}_{\mathbf{q}''s''}(\bar{n}_{\mathbf{q}s}+1)\delta_{\mathbf{q}+\mathbf{q}'+\mathbf{q}'',\mathbf{G}}exp\left[-\left(\frac{(\omega_{\mathbf{q}s}-\omega_{\mathbf{q}'s'}-\omega_{\mathbf{q}''s''})}{\sigma\omega_{\mathbf{q}s}}\right)^2\right] \tag{51}$$

here σ is the broadening parameter of the Gaussian peak and $F^2 = \gamma^2\ \bar{c}^2$ is a temperature dependent fitting parameter used to match the bulk thermal conductivity.

The equilibrium phonon occupation number used in calculation of the transition probabilities is described using the Bose-Einstein distribution as:

$$\bar{n}_{\mathbf{q}s} = \frac{1}{exp\left[\frac{\hbar\omega_{\mathbf{q}s}}{k_B T_{\mathbf{q}s}}\right]-1} \tag{52}$$

where T_{qs} is the equivalent lattice temperature of mode qs.

The scattering matrix is built using the above equations and the dispersion information of GaN at a constant temperature, assuming that all phonons are in equilibrium. The scattering matrix found using this method is not symmetric since Umklapp

processes are included in its calculations. This may lead to conservation of energy issues that will be dealt with later.

$\Psi_{\mathbf{q}'s'}$ in Eq.45 is a measure of the disequilibrium of a particular phonon mode. It is defined by Srivastava as [100]:

$$n_{\mathbf{q}s} = \frac{1}{exp\left[\frac{\hbar\omega_{\mathbf{q}s}}{k_B T} - \Psi_{\mathbf{q}s}\right] - 1} \tag{53}$$

where $n_{\mathbf{q}s}$ is the phonon occupation number and T is the lattice temperature. Using Eq.52 and 53 the disequilibrium term can be obtained as:

$$\Psi_{\mathbf{q}s} = \frac{\hbar\omega_{\mathbf{q}s}}{k_B T} - \frac{\hbar\omega_{\mathbf{q}s}}{k_B T_{\mathbf{q}s}} \approx \frac{\hbar\omega_{\mathbf{q}s}(T_{\mathbf{q}s} - T)}{k_B T^2} \tag{54}$$

The last term in the equation is obtained by linearizing the disequilibrium expression and is only valid for small temperature differences.

4.2 Phonon Dispersion and ABINIT

Phonon dispersion information of GaN is required for the scattering matrix formation using above steps. Previously, ab-initio calculations were performed to obtain phonon dispersion of wurtzite GaN crystal using publicly available package, ABINIT [40].

ABINIT is capable of computing a large set of properties useful for solid state studies such as: structural and elastic properties, phase stability or instability, specific heat, and spectroscopic and vibrational properties. It performs these calculations using the Density Functional Theory (DFT) with pseudopotentials and a planewave or wavelet basis[101, 102]. Phonon dispersion modeling is performed by computing the response functions of phonons by optimization of the geometry according to density functional perturbation theory[101, 102].

Optimization was done in two steps. The first step was the structural optimization in which the equilibrium positions of atoms were calculated. In the second step, the second derivatives of the total energy for a given **q** point grid [40] was calculated.

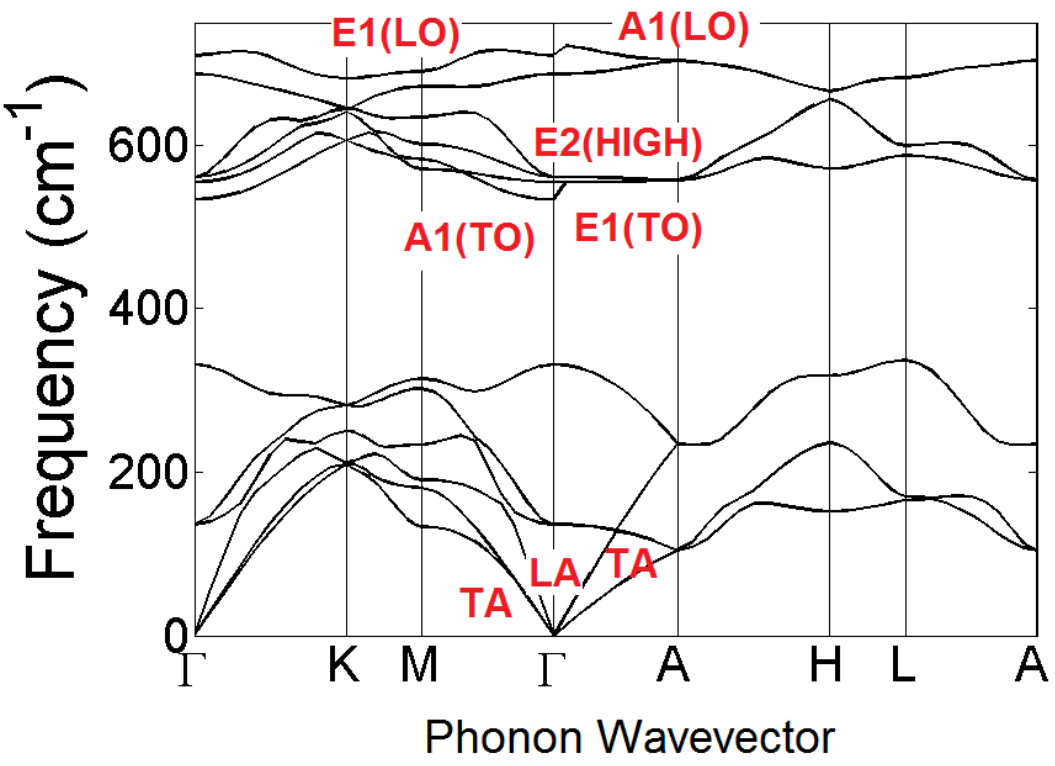

Figure 25: The dispersion curve of GaN obtained through ab-initio calculations of Abinit.

These points were generated to sample the Irreducible Brillouin Zone with evenly spaced grids. ABINIT calculated the energies (frequencies) of phonons with different polarizations at these wavevectors($\mathbf{q}$ points).

When a grid of 726 wavevectors was used the results were observed to be grid independent [40]. The phonon dispersion curve along the high symmetry directions in GaN obtained using ABINIT is shown in Fig.25, yet phonon information was available for all points in the irreducible Brillouin zone.

Currently, only some third order potential terms are available in ABINIT when this feature becomes fully available there will not be a need for fitting parameters such as Gruneisen parameter to obtain accurate thermal conductivity. Properties used in simulations and other details of ABINIT simulations used to obtain phonon dispersion used in this study are given elsewhere [40].

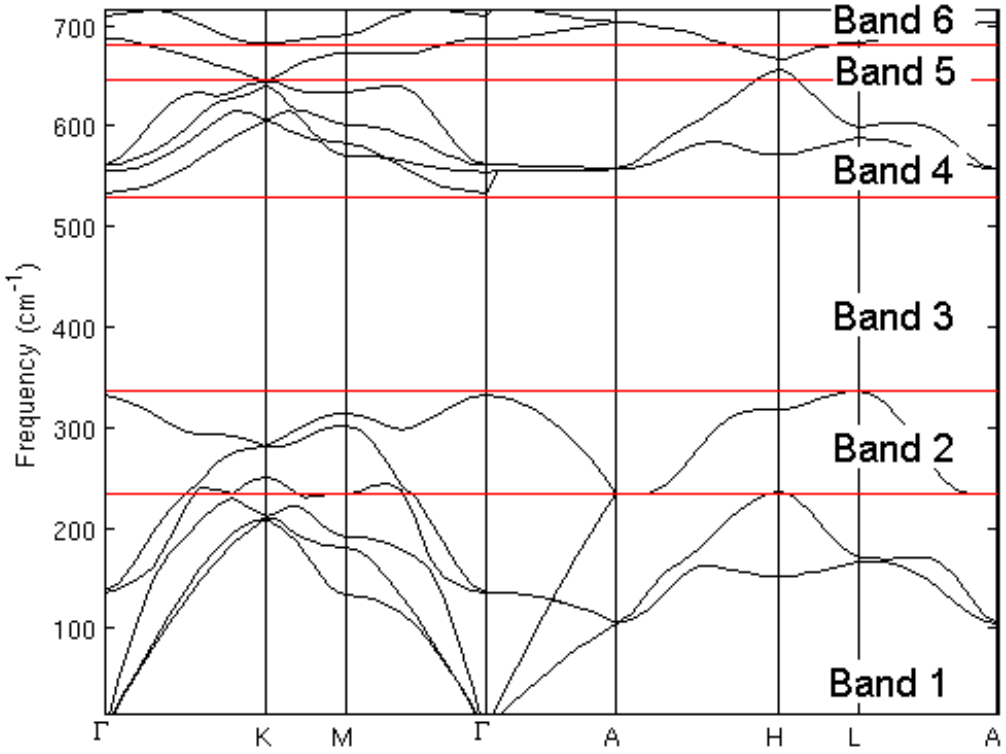

Figure 26: The dispersion curve of GaN discretized into 6 phonon bands. Horizontal red lines mark the phonon band boundaries.

4.3 Non-Gray Phonon BTE with Phonon Bands

Due to the difficulty of modeling each phonon mode in a crystal, phonon bands were used to understand the non-equilibrium phonon transport in the crystal [40]. Grouping of the phonons into bands was done by splitting the phonon dispersion curve into energy bands as mentioned earlier.

A one band model corresponds to gray model and it is desired to use more bands for a more detailed model of the phononic interactions. Figure 26 illustrates GaN phonon dispersion split into 6 bands. The red lines in Fig.26 marks the phonon group boundaries. In Fig.26, 3rd band is lying right in the phononic band gap and is empty. Empty bands were neglected in all calculations.

Grouping the phonons based on their energy causes the directionality of the mode

to be lost therefore, the non-gray model is an isotropic model. As a result of this phonon BTE should be rewritten for non-gray model:

$$-\frac{\partial e_g}{\partial t} - v_g \vec{S}(\Omega) \nabla e_g(\Omega) = \frac{\hbar}{4\pi V} \sum_{g'} \int_{4\pi} P_{gg'} \Psi_{g'}(\Omega) \delta(\Omega - \Omega') d\Omega' - G_\Omega \tag{55}$$

where g represent the band, S is the direction cosine of the solid angle Ω , v_g is the band group velocity and the $G(\Omega)$ is the energy generation rate in that particular phonon band and solid angle. $P_{gg'}$ is the band-to-band scattering matrix and $\Psi_{g'}$ is the band disequilibrium term. They can be related to individual phonon scattering matrix and disequilibrium terms by using the constraint:

$$P_{gg'} \Psi_{g'} = \sum_{\mathbf{q}s\epsilon g} \omega_{\mathbf{q}s} \sum_{\mathbf{q}'s'\epsilon g'} P^{ss'}_{\mathbf{q}\mathbf{q}'} \Psi_{\mathbf{q}'s'} \tag{56}$$

and band disequilibrium term can be obtained with a slight modification of Eq.(7):

$$\Psi_g = \frac{\hbar \omega_g (T_g - T)}{k_B T^2} \tag{57}$$

In this way, no interaction within a band will be lost. The derivation details can be found elsewhere [40]. Finally the band-to-band scattering matrix was derived to be in the form:

$$P_{gg'} = \frac{1}{\omega_{g'}} \sum_{\mathbf{q}s\epsilon g} \omega_{\mathbf{q}s} \sum_{\mathbf{q}'s'\epsilon g'} P^{ss'}_{\mathbf{q}\mathbf{q}'} \omega_{\mathbf{q}'s'} \tag{58}$$

Using those relations and the temperature specific heat relation to relate the band temperature T_g and lattice temperature, T to band energy density e_g and total energy e, the steady state non-gray phonon BTE was obtained as:

$$-v_g \vec{S}(\Omega) \cdot \nabla e_g(\Omega) = \frac{\hbar^2}{4\pi V} \sum_{g'} P_{gg'} \omega_{g'} \left[\frac{e_{g'}(\Omega)}{C_{g'}} - \frac{e}{C} \right] - G_g(\Omega) \tag{59}$$

where $C_{g'}$ is the specific heat of the band and C is the total specific heat.

$$\sum_{g}\sum_{g'}\sum_{g''} P_{gg'}\omega_{g'}(\delta_{g'g''} - C_{g'}/C)e_{g''} = 0 \tag{60}$$

where N is the total number of phonon bands used for the model.

4.4 Calculating the Band Properties

Thermal properties of GaN used in the simulations are extremely important to understand the heat carrying mechanism in GaN. The values used in multiscale thermal simulations should be in good agrement with theoretical and experimental values. Thus, the thermal properties such as thermal conductivity, specific heat, relaxation time, and mean free path for models containing multiple bands as well as a single band(gray) model were analyzed. Specifically, a single band model which groups all phonons into one, a 3 band model which divides the dispersion curve shown in Fig.26 into 3 bands instead of 6 from using the boundaries just above and below the bandgap in Fig.26, and a 6 band model shown in Fig.26 were analyzed and compared.

The properties of each band such as specific heat, thermal conductivity, group velocity and thermal conductivity were different from each other. Details of how they were calculated and their comparison with each other and to other models are explained next.

4.4.1 Specific Heat

The specific heat of a band was calculated from the specific heat of individual phonon modes that lies within that band as in Eq.61. Looking at this equation, the specific heat of a band is directly proportional to population of that band, phonon occupation number of a particular phonon and thus inversely proportional to frequency of phonon mode. The total specific heat of the lattice can be found by adding all the band specific heats as:

$$C_g = \sum_{\mathbf{q}s\epsilon g} C_{\mathbf{q}s} = \sum_{\mathbf{q}s\epsilon g} k_B \left[\frac{\hbar\omega_{\mathbf{q}s}}{k_B T}\right]^2 \frac{exp\left[\frac{\hbar\omega_{\mathbf{q}s}}{k_B T}\right]}{\left[exp\left[\frac{\hbar\omega_{\mathbf{q}s}}{k_B T}\right] - 1\right]^2} \tag{61}$$

Total specific heat of the lattice was calculated by adding specific heats of all phonon modes which is $2.57 \times 10^6 J/m^3 K$. This was equal to the band specific heat of 1-band model. For the 3 band model (where the middle band is empty) the specific heat of the upper band was $1.66 \times 10^6 J/m^3 K$ and the lower band was $0.91 \times 10^6 J/m^3 K$ adding up to a total specific heat of $2.57 \times 10^6 J/m^3 K$. This shows that about 1/3 of the lattice energy is stored by phonons below the bandgap at T=300K. More detailed analysis of the distribution of specific heat was performed by comparing band specific heats of a 6 band model shown in Fig.26. Specific heats of bands are shown with a bar plot in Fig.27.

It was observed that band 2 has the highest specific heat since in band 2, a large number of phonon modes are present. On the other hand, band 5 had the lowest specific heat since it had the lowest frequency and occupation of phonons.

4.4.2 Group Velocity

The speed of the phonon mode v_{qs} can be found from the gradient of the phonon dispersion curve (i.e. $v_{qs} = \partial\omega/\partial k$. The band group velocities were found by averaging the phonon velocities within a phonon band. For a one band(gray) model it was found as $1831 m/s$. For a 3 band model, the lower band group velocity was calculated as 1254m/s while the upper phonon band group velocity was calculated as 578m/s. This shows that faster moving conductive phonons were the phonons below the phononic bandgap. Again with a larger number of bands, a more detailed picture of phonon speeds was obtained. For a 6 band model the group velocities of 5 non empty bands were given in Fig.27.

As evident from the dispersion curve of GaN, given in Fig.27 phonon dispersion in bands 5 and 6 had very small gradients. On the contrary, phonon dispersion in

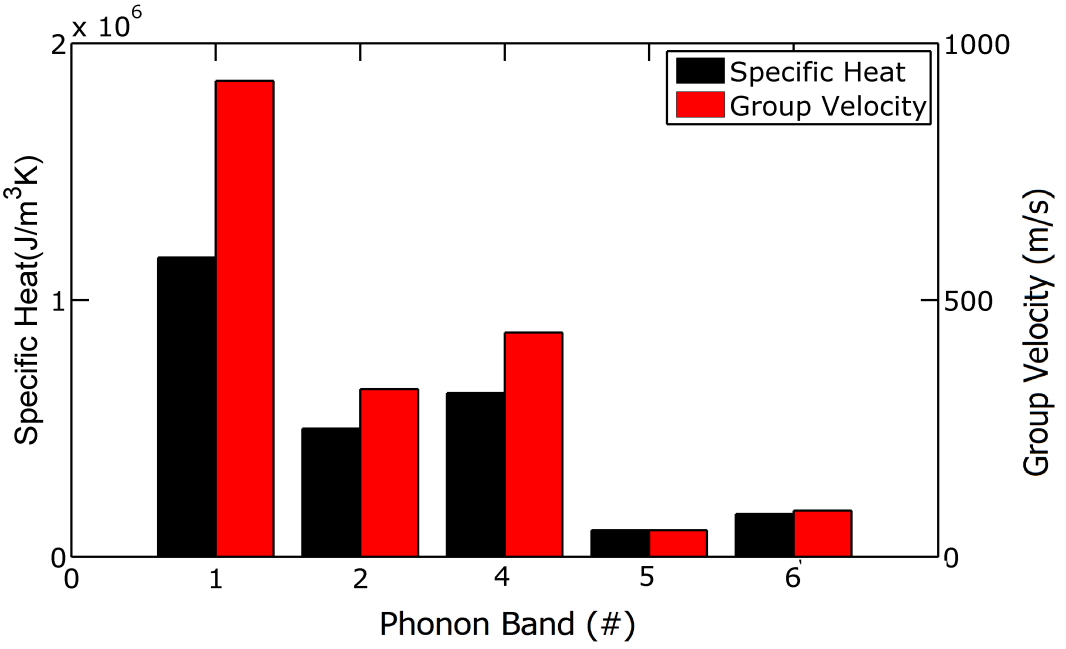

Figure 27: Calculated specific heats and group velocities of GaN phonon bands in 6 band non-gray phonon model(3rd band is empty and is not shown).

band 1 had high gradients thus group velocity was calculated to be highest.

4.4.3 Thermal Conductivity

Thermal conductivity of the phonon bands were computed from the band-to-band scattering matrix and is extremely important. Yet, before we start the discussion of it is very important to make sure that the total conductivity of the bands match the bulk thermal conductivity. Figure 28 shows the experimental thermal conductivities of wurtzite GaN with varying temperature.

In this thesis, we performed non-gray simulations using a constant thermal conductivity of 150W/mK which corresponds to thermal conductivity of wurtzite GaN at room temperature ($T = 300K$)[15]. As discussed before Gruneisen parameter can be used with scattering matrix, $P^{ss'}_{\mathbf{qq'}}$, to match this bulk thermal conductivity. However, calculation of the bulk thermal conductivity from full scattering matrix is difficult since it is difficult to get the inverse of this scattering matrix due to the large number of elements[40]. Thus, instead of correcting the phonon scattering matrix with

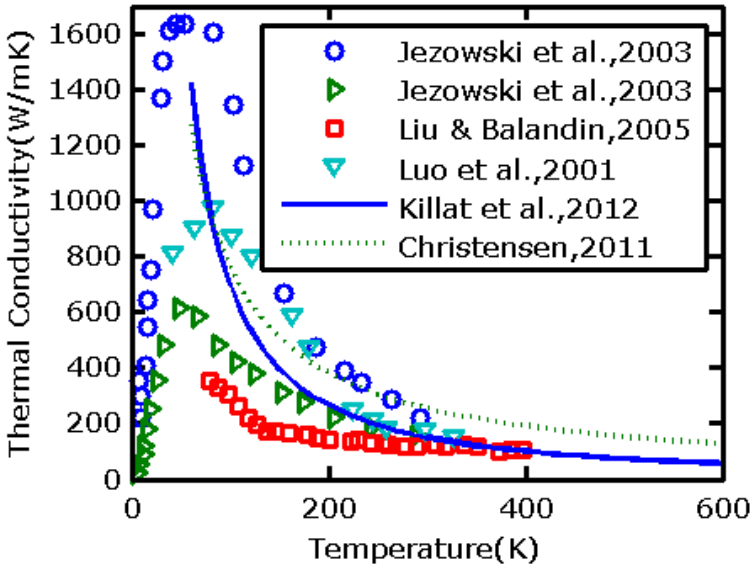

Figure 28: Temperature dependent thermal conductivity of GaN [9, 14, 15, 16, 17].

the Gruneisen parameter, we calculated the band-to-band scattering matrix using an unfitted phonon scattering matrix. Later the band-to-band scattering matrix was corrected by a factor similar to Gruneisen parameter since it was easier to take the inverse of band-to-band scattering matrix. The unfitted thermal conductivity was calculated from band-to-band scattering matrix as below, where detailed derivation can be found[40]:

$$k_{unfitted} = \frac{1}{3}\frac{k_B T_0^2 V}{\hbar^2}\sum_g v_g \sum_{g'} \mathbf{A}^{-1} C_{g'} v_{g'} \tag{62}$$

where $\mathbf{A}$ is a matrix given as:

$$\mathbf{A} = \frac{P_{gg'}\omega_{g'}}{C'_g} \tag{63}$$

First the unfitted thermal conductivity,$k_{unfitted}$ was calculated using the unfitted band-to-band scattering matrix $P_{gg'}$ using the unfitted scattering matrix, found by Eq.46 and the Eq.58. Later a fitting parameter was found from the ratio of the unfitted and the bulk thermal conductivities and applied to $P_{gg'}$ to obtain the new

scattering matrix $P^*_{gg'}$. The new $P^*_{gg'}$ when used with Eq.62 gives the bulk thermal conductivity of $150W/mK$. After, this correction was done new scattering matrix was used for the non-gray phonon BTE equation given in Eq.59. The band thermal conductivities were found using this new scattering matrix with the below equation:

$$k_g = \frac{1}{3}\frac{k_B T_0^2 V}{\hbar^2} v_g \sum_{g'} \mathbf{A}^{-1} C_{g'} v_{g'} \tag{64}$$

where new $\mathbf{A}$ matrix was recalculated with the new scattering matrix using Eq.63. Thermal conductivities of the bands found using this method were also compared. For example, for a 1 band model, thermal conductivity of the only band was equal to the total thermal conductivity of $150W/mK$. For a 3 band model, the phonon band below the bandgap had thermal conductivity of $134W/mK$ carrying most of the heat while the phonon band above the bandgap had a thermal conductivity of $16W/mK$.

For a 6 band model, phonon band with the highest conductivity was band 1 as seen in Fig.29. This was due to high specific heat and group velocity of the phonon band. The lowest thermal conductivity was observed for the bands with the highest frequency due to their low specific heat and group velocities.

4.4.4 Relaxation Time

Relaxation time of phonon bands can be calculated from other band properties such as specific heat, group velocity, and thermal conductivity using the equation below[40]:

$$k_g = \frac{1}{3} v_g^2 C_g \tau_g \tag{65}$$

For the gray model, the relaxation time was calculated as 52ps and for a 3 band model, the relaxation time of the lower band and upper band were given as 15 and 16ps respectively. For a 6 band model bands that were close to the bandgap have relatively short relaxation times since they can exchange energy with each other easily. However, as phonons move away from the bandgap, which is the case for bands 5 and

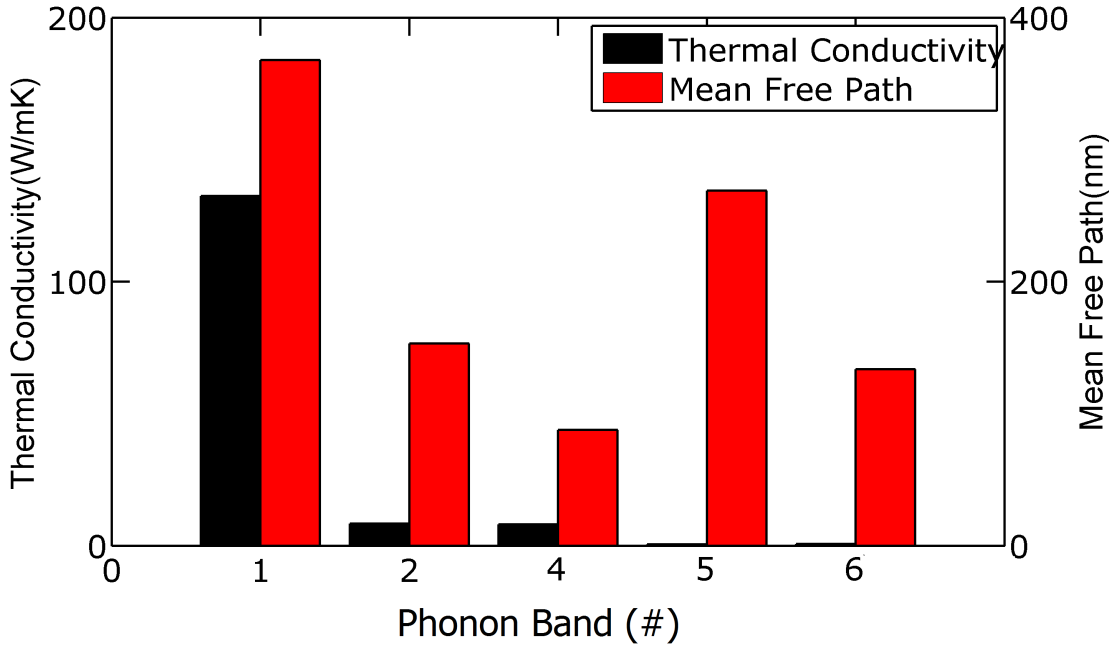

Figure 29: Calculated thermal conductivity and mean free paths of GaN phonon bands in 6 band non-gray phonon model(3rd band is empty and is not shown).

6, the relaxation times increased.

4.4.5 Mean Free Path

Mean free path of phonon groups were calculated from phonon group velocity and relaxation time using $\Lambda = v_g\tau$. Mean free path of 1 band model was calculated as 96nm. For 3 band model the mean free path was calculated as 192nm and 94nm for the lower and upper phonon bands respectively. For a 6 band model much higher phonon mean free paths were computed. For example band 1 which was highly conductive has mean free path of 550nm whereas minimum mean free path was observed for 5th phonon band as 61nm. This shows that when 6 band model was used most of the heat was carried away with phonons with mean free paths larger than 500nm[9]. In order to validate this, thermal conductivities of individual phonon modes were calculated and accumulation of thermal conductivity with respect to mean free path of phonons was obtained.

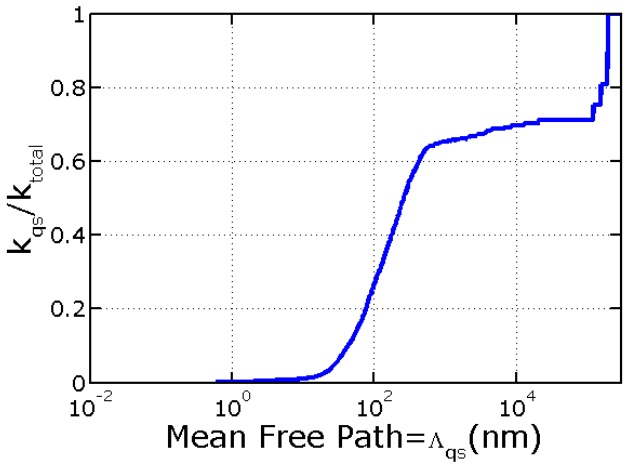

Figure 30: Thermal conductivity accumulation with respect to mean free path of phonons in wurtzite GaN at 300K.

As stated before it is difficult to calculate the relaxation times of individual phonon modes due to size of the scattering matrix. However, Single Mode Relaxation Time (SMRT) approximation can be used to get an estimate. With this approximation all modes except the mode for which the relaxation time is calculated are in equilibrium. With this approximation relaxation time of phonon mode $\mathbf{q}s$ is given as:

$$\tau_{\mathbf{q}s} = \frac{k_B T_0^2 V C_{\mathbf{q}s}}{\hbar^2 \Gamma_{\mathbf{q}s} \omega_{\mathbf{q}s}^2} \tag{66}$$

where $\Gamma_{\mathbf{q}s}$ is the diagonal portion of scattering matrix.

Using this relaxation time and previously computed phonon group velocity and specific heat thermal conductivity of phonon mode $\mathbf{q}s$ was calculated as:

$$k_{qs} = \frac{1}{3} v_{qs}^2 C_{qs} \tau_{qs} \tag{67}$$

4.5 Numerical Solution of Non-Gray Phonon BTE

In chapter 3 discretization of gray phonon BTE using FVDOM was explained. Using a similar technique, the phonon BTE written for individual phonon groups was

discretized. Directional discretization leads to the following directionally discretized non-gray phonon BTE:

$$-v_g\vec{S}_i\nabla e_{gi} = \frac{\hbar^2}{4\pi V}\sum_{g'} P_{gg'}\omega_{g'}\left[\frac{e_{g'i}(\Omega)}{C_{g'}} - \frac{e}{C}\right] - G_{gi} \tag{68}$$

$$e = \sum\sum w_i e_{gi} = CT \tag{69}$$

$$v_g\vec{S}_i\nabla e_{gi} = \sum_{g'}\sum_{i'} K_{gg'ii'}e_{g'i'} - G_{gi} \tag{70}$$

$$K_{gg'ii'} = \frac{\hbar^2}{4\pi V}\left[\frac{P_{gg'}\omega_{g'}}{C_{g'}}\delta_{ii'} - \frac{w_i'}{C}\sum_{g''} P_{gg''}\omega_{g''}\right] \tag{71}$$

using the LUS. After substituting Eq.35 into Eq.31 by taking account the phonon propagation directions Eq.72 was obtained:

$$\begin{aligned} &a_{gi}^P e_{gi}^P - a_{gi}^E e_{gi}^E - a_{gi}^W e_{gi}^W - a_{gi}^N e_{gi}^N - a_{gi}^S e_{gi}^S - a_{gi}^{EE} e_{gi}^{EE} - \\ &a_{gi}^{WW} e_{gi}^{WW} - a_{gi}^{NN} e_{gi}^{NN} - a_{gi}^{SS} e_i^{SS} + \sum_{g'}\sum_{i'} K_{gg'ii'}e_{g'i'}^P + G_{gi}^P = 0 \end{aligned} \tag{72}$$

For LUS scheme the coefficients $a_{gi}^E, a_{gi}^S, a_{gi}^W, a_{gi}^N, a_{gi}^{EE}, a_{gi}^{SS}, a_{gi}^{WW}, a_{gi}^{NN}$, and a_{gi}^P are given as:

$$a_{gi}^E = max(\frac{-2v_g\mu_i}{\Delta x}, 0) \tag{73a}$$

$$a_{gi}^W = max(\frac{2v_g\mu_i}{\Delta x}, 0) \tag{73b}$$

$$a_{gi}^N = max(\frac{-2v_g\eta_i}{\Delta y}, 0) \tag{73c}$$

$$a_{gi}^S = max(\frac{2v_g\eta_i}{\Delta y}, 0) \tag{73d}$$

$$a_{gi}^{EE} = max(\frac{-v_g\mu_i}{2\Delta x}, 0) \tag{73e}$$

$$a_{gi}^{WW} = max(\frac{v_g\mu_i}{2\Delta x}, 0) \tag{73f}$$

$$a_{gi}^{NN} = max(\frac{-v_g\eta_i}{2\Delta y}, 0) \tag{73g}$$

$$a_{gi}^{SS} = max(\frac{v_g\eta_i}{2\Delta y}, 0) \tag{73h}$$

$$a_{gi}^{P} = max(\frac{3v_g\mu_i}{2\Delta x}, 0) + max(\frac{-3v_g\mu_i}{2\Delta x}, 0) + max(\frac{3v_g\eta_i}{2\Delta y}, 0) + max(\frac{3v_g\eta_i}{2\Delta y}, 0) \quad (73i)$$

where μ_i an η_i are x and y components of unit vector along direction i.

4.5.1 Boundary Conditions

4.5.1.1 Temperature Boundary Condition

In the band to band model temperature boundary conditions were applied using the same techniques as in gray models. The inward facing phonon energy densities of all phonon bands were set to the band energy at the boundary temperature.

$$e_{gi}^{in} = C_g T_b \quad (74)$$

For certain higher order schemes (LUS,QUICK) the nodal energy densities outside the domain were required. In those conditions it was assumed that the temperature outside the domain was also equal to the boundary temperature. This was a good assumption when the nodal spacing was low enough.

4.5.1.2 Specular Reflection Boundary Condition

Implementation of a specular boundary condition was relatively easy. This type of boundary condition was used mainly to represent symmetry. When a specular boundary condition is used at a boundary then the inward facing phonon energies of bands are taken equal to the outward facing phonon energy densities at the boundary along the mirrored direction i'. This is shown in Fig.22(a) for gray model. For non-gray model each phonon band was reflected using the same principle:

$$e_{gi}^{in} = e_{gi_{mirror}}^{out} \quad (75)$$

Outward moving phonon energy density was computed from the appropriate numerical scheme (LUS,QUICK etc.) explained in chapter 3. Again for higher order

schemes nodal energy densities of outer nodes were required to compute the energy densities at the faces of control volumes close to the boundaries. In this case the energy densities at outer nodes were obtained assuming the specular reflecting boundary was a symmetry plane and the nodal energies on the left and right sides of this boundary were equal to each other.

4.5.1.3 Diffuse Reflection Boundary Condition

Application of a diffuse reflection boundary condition is relatively difficult, yet it is important to model real domain boundaries[86]. At diffusely reflecting boundary inward facing energy is equal to the equilibrium energy of the boundary. In this work, it was assumed that inward facing energy of each band was equal to the equilibrium energy of that band only. Thus, scattering between phonon bands was also neglected at the boundary. This can be mathematically expressed as:

$$e_{gi}^{in} = \sum_{i'} w_{i'} e_{gi'} \tag{76}$$

$$e_{gi}^{in} = \sum_{i'} w_{i'} e_{gi'}^{out} a_{i'} + \sum_{i'} w_{i'} e_{gi'}^{in} (1 - a_{i'}) \tag{77}$$

where $a_i = 1$ when $s_i \cdot n < 0$ and 0 otherwise. Since outward moving phonon energy density is given as $e_{gi'}^{out} = e_P + (e_P - e_{inner})/2$ in LUS scheme Eq.77 can be rewritten as:

$$e_{gi}^{in} = \frac{\sum_{i'} w_{i'} e_P + (e_P - e_{inner})/2 a_i}{1 - \sum_{i'} w_i (1 - a_i)} \tag{78}$$

4.5.2 Matrix Formulation and Solution

Equation (72) can be solved using implicit or explicit techniques. Fully implicit techniques are not recommended to solve it since the number of degrees of freedom is very high even for relatively small problems [40]. For instance, when a domain is

discretized into 100×100 control volumes, angular discretization of 12 directions (i.e. S3 quadratures) and dispersion curve discretisation into 6 bands (with 5 non-empty bands) total number of degrees to be solved is $N_{dir} \times N_g \times N_x \times N_y = 12 \times 5 \times 100 \times 100 = 600,000$. As a result of this, semi implicit methods are suggested. For this it is required to put the Eq.72 in the form $\mathbf{Ae} = \mathbf{b}$,where $\mathbf{e}$ is the energy density vector.

$$\begin{bmatrix} a_{gi}^P + K_{ggii} & -a_{gi}^E & . & -a_{gi}^S & K_{gg'ii'} & . \\ -a_{gi}^W & a_{gi}^P + K_{ggii} & -a_{gi}^E & . & . & K_{gg'ii'} \\ . & . & . & . & . & . \\ & . & . & . & . & . \\ & . & . & . & . & . \\ & . & . & . & . & . \\ & . & . & . & . & . \\ & . & . & . & . & . \\ & . & . & . & . & . \\ & . & . & . & . & . \\ & . & . & . & a_{gi}^P + K_{ggii} & -a_{gi}^E \\ & K_{gg'ii'} & & & -a_{gi}^W & a_{gi}^P + K_{ggii} \end{bmatrix} \begin{bmatrix} e_{1,1}^{1,1} \\ . \\ e_{Nx,1}^{1,1} \\ . \\ e_{Nx,Ny}^{1,1} \\ e_{1,1}^{1,2} \\ . \\ e_{Nx,Ny}^{1,Ndir} \\ e_{1,1}^{2,1} \\ . \\ e_{Nx,Ny}^{Ng,Ndir} \end{bmatrix} = \begin{bmatrix} b_{1,1}^{1,1} \\ . \\ . \\ . \\ . \\ . \\ . \\ . \\ . \\ . \\ b_{Nx,Ny}^{Ng,Ndir} \end{bmatrix} \tag{79}$$

where $\mathbf{b}$ array is composed from generation and boundary conditions at respective control volumes:

$$\mathbf{b} = \mathbf{Gen} + \mathbf{Bound} \tag{80}$$

In this condition matrix $\mathbf{A}$ given at Eq.79 is still very big to solve. Thus, it is decomposed into smaller matrices and solved one direction and band at a time. In this case the system of equation can be rewritten as:

$$\mathbf{A}_{gi} = \begin{bmatrix} a_{gi}^P + K_{ggii} & -a_{gi}^E & . & -a_{gi}^S & . & . \\ -a_{gi}^W & a_{gi}^P + K_{ggii} & -a_{gi}^E & . & . & . \\ . & . & . & . & . & . \\ . & . & . & . & a_{gi}^P + K_{ggii} & -a_{gi}^E \\ . & . & . & . & -a_{gi}^W & a_{gi}^P + K_{ggii} \end{bmatrix} \tag{81}$$

The new equation system looks like:

$$\mathbf{A}_{gi}\mathbf{e}_{gi} = \mathbf{b}_{gi} \tag{82}$$

where the new $\mathbf{b}_{gi}$ will be computed from the $\mathbf{b}$ in Eq.80 and also the scattering with other bands and directions as:

$$\mathbf{b}_{gi} = \begin{bmatrix} b_{1,1}^{g,i} \\ . \\ . \\ . \\ b_{Nx,Ny}^{g,i} \end{bmatrix} + \mathbf{Scat}_{gi}\mathbf{e} \tag{83}$$

where $\mathbf{Scat}_{gi}$ represents the remaining part of the matrix $\mathbf{A}$ of Eq.79for each direction and band and $\mathbf{e}$ represents the energy densities. Since the boundary matrix has to be updated after each solution an iterative technique was used to solve the system of equations given by Eq.82. To reduce the memory usage the generalized minimum residual (GMRES) method of MATLAB was used at each iteration step. GMRES is an extension of the minimal residual method (MINRES), which is only applicable to symmetric systems, to unsymmetric systems [103]. GMRES is slower than a direct solution, however it provides results with reasonable accuracy while reducing the memory requirement [103]. Using a preconditioner is desired in many simulations

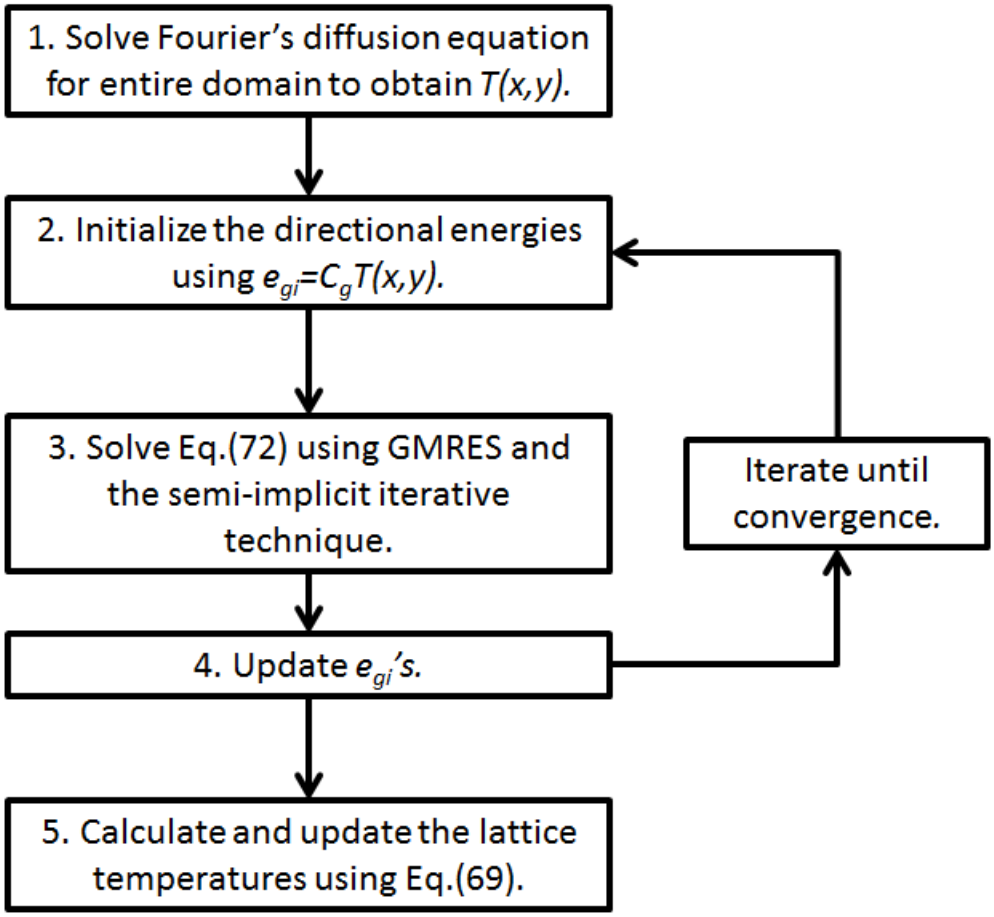

Figure 31: Solution algorithm for the phonon BTE solver.

thus incomplete LU decomposition $\mathbf{A}_{gi}$ before starting the solution. The summary of the solution method explained here is given in Fig.31.

4.6 Conclusion

In this chapter non-gray phonon modeling was introduced by discretizing the phonon dispersion into bands and calculating their interaction strengths. Moreover, thermal properties such as specific heat, thermal conductivity, group velocity, and relaxation time of phonon bands were calculated and compared. Finally, numerical solution technique for the non-gray model was discussed.

CHAPTER V

MULTISCALE THERMAL MODEL

So far, the gray and non-gray phonon models that can be used to investigate the hotspot temperature in devices has been discussed. Although these methods give better temperature estimates at the hotspot area by accounting for the ballistic effects computational challenges caused by the high degree of freedom of phonon BTE numerical solutions exist. As a result, many previous simulations have been limited to domains where only ballistic-diffusive phonon transport effects are present. However, this may lead to the exclusion of the effects of the far field system boundaries that can impact the system level and local level responses. For AlGaN/GaN HFETs it is known that substrates, heat sinks, and boundary resistances between these layers effect the temperature and the reliability of devices.

In order to include far field system boundary effects with reasonable computational cost one can use a non-uniform mesh. However, to do this the model should be significantly changed. Moreover, it will be redundant to solve the BTE for elements that are big enough and far away from the ballistic effects since they can be modeled with diffusive models.

To overcome these computational issues, several groups have implemented various multiscale solutions solving ballistic-diffusive phonon transport in a small domain of interest, while addressing the remaining portions of the system using a diffusive transport model [104, 9]. However, a systematic study including the limitations of such multiscale models in evaluating the domains with localized hotspots has not been investigated in detail. In this chapter a coupled phonon BTE and a Fourier diffusion equation solver are introduced and a systematic study of its limitations are

discussed. Domains with localized heat generation were investigated to understand the applicability of such multiscale methods for simulations of devices with localized heat generation such as AlGaN/GaN HFETs.

5.1 Direct Coupling of BTE and Fourier Solvers

Previous studies have shown that ballistic-diffusive effects present in the vicinity of a heat generation region smaller than the phonon mean free path will cause higher peak temperatures to occur within the hotspot region, but far removed from this region, the temperature response will relax to one described by Fourier diffusion [105]. Since heat transport becomes diffuse after a certain distance, it is redundant and computationally expensive to model such far field areas using gray phonon BTE solutions. As a result, a multiscale model that involves partitioning of the domain into two sub domains as illustrated in Fig.32 was proposed. The inner domain includes the heat generation region where the ballistic-diffusive effects are dominant and is thus referred to as the BTE domain. An outer domain that contains the rest of the geometry where ballistic effects are negligible is called the Fourier domain. The two domains were coupled together at coupling nodes where the temperature and energy fluxes must be equal. The discretization of the relevant thermal transport equations required for the numerical simulations and the coupling techniques will be explained in the next section.

5.1.1 BTE Domain

In the BTE domain shown in Fig.32, the gray phonon BTE equation, Eq.4 is solved to account for ballistic-diffusive effects. As discussed in chapter 3 the discrete ordinates method(DOM) was used for the discretization in angular domain since it eliminates ray effects by providing more flexibility in directional discretization. Equation 36, with correct implementation of boundary conditions, was solved to give e_i values for all nodes and directions. These directional energies were finally be used for calculation

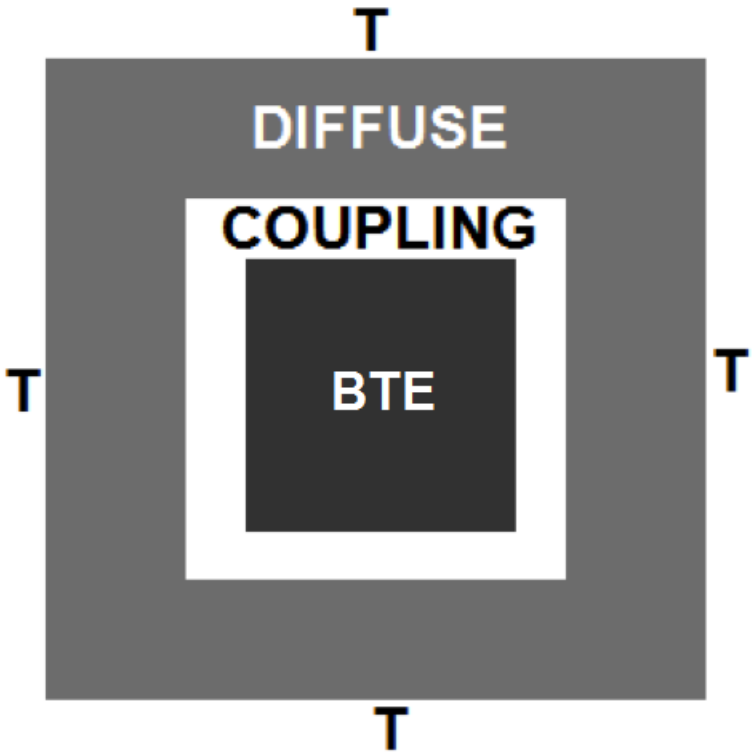

Figure 32: Domains of multiscale Fourier - gray phonon BTE solver. BTE region represents the region where gray phonon BTE is solved, diffuse region represents the region where Fourier's heat diffusion equation is used and the coupling region represents the region where these two regions were coupled to each other.

of lattice energy and temperature using Eq.30. Application of boundary conditions was done through the coupling procedure used to connect the BTE domain to the Fourier domain. Coupling procedure will be explained later.

5.1.2 Fourier Domain

Outside the domain where sub-continuum effects were present, i.e. in the diffuse domain, Fourier's diffusion equation was solved due to its computational advantages. The common form of the heat diffusion equation with isotropic thermal conductivity is:

$$k\Delta^2 T = q''' \tag{84}$$

where k is the bulk isotropic thermal conductivity, T is the lattice temperature and q''' is the volumetric heat generation term. Using the notation given in Fig.16(a) when two-dimensional heat diffusion is discretized, Eq.84 takes the form:

$$k\frac{\Delta y}{\Delta x}(2T_P - T_E - T_W) + k\frac{\Delta y}{\Delta x}(2T_P - T_N - T_S) = q'''\Delta x\Delta y \tag{85}$$

Details of how to implement temperature boundary condition and the heat flux boundary condition to a given boundary when solving Eq.85 are given elsewhere[106] and omitted in this work.

5.2 Coupling Method and Solution Algorithm

As shown in Fig.32 the diffuse domain encloses the BTE domain and the coupling region between the two provides the boundary conditions required to solve the Eq.36 in the BTE domain. The size of the BTE domain should be large enough such that at the domain boundaries, the BTE solution and Fourier solution provide the same temperatures and heat fluxes at these coupling nodes. Figure 33(a) and (b) illustrate the coupling region and how coupling is performed through boundary conditions.

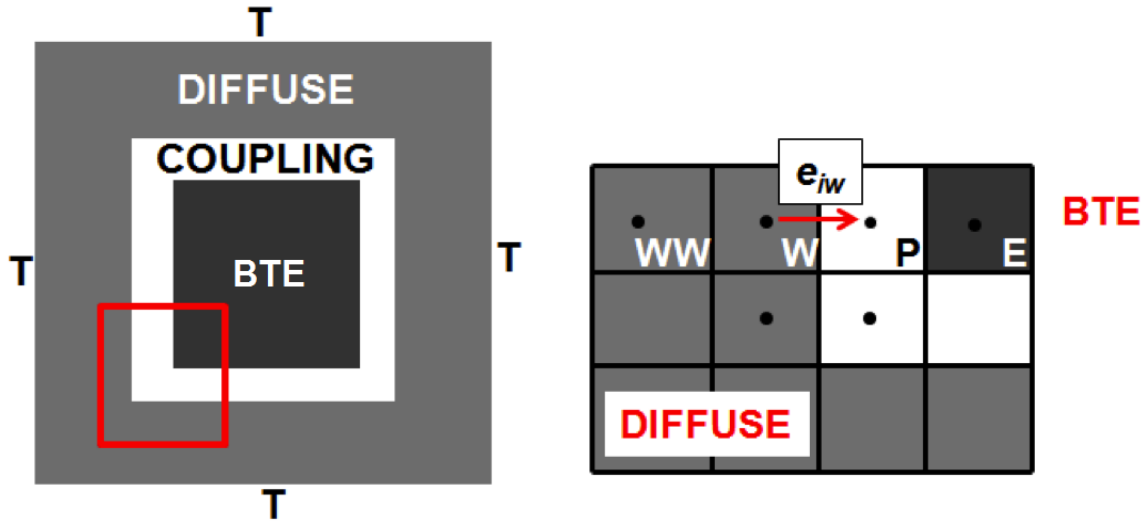

Figure 33: Coupling method for multiscale model (a) General view of the domain modeled. (b)Detailed view of the coupling node P, where west face energy density in direction ($+x$ direction) is computed from the temperatures of neighboring nodes W and WW shown in the figure.

The multiscale thermal model follows the same solution algorithm given in Fig.31 with some differences. It starts with initializing the temperature and directional energies in the Fourier and BTE domains by first solving the entire system using Eq.85. After isotropic initialization of energy densities as using $e_{gi} = C_g T(x, y)$, Eq.36 was solved for all nodes and directions of the BTE domain with the given coupling procedure.

The boundary conditions implemented on the BTE domain or the inward phonon intensity at the boundaries depicted in Fig.21 was computed using the LUS scheme given in Eq.86. Using this scheme e_i^w shown in Fig.33(b) was obtained as:

$$e_i^w = e_i^W + \frac{e_i^W - e_i^{WW}}{2} \tag{86}$$

For this, the directional energies of outer nodes W ad WW were required and were computed from initialized lattice temperatures assuming all the directional energies were equal (diffuse behavior) at these nodes. As explained in Chapter 3 iterative

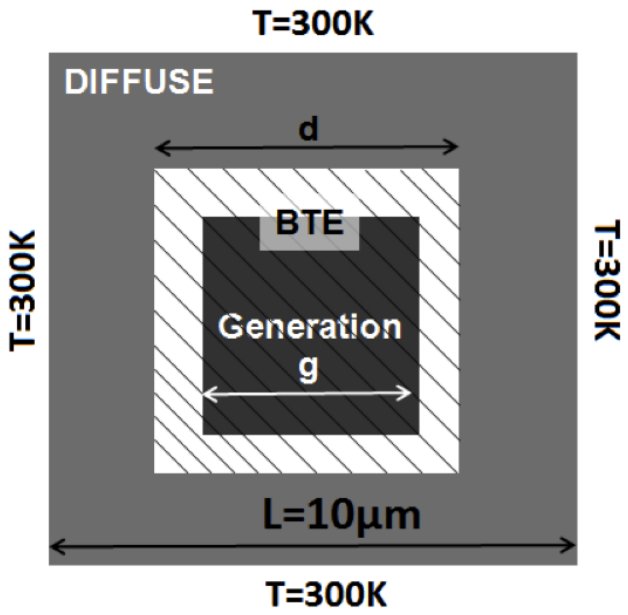

Figure 34: Investigated geometry 1. Fourier's diffusion equation was solved for the entire domain (represented as Diffuse domain) with size $L = 10\mu m = 100 \times \Lambda$ where heat generation region size was g and BTE solved for only the dashed region with size d represented as BTE domain(coupling region was included in BTE region).

solution using GMRES was performed to solve gray phonon BTE. Once the directional energies at BTE nodes were solved for one direction, they were immediately updated since they impact the solution of other directions via the relaxation matrix term. This was repeated until the convergence of all directional energies. Since the coupling is in one direction only, it is sufficient to solve for temperature in entire domain once using Fourier model and use the boundary conditions to solve for temperatures in BTE domain using the iterative technique explained above. Finally the directional energies at the BTE nodes were used to obtain nodal temperatures in BTE domain using Eq.25.

5.3 Investigated Problem

The multiscale model was first used to investigate the problem depicted in Fig.34. The reason for placing the localized heat generation region at the center of the domain

was to eliminate the boundary effects to come up with some generalized discussion. The domain was a square of side length L, with boundary temperature T, square heat generation region of side length g and a square BTE region of side length d that surrounds the heat generation region ($d > g$). The phonon group velocity used for simulations was $v_g = 1000m/s$ and the relaxation time was $\tau = 100ps$, giving a phonon mean free path of $\Lambda = v_g\tau = 100nm$. Bulk thermal conductivity of the material modeled was assumed to be $k = 254W/mK$ which provides properties related to high quality gallium nitride materials [9]. Finally, the specific heat was calculated from kinetic theory as in Eq.6.

The size of the domain was chosen as $L = 100\Lambda = 10\mu m$, to ensure phonons relax to their equilibrium energy at the boundaries. This way ballistic effects due to boundary scattering were eliminated entirely leaving the main reason of ballistic effects as localized heating. Constant temperature boundary condition ($T = 300K$) were applied at the outer boundaries as illustrated in Fig.34. The size of the heat generation region, g was chosen to cover the full range of ballistic-diffusive to diffusive localized heating. Thus the relative sizes of heat generation region, g to mean free path of phonons, Λ was chosen as $g/\Lambda = 1, 2, 5$, and 0.1. The total integrated heat generation rate in the domain was taken as $G = 50W/mm$. Therefore, the volumetric heat generation rate q''' for each case was different and calculated from the total heat generation rate, G and size of the heat generation region, g to ensure the total heat generation rate was constant.

Another goal was to understand the importance of the choice of the size of the BTE region on the accuracy of the results of the above explained multiscale method and the effects of the size of heat generation and phonon mean free path on this. Thus, d was increased from $d = g$ (for each heat generation domain size) to $d = 0.8L$ to understand the effect of the size of the BTE domain size on the accuracy of the results and to find the minimum size of the BTE domain that will maximize the

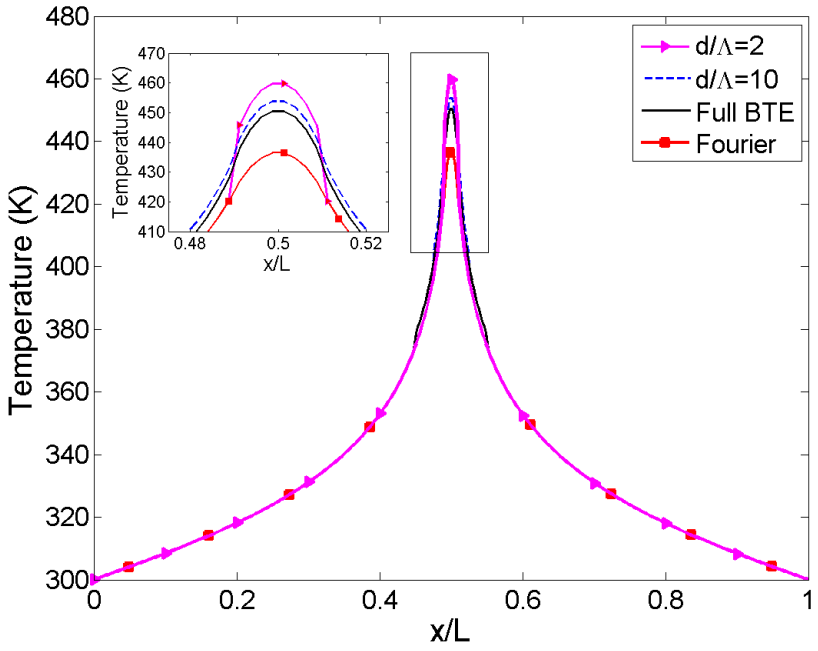

Figure 35: Midline temperature profile (at $y = L/2$) for the investigated geometry when heat generation region has size, $g = 200nm = 2 \times \Lambda$. Solutions were obtained using Fourier's diffusion equation (Fourier), phonon BTE solution in the entire domain (Full BTE), and multiscale model with varying d (size of the BTE domain) explained in this study. Inset shows the zoomed in view of the peak temperature.

speed of the solution without sacrificing the accuracy. To investigate the validity of the multiscale model FVDOM solutions for all cases were obtained for the entire domain and used as benchmark. Although such solutions take longer time than the multiscale approach they were required to test the validity and applicability of the multiscale method.

5.3.1 Results

The midline temperature profiles obtained using the multiscale solution for the cases $g/\Lambda = 2$ and $g/\Lambda = 10$ were shown in Fig.35 and Fig.36, respectively. These plots also include the temperature profiles obtained from the solution using the FVDOM method over the entire domain for comparison. Figure 35 includes the solution of

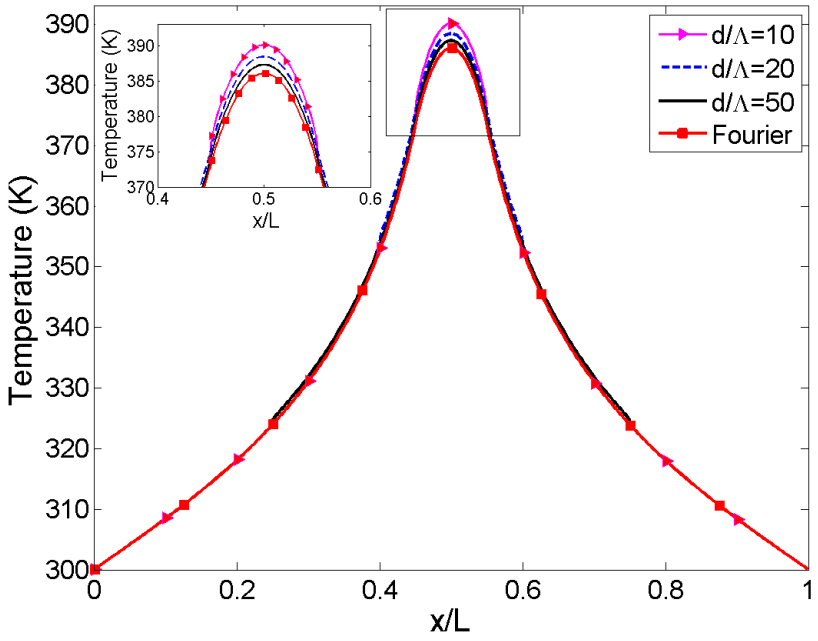

Figure 36: Midline temperature profile (at $y = L/2$) for the investigated geometry when heat generation region had size, $g = 1\mu m = 10 \times \Lambda$. Solutions were obtained using Fourier's diffusion equation(Fourier) and multiscale model with varying d (size of the BTE domain) explained in this study. Inset shows the zoomed in view of peak temperature.

Fourier's diffusion equation to show the ballistic heat transport effects. For the problem with $g/\Lambda = 2$, the size of the BTE region, d was increased from $d = g = 200nm$ to $8\mu m$. On the other hand, for the problem with $g/\Lambda = 10$, size of the BTE region, d was increased from $d = g = 1\mu m$ to μm.

From Fig.35 it is observed that the maximum temperatures calculated with the multiscale model were at least 10K higher than the maximum Fourier temperature. This is not observed in Fig.36, where maximum temperatures obtained using the multiscale model were only slightly different from Fourier since the heat generation region was larger and the ballistic effects were not as significant. This shows that when the phonon mean free path was $\Lambda = 100nm$ and $g = 1\mu m$ diffuse behavior was reached and the ballistic effects became almost negligible and temperatures relaxed to Fourier temperatures in the entire domain. When the mean free path of phonons

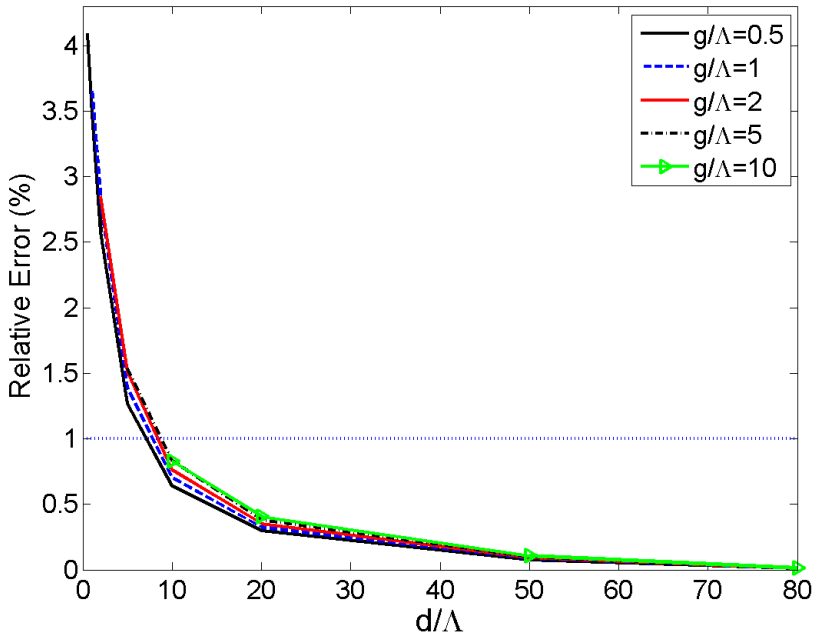

Figure 37: Relative error of maximum temperature obtained with multiscale model for investigated geometry shown in Fig.34 with respect to relative size of the BTE region to mean free path of phonons ($d/\Lambda = 10$). When $d/\Lambda = 10$ relative error is below %1.

was longer, this distance became longer. Thus the relative size of the generation region size with respect to phonon mean free path is important while determining the ballistic effects.

In Fig.35, for $d = 200nm$ and $g = 200nm$, an overshoot in temperature of 20K was observed. In addition, discontinuities at the boundaries where the BTE domain meets the Fourier domain can be seen. Once the BTE domain size was increased to $d = 1\mu m$, it was observed that the temperature rise has converged to 448K and the value of temperature at the boundaries has converged. Therefore, it can be concluded that when the BTE region was small, coupling with Fourier domain was done before carriers reach the equilibrium energy causing additional ballistic effects and higher temperatures. However, as the BTE domain was expanded, the coupling occurred further away from the hotspot and the carriers reached diffuse behavior decreasing the ballistic effects and discontinuities. This is important since it proves the redundancy

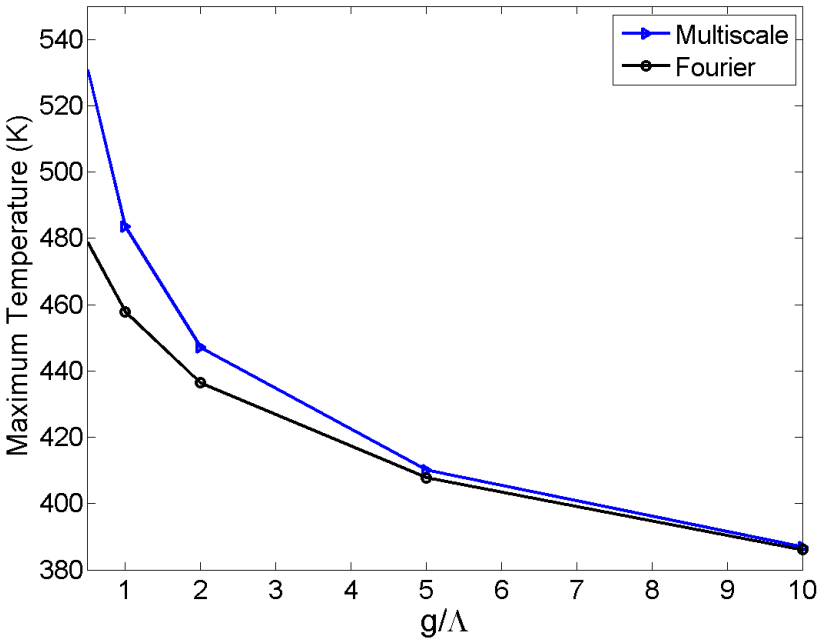

Figure 38: Converged maximum temperatures obtained with the multiscale model for the investigated geometry shown in Fig.34 with respect to the relative size of the heat generation region to mean free path of phonons (g/Λ).

of solution of BTE away from hotspot in big domains which can be accounted for more easily using simple continuum heat transport simulations. The temperatures in Fig.36 are very close to the full FVDOM solution and Fourier temperature since the ballistic effects were not as significant due to a relatively large heat generation region. As a result of this, the discontinuities were not as significant as in Fig.35. After observing the effect of the size of the BTE region on the discontinuities and the maximum temperature convergence it is important to define a minimum BTE domain size that will give accurate results when multiscale model is used.

Figure 37 is the relative percentage error plot of maximum temperatures obtained using multiscale model using different BTE domain sizes. The relative percentage error was calculated taking the maximum temperatures obtained from the FVDOM solutions in the entire domain as reference. Figure 37 shows the decreasing trend and convergence of relative percentage error as the size of the BTE domain, d increase.

When the heat generation region had the size of $g = 50nm$ and the size of the BTE region was $d = 50nm$, the relative percentage error became as high as 4%. Considering the magnitude of maximum temperature, which was more than 500K, 4% error corresponds to a 20K temperature over prediction. However, the relative percentage error dropped below 1% for all cases, independent from heat generation region size when BTE region was chosen as $d = 10\Lambda = 1\mu m$. This is a significant result since it tells us distance required for diffuse behavior to be reached independent from the size of the heat generation which is 10 times the mean free path of phonons. Moreover, this result shows that if no real boundaries exist within 10Λ distance of the heat generation region then it is sufficient to model only the 10Λ vicinity of the area with ballistic effects with FVDOM and the rest with diffuse models. This ratio is further validated with simulations performed by keeping the material thermal conductivity same but changing the phonon mean free path to 300nm. Therefore, it can be concluded that diffuse behavior is reached in a distance about 10 times that of mean free path.

Finally, Fig.38 is the plot of the converged maximum temperature of the domain with respect to the heat generation region size, g, obtained using the multiscale model versus a Fourier solution. Figure 38 illustrates the ballistic nature of heat transport caused by the submicron heat generation region. When the heat generation was submicron in size, heat was not carried away from the hotspot fast enough, resulting in higher maximum temperatures compared to the Fourier solution as can be seen in Fig.38. The slow heat removal from the hotspot area was due to continuous addition of energy to the lattice while constraining the phonon relaxation mechanisms with very short length scales. When the size increased, the temperature decreased due to the decrease in ballistic effects and the thermal resistance. Since the ballistic effects no longer existed as the size of the generation region increased to the micron scale, the Fourier and multiscale solutions of temperature became almost identical.

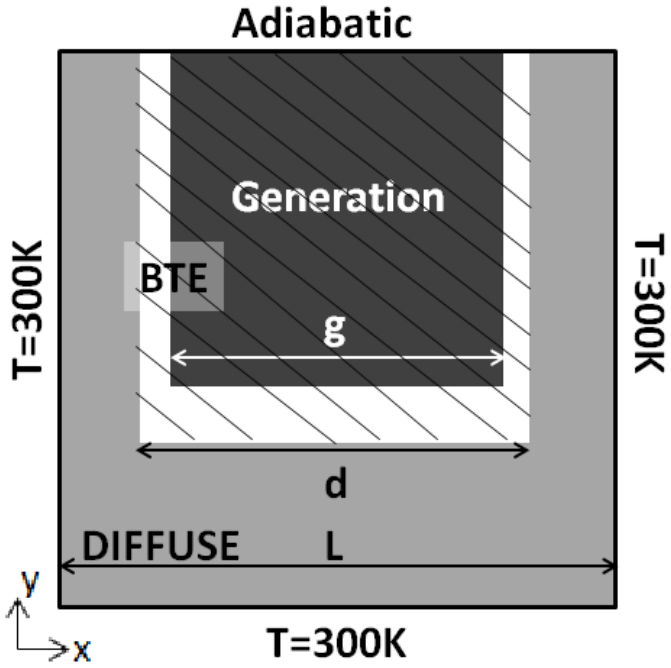

Figure 39: Investigated geometry 2. Fourier's diffusion equation was solved for the entire domain (represented as Diffuse domain) with size $L = 10\mu m$ where heat generation region size was g and BTE solved for only the dashed region with size d represented as BTE domain(coupling region was included in BTE domain).

In order to investigate the influence of the size of the domain, L, and the magnitude of the total heat generation, G, on the results additional simulations were performed. Although, the magnitude of the temperatures were changed due to the change of size of the domain and total heat generation, similar trends were observed for the convergence of results with respect to size of the BTE domain. Therefore, it can be concluded that independent from the size of the entire domain, magnitude of the total heat generation rate, G, or the size of the heat generation region, g, the BTE domain can be taken as small as 10 times the mean free path of phonons for accurate modeling of hotspot temperature of a similar problem.

5.4 Heat Generation Close to a Boundary

The first problem investigated in Fig.34, had localized heating at the center of the domain. However, for some applications such as field effect transistors in semiconductors, heat generation can occur near one of the surfaces or domain boundaries. These boundaries might have extra effects on the ballistic nature of heat transport. The multiscale modeling parameters that were found for the earlier investigated case might not hold for such problems. For example, when boundaries were present in the vicinity the previous conclusion about diffuse behavior being reached in a distance about 10 times that of mean free path was no longer correct. Therefore, to understand the effects on the domain boundary on the ballistic to diffusive transport transition we also investigate the domain presented in Fig.39 where the heat source is located next to the domain boundary.

For this second problem, the size of the domain was chosen as $L = 100\Lambda = 10\mu m$ to eliminate the additional ballistic effects that might be caused by the boundary scattering effects. Similar to problem illustrated in Fig.34 generation region, BTE domain, and the full domain were all chosen as squares. Constant temperature boundary condition (T=300K) was applied at the three outer boundaries and adiabatic boundary condition was applied to the remaining boundary as illustrated in Fig.39. Same material properties were used for these simulations.

5.4.1 Results

The surface temperature profile obtained for the geometry shown in Fig.39 is given in Fig.40. From Fig.40 it is observed that once the BTE domain size was increased from $d = 1\mu m$ to $d = 8\mu m$, the maximum temperature increased and finally converged to the full BTE solution of the problem. Increase of temperature with the increased size of the BTE domain was different from what has been observed with the previous problem investigated where the temperature decreased with the size of the BTE

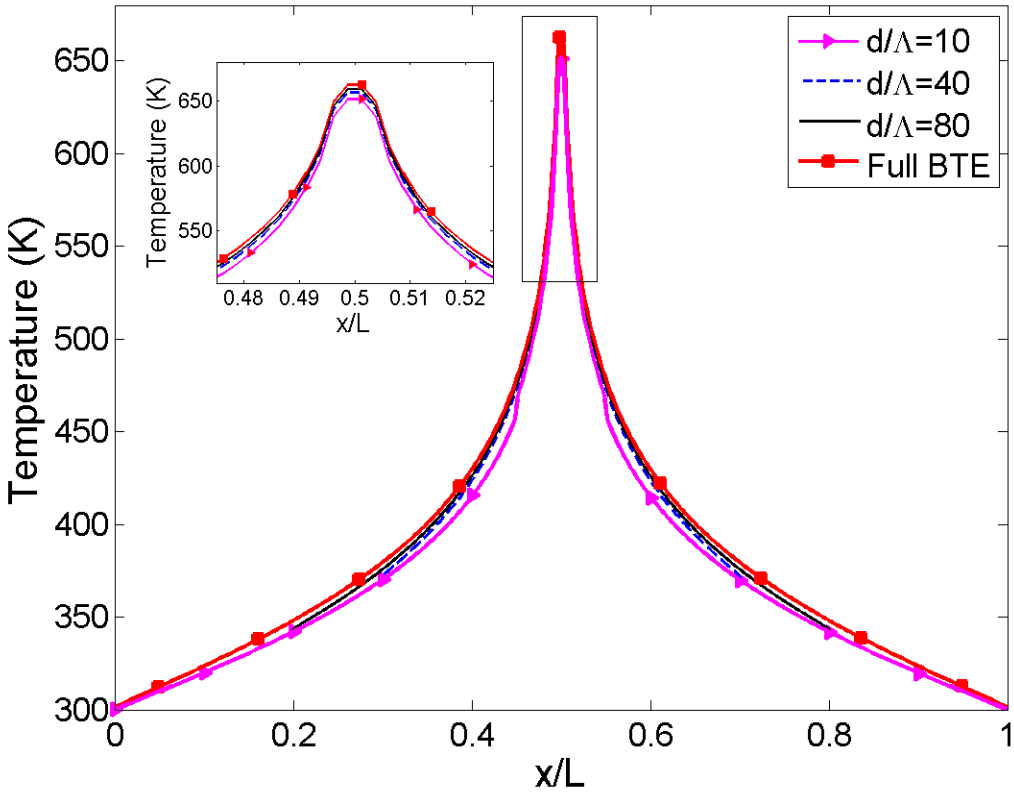

Figure 40: Surface temperature profile (at $y = L$) for the investigated geometry when heat generation region has size, $g = 100nm = \Lambda$. Solutions were obtained using phonon BTE solution in the entire domain (Full BTE), and multiscale model with varying d (size of the BTE domain) explained in this study. Inset shows the zoomed in view of the peak temperature.

region. This is due to additional boundary scattering effects. When the size of the BTE region is small some of these ballistic phonon effects that were reflected from the boundary were lost thus reducing the temperatures of the domain.

Figure 41 is the relative absolute percentage error plot of maximum temperatures obtained using multiscale model using different BTE domain sizes. Similar to the first problem, the relative percentage error was calculated taking the maximum temperatures obtained from the FVDOM solutions in the entire domain as reference. Figure 41 shows the decreasing trend and convergence of relative percentage error as the size of the BTE domain, d increase. However, unlike the previous case when the size of

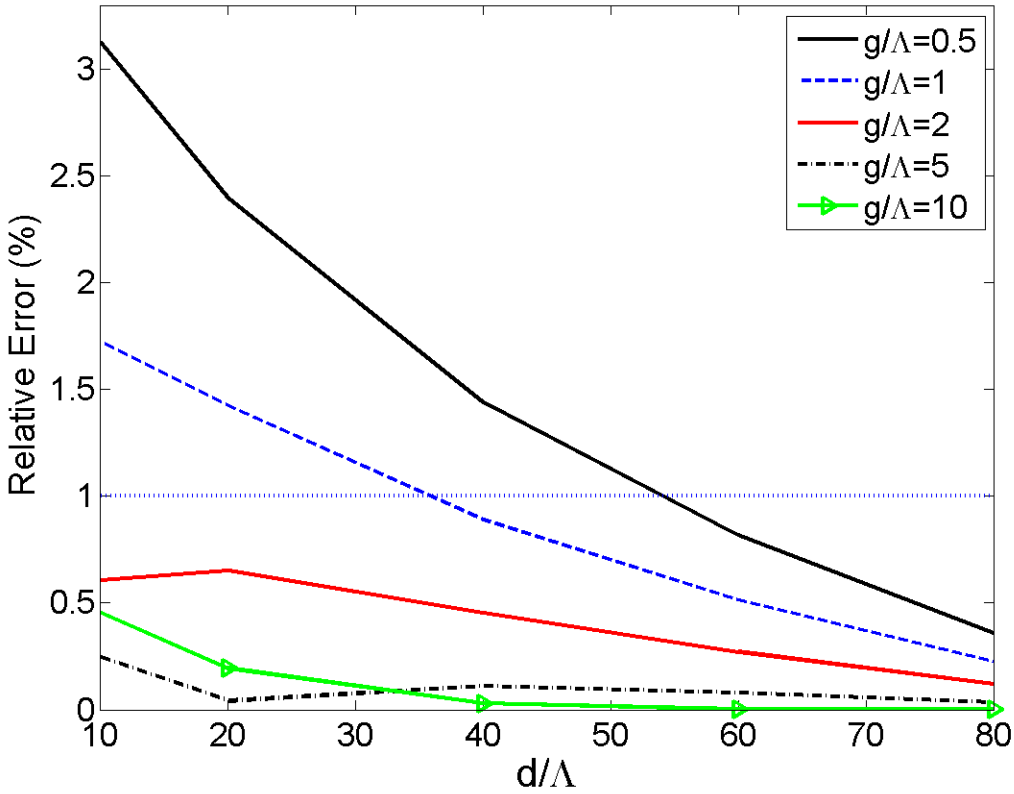

Figure 41: Relative error of maximum temperature obtained with multiscale model for investigated geometry shown in Fig.39 with respect to relative size of the BTE region to mean free path of phonons (d/Λ). When $d/\Lambda = 10$ relative error is below %1.

the BTE region was about 10 times the mean free path the relative error was higher than 1% for some cases.

When the heat generation region had the size of g=50nm and the size of the BTE region was $d = 1\mu m$, the relative percentage error was found to be more than 3%. Considering the magnitude of maximum temperature for this case which was more than 700K, 3% error corresponds to about 30K temperature under prediction. However, the relative percentage error drops below 1% for all cases, independent from heat generation region size when BTE region was chosen bigger than $5\mu m$. This shows that when boundary effects are present and the heat generation is extremely small BTE region should be chosen bigger.

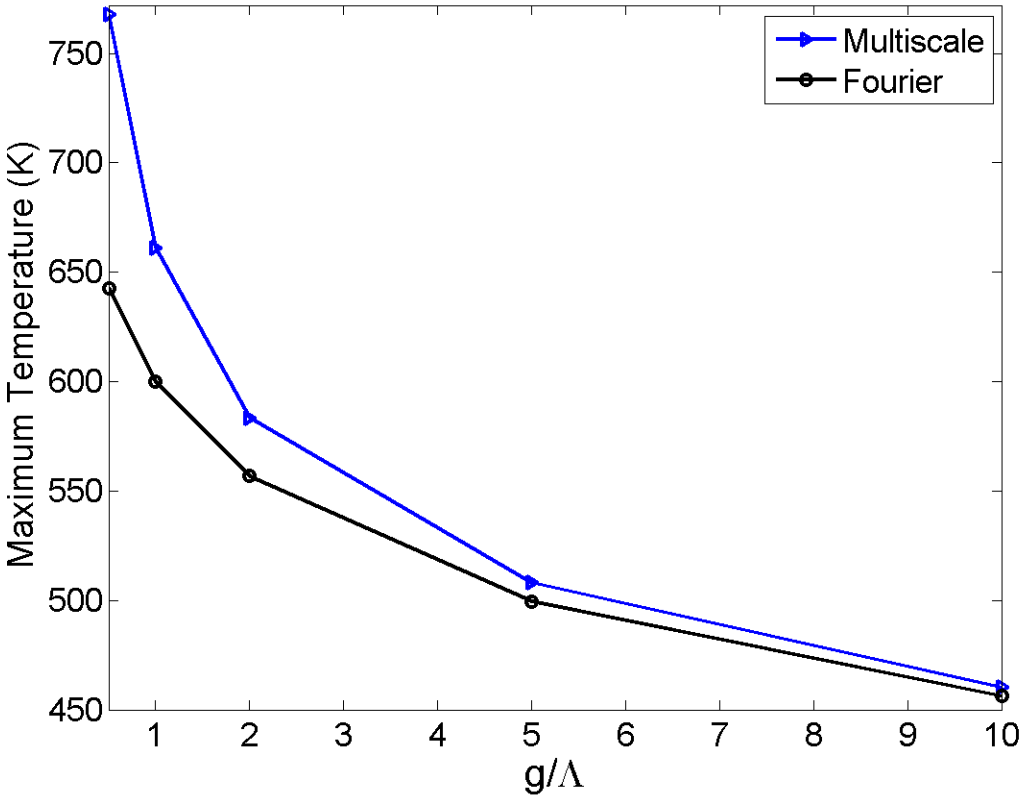

Figure 42: Converged maximum temperatures obtained with the multiscale model for the investigated geometry shown in Fig.39 with respect to the relative size of the heat generation region to mean free path of phonons (g/Λ).

Finally, Fig.42 is the plot of converged maximum temperature of the domain with respect to the heat generation region size; g obtained using the multiscale model versus a Fourier solution. The submicron heat generation region that was responsible for ballistic phonon transport effects was the main cause of the maximum temperature difference between the Fourier and multiscale model temperatures. As the size of the generation domain was increased these temperatures converge. However, the convergence is much slower in Fig.41 compared to Fig.37 as a result of additional scattering effects from the boundary in the vicinity.

5.5 Coupling of BTE and COMSOL

Finally, since the coupling procedure utilized here was a one way coupling procedure a commercially available software (i.e. COMSOL) can be used for modeling the heat transport in the diffuse domains of the multiscale model. Using a commercially available software for the diffuse domain has several advantages like unstructured mesh generation for computational efficiency and modeling more complex, bigger geometries as well as modeling different physical processes such as fluid dynamics that can be used for different applications such as for investigating the effect of cooling liquids on the temperature of a submicron hotspot. Once the temperatures were obtained for the diffuse domain a similar coupling technique can be used to provide boundary conditions for the BTE domain where ballistic effects were present.

5.6 Conclusion

A multiscale phonon BTE and Fourier's heat diffusion equation solver was suggested for the investigation of heat transport at localized heat generation regions away from the boundary scattering effects. The multiscale method was validated by comparing with results obtained by the solution of Fourier's diffusion equation in diffuse limit and a full domain phonon BTE solver in the ballistic limit. It was found that the physical dimensions, the size of the heat generation region, mean free path of carriers are important parameters affecting the nature of heat transport in the domain.

When the boundaries were far removed from the localized heat generation region it was shown that the multiscale model can be used when the BTE region is at least 10 times the mean free path of phonons. When this was the case, the multiscale model gave identical results to full FVDOM solutions. However, the multiscale model cannot be used for small domains (i.e. smaller than 10Λ) where the boundaries are not far removed from the heating region, thus a full BTE solution should be employed. When non-gray models are used one should consider accounting for the longest mean

free path of the phonons used to model the structure. On the other hand, when the heat generation region causing the ballistic effects is close to a physical boundary, which is the case in most transistors, the required size of the BTE domain must be larger. This is a result of the reflecting surface that slows the phonon relaxation and heat transport from the hotspot [9] causing the ballistic effects to dominate over a larger region. Therefore, special care must be given in determining the proper BTE domain size when non-gray models are used and the localized heat generation is close to domain boundaries.

Finally, since the coupling procedure utilized here was a one way coupling procedure, any commercially available software utilizing finite element or finite difference temperature solutions can be used for modeling the heat transport in the diffuse domains of the multiscale model. Using a commercially available software for the diffuse domain has several advantages like unstructured mesh generation for computational efficiency and modeling more complex, larger geometries as well as modeling different physical processes such as fluid dynamics that can be used for different applications such as for investigating the effect of cooling liquids on the temperature of a submicron hotspot.

CHAPTER VI

DEVICE SIMULATIONS

In this chapter electrical and multiscale thermal simulations are performed for HFETs using gray and non-gray approaches to estimate the hotspot temperature under various bias conditions. This was performed using a one-way coupling between electrical simulations and multiscale thermal simulations.

6.1 Simulation Procedure

General simulation procedure used for device simulations is given in Fig.43. First, two-dimensional electrical simulations were performed at the active region of an operating device to obtain Joule heating data. Later this data was projected in 3rd dimension an used for three-dimensional Comsol thermal simulations that include the realistic boundary conditions, substrate, and other surrounding materials.

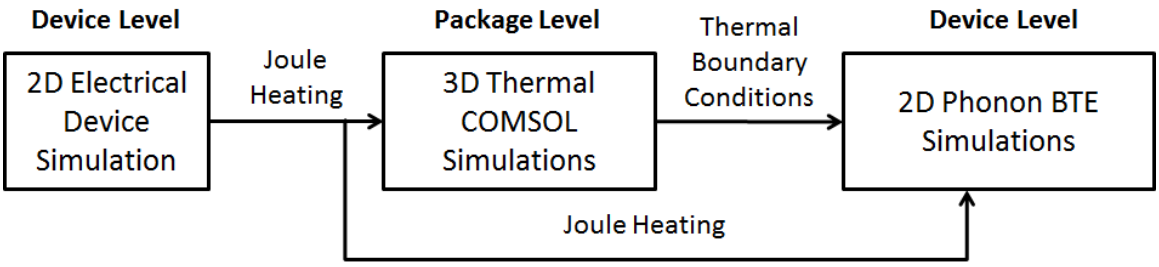

Figure 43: Flow chart explaining the steps of the gray and non-gray multiscale electro-thermal simulations.

Finally, in order to account for ballistic effects at hotspot area, two-dimensional phonon BTE simulations were performed at a small region enclosing the hotspot. Thermal boundary conditions were taken from the Comsol solutions and the Joule

heating data was obtained from the electrical simulations. The device simulations performed in this chapter are categorized as gray and non-gray.

For the gray simulations, the hydrodynamic electrical simulations were performed to obtain Joule heating data of these devices is described, followed by the multi-scale thermal model. The Joule heating distribution from the electrical simulations for various bias conditions was fed into the multiscale thermal model using a gray assumption to determine the maximum temperature and its distribution for a multifinger HFET. The results were obtained for devices operating at different biasing conditions and compared.

For the non-gray simulations, the realistic electron to lattice energy relaxation information was obtained from Monte Carlo simulations. Monte Carlo simulations were used as they have the ability to determine which phonon bands the energy is being transfered to versus hydrodynamic calculations. The temperatures obtained using non-gray models with increasing complexity were compared with each other and the effect of biasing conditions were discussed.

6.2 Device Description

In this chapter, two-finger HFET devices were investigated. The representation of the die with a 2 finger HFET is shown in Fig.44. In Fig.44 there are two gates, the width of the gate is represented with Wg. The gate, source, and drain lengths are marked with Lg, Ls, and Ld. The spacings between the gate and the source and the gate and the drain are marked with Lgs and Lgd respectively.

For both the gray and the non-gray simulations device gate width (Wg) was chosen as $100\mu m$, and a $200\mu m$ thick SiC was chosen as substrate. Other device dimensions used in gray and non-gray simulations are given in subsequent sections.

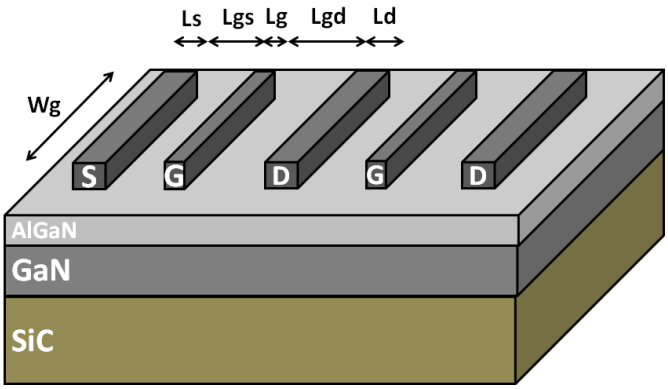

Figure 44: The schematic of the 2 finger AlGaN/GaN HFET die.

6.3 Gray Simulations

6.3.1 Electrical Simulations

The hydrodynamic electrical simulations were performed in a 2D. The schematic of the cross section of one finger (due to symmetry) which was modeled electrically is shown in Fig.45. The SiC substrate is omitted in electrical simulations since it is known to play a negligible role in determining dc characteristics of such devices[1]. The device modeled was composed of a $3\mu m$ GaN layer and a 30nm AlGaN layer grown on SiC substrate. The devices were passivated with 10nm SiO_2 layer, which has been shown to be a good alternative to more common Si_3N_4 passivation[107]. Gate length (Lg), gate-source (Lgs), and gate-drain (Lgd) spacings were $0.7\mu m$, $1\mu m$, and $2\mu m$ respectively.

Two investigate the effects of power on hotspot temperature electrical simulations were performed for devices operating at power densities between 2 and 8 W/mm at VGS=-0.5V. These power densities were the average power output of the device per millimeter of gate width(Wg).

In order to account for change of mobility at high electric fields, hydrodynamic Canali model explained in [65] is utilized. In the hydrodynamic Canali model used for this study temperature dependence of mobility under low electric fields was taken into account. High electric field was determined based on the electron saturation velocity

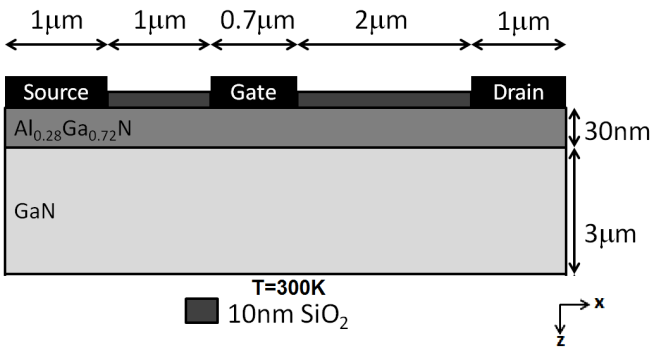

Figure 45: The schematic of the AlGaN/GaN HFET simulated using multiscale gray thermal simulations.

Table 5: Electrical Material Properties used in Sentaurus Simulations[1].

Parameters	GaN	AlGaN
Dielectric Constant	9.5	8.5
Energy Gap (eV)	3.47	6.2
Electron Affinity (eV)	3.4	1.7
Effective Conduction Band Density of States (cm^{-3})	2.65×10^{18}	4.1×10^{18}

and the mobility was calculated accounting for the low field mobility, saturation velocity, and the driving force due to electric field. The electron saturation velocity of GaN was taken as $1.3x10^7 cm/s$.

The quantum effects caused by the extreme localization of electrons in 2DEG region were included using the density gradient(DG) transport model [65]. The approximate values of the trap density and cross section were still being investigated [1]. Therefore, the density and cross section of GaN layer traps, placed 1eV above the mid band gap, were assumed to be $N_{trap} = 3 \times 10^{18} cm^{-3}$ and $\sigma_{trap} = 1 \times 10^{-15} cm^{-2}$. Metal/Schottky barrier height of gate was taken as B=1.48V[108].

Using the spontaneous and piezoelectric polarization, sheet carrier density AlGaN/GaN interface was calculated as $1.56 \times 10^{13} cm^{-2}$ using the relation[3]:

$$\sigma(x) = P_{PE}(Al_xGa_{1-x}N) + P_{SP}(Al_xGa_{1-x}N) - P_{SP}(GaN) \tag{87}$$

where x is the Al mole fraction, $P_{SP}(GaN)$ is the spontaneous polarization of GaN

taken as $-0.029C/m^2$, $P_{SP}(Al_xGa_{1-x}N) = (-0.052x - 0.029)C/m^2$ is the spontaneous polarization of AlGaN layer, and $P_{PE}(Al_xGa_{1-x}N)$ is the piezoelectric polarization of $Al_xGa_{1-x}N$ that can be computed using [3]:

$$P_{PE}(Al_xGa_{1-x}N) = 2\frac{a(0) - a(x)}{a(x)}\left(e_{31}(x) - e_{33}(x)\frac{C_{13}(x)}{C_{33}(x)}\right) \tag{88}$$

where a's are lattice constant, C_{13} and C_{33} are elastic constants, and e_{31} and e_{33} are piezoelectric constant that can be found in [3].

The electrical properties of GaN and AlN used for the electrical device simulations are presented in Table 5. Properties of $Al_xGa_{1-x}N$ alloy are calculated from the AlN and GaN properties using the equation below [65]:

$$P(Al_xGa_{1-x}N) = xP(AlN) + (1-x)P(GaN) \tag{89}$$

The boundary conditions applied for the solution of lattice energy conservation equation given in Eq.12(c) were all adiabatic except for the bottom boundary where the temperature is specified as T=300K. The IV response of the device shown in Fig.45 obtained under different biasing conditions at the end of two-dimensional electrical simulations is shown in Fig.46.

Using Fig.46 the drain source voltage required for the device to operate at power densities of 2, 3, 4, 5, 6, 7, and 8 W/mm were obtained. Device simulations at these power levels were performed one more time to obtain the Joule heating distribution. In order to illustrate the extreme localization of heat under the gate edge Joule heating distribution for the device operating at 2W/mm and 8W/mm are shown in Fig.47. Localization was observed under the gate edge on the drain side due to pinching of the gate at VGS=-0.5V. The distribution of Joule heating seems more localized for the device operating at 2W/mm. On the other hand, magnitude of localized heating is much higher when the device operates at 8W/mm. This heat distribution was later used in detailed thermal simulations as described in Fig.43.

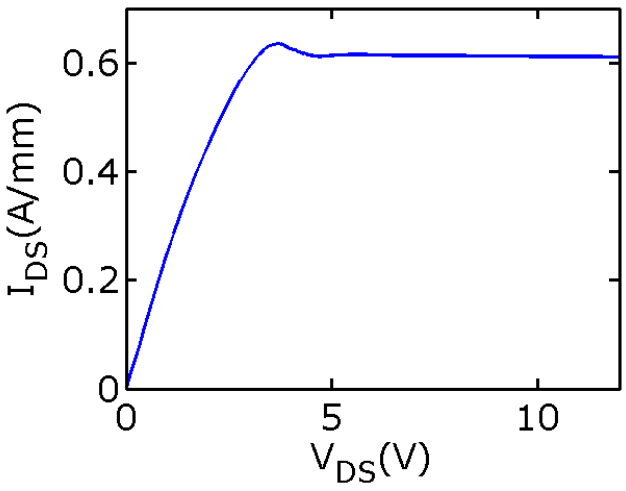

Figure 46: IV curve obtained by the 2 dimensional Sentaurus electrical simulations of the device shown in Fig.45 (Since electrical simulations were performed in 2D, current is given as current per unit gate width, Wg).

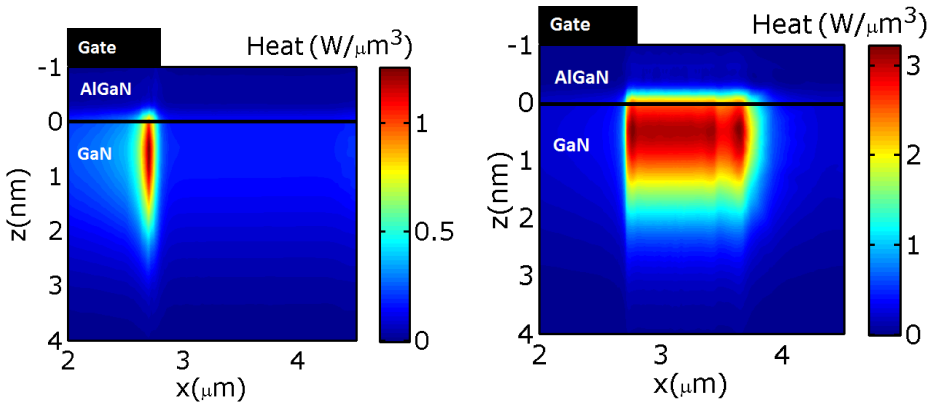

Figure 47: Joule heating distribution of the device operating at a power density of (a)2W/mm (b)8W/mm.

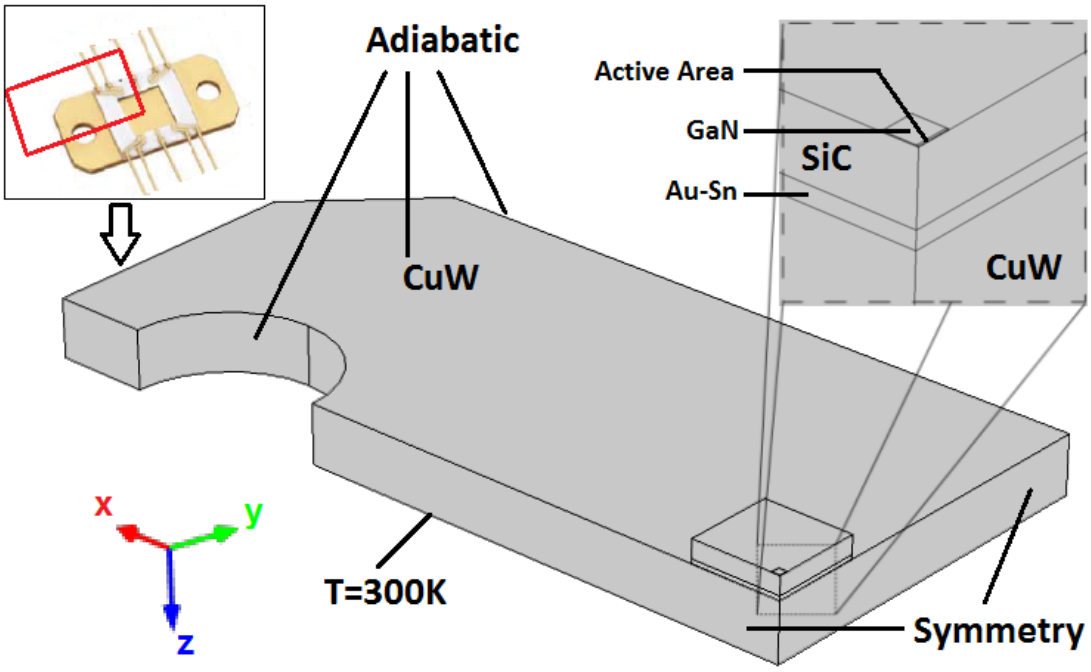

Figure 48: The schematic of the 3D COMSOL thermal model to represent the CuW package from StratEdge Corp.(shown as inset) and the die with boundary conditions. Zoomed in view shows the die and the active area.

6.3.2 COMSOL Simulations

In order to obtain better temperature estimates detailed thermal simulations including the package, substrate, and realistic boundary conditions is necessary. Due to computational restrictions, it is not feasible to perform such simulations using Sentaurus device simulator. As a result, we performed detailed thermal simulations separately using COMSOL Multiphysics. This thermal model includes not only the die but also the package on which these devices are generally mounted on.

Devices grown on SiC substrates are investigated and the thermal interface material used for bonding the die on the package is chosen as gold-tin alloy (Au-Sn). The inset of Fig. 48 shows the schematic of the RF package made of Copper-Tungsten (CuW) alloy used in these simulations.

Due to the symmetry of the device and the package, only the quarter of the package and the die is modeled. This is shown in Fig. 48. The temperature dependent

Table 6: Thermal conductivities of materials used for the simulations.

Material	$k(W/mK)$
Gallium Nitride	150
Silicon Carbide [109]	$387 * (T/293)^{-1.49}$
Copper Tungsten [110]	$204 - 2.51x10^{-2}T - 7.62x10^{-5}T^2$
Bonding (Au/Sn) [111]	57

thermal conductivities used for thermal simulations are given in Table 6. Thermal conductivity of GaN, $150W/mK$[15], is used due to ballistic-diffusive simulations that can only be performed with constant thermal conductivity at this stage. The thermal boundary resistance of $3.3 \times 10^{-8}m^2K/W$ is applied at the SiC and GaN interface [112].

Since two-dimensional Joule heating distribution obtained from Sentaurus simulations was extremely localized as shown in Fig.47, the mesh used in the COMSOL simulations should be extremely fine. However, due to computational restrictions and the geometry of the device, using elements with side lengths less than 100nm was not feasible for this study. Therefore, two-dimensional Joule heating data was first projected by integration to a line with 100nm grid spacing. Later this data was imported to COMSOL and a new function was defined to project it $100\mu m$ along +y direction to represent the gate width in three-dimensional simulations. This way the two-dimensional volumetric heat generation data from Sentaurus was transformed into a 3-dimensional surface heat flux data to be used in COMSOL simulations. All other surfaces except the bottom surface of CuW package were treated as adiabatic surfaces. Temperature of the bottom surface was kept at T=300K.

Finally, to match this projected heat flux surface meshing of GaN in Fig.48 was done in four steps. First step was meshing the edge with 100nm elements along x direction. The second step used these edge elements to build triangular surface elements on the symmetry surface of GaN layer. Later, this mesh was projected along the gate width direction using the sweeping function of COMSOL. Finally,

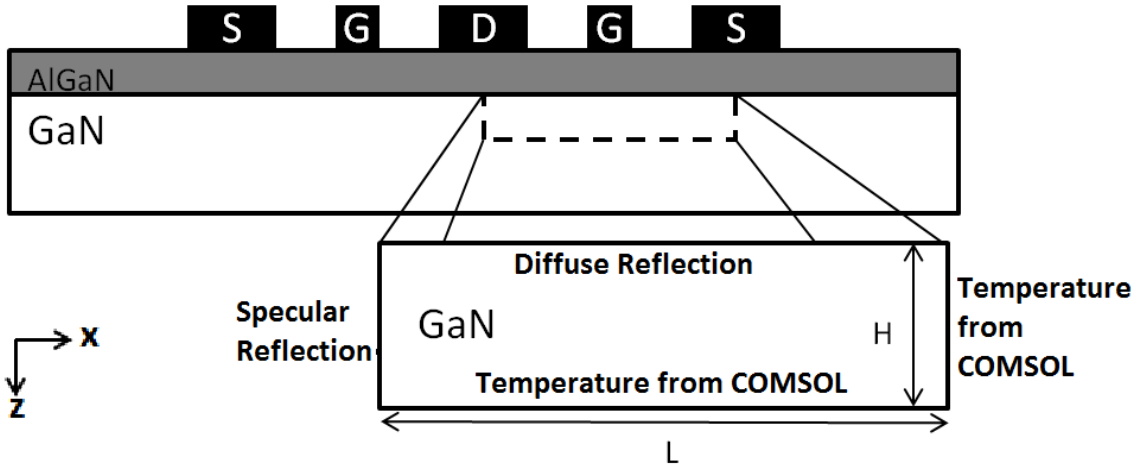

Figure 49: Zoomed in view of the thermal domain modeled to observe the ballistic diffusive thermal transport effects due to localized Joule heating with boundary conditions.

remaining sections of the domain were meshed using tetrahedral elements.

After meshing, COMSOL simulations were performed and the temperature distributions were obtained. As a final step, the ballistic diffusive effects at the hotspot were investigated using the Joule heating data from Sentaurus and temperature data from COMSOL simulations.

6.3.2.1 Ballistic-Diffusive Thermal Simulations

Ballistic-diffusive effects at the hotspot were investigated by solving the two-dimensional phonon BTE using finite volume discrete ordinates method in a small domain. Modeling the hotspot using two-dimensional simulations is a good approximation since the gate width is generally very long compared to the size of the domain modeled using phonon BTE.

The domain that was modeled using phonon BTE had the size LxH ($10\mu m \times 3\mu m$) as shown in Fig.49. The reason to have such dimensions was to eliminate the boundary scattering effects from the application of boundary conditions. The extremely thin AlGaN layer was ignored in thermal simulations and thermal conductivity of the domain was taken as GaN thermal conductivity, k=150W/mK.

Joule heating was applied as a volumetric heat generation term to the GaN layer as represented in Fig.43. Since some of the heat generation data was in AlGaN layer as can be observed in Fig.47 this data was slightly shifted in order not to lose any of the heat generation in the device. Temperatures obtained from COMSOL simulations were applied to right and bottom boundaries as shown in Fig.49. Top boundary was assumed to be adiabatic since it is known that majority of the heat is carried away from the hotspot through the substrate and diffuse reflection boundary condition was applied to it. Finally, the left boundary was assumed to be a symmetry boundary thus a specular reflection boundary condition was applied to it.

The numerical solution of Eq.72 was performed using control volume discretization and Linear Upwinding Scheme (LUS) for spatial discretization. For angular discretization S6 quadratures were used since no direction of propagation is favored and strict symmetry conditions are satisfied by Sn quadratures[13].

The specific heat of GaN was taken as $C = 2.57 \times 10^6 J/m^3K$ as found in Chapter 4. Relaxation time and group velocity were calculated using two constraints: the mean free path and the thermal conductivity. First, the group velocity, specific heat, and relaxation time used in the solution of Eq.72 when used with Eq.6 should match the bulk thermal conductivity which is $k = 150W/mK$. The second constraint came from the mean free path of phonons.

Some of the previous research stated that phonons with mean free paths greater than 500nm are responsible for more than 50% of the thermal conduction in GaN lattice[9]. Since this is still being investigated we investigated the effects of different mean free paths on our ballistic diffusive simulations. Three mean free paths 100nm, 500nm, $1\mu m$ were used in simulations. Mean free path, Λ, was calculated from the multiplication of the group velocity and relaxation time.

For each mean free path, the relaxation time and the group velocity that satisfies the thermal conductivity and mean free path constraints were calculated. The hotspot

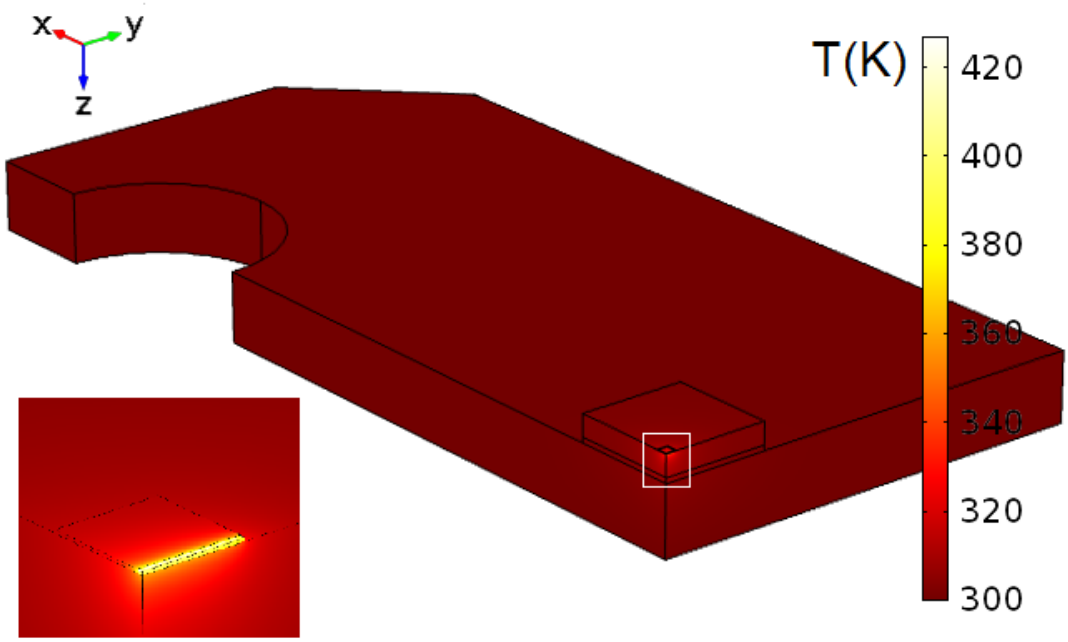

Figure 50: Surface temperature profile obtained by COMSOL simulations for the device operating at P=0.8W.

temperatures obtained at different stages of the thermal simulations are presented in next section.

6.3.3 Results

Surface temperature distribution for the device operating at 8W/mm obtained from COMSOL simulations is shown in Fig.50. Inset of Fig.50 shows the zoomed in view of the die where highest temperature more than 420K are observed. Although the highest temperatures were observed at the GaN layer, top layers of SiC substrate was also affected by the device operation. Therefore, thermal conductivity of the substrate is expected to play a significant role in thermal performance of devices. Moving away from the substrate towards the package the temperature variations diminished and almost the entire package was observed to be at a constant temperature which is equal to the base temperature of the package.

Temperature profiles along +y direction on the GaN surface under the gate edge

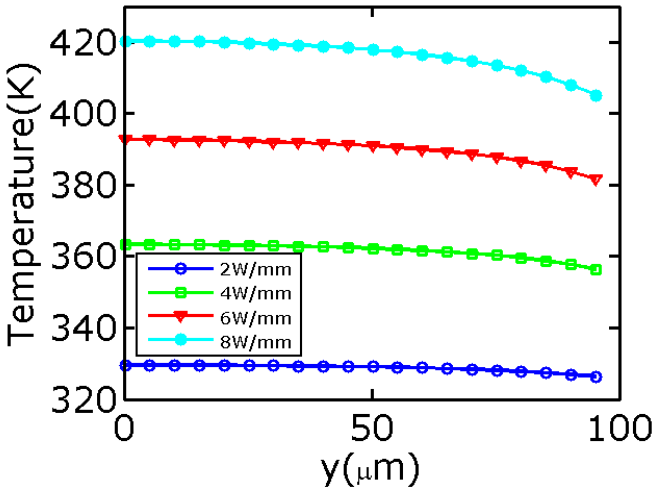

Figure 51: Temperature profile along the gate width (+y dir.) at gate edge on GaN surface at power densities of 2, 4, 6, and 8 W/mm.

were plotted for devices operating at 2, 4, 6, and 8 W/mm in Fig.51. For all cases the maximum temperatures were observed at y=0 on the symmetry plane. The highest temperature observed was T=420K at 8W/mm. The temperatures decreased along the gate width due to decreasing thermal resistance moving away from the center of the die. In Fig.51 the temperature difference between the center and edge of a finger was about 15K for a device operating at 8W/mm whereas it was much smaller for smaller power densities.

It is known that the temperature has an important negative effect on electrical performance variation of temperature. Thus, the variation of electrical performance along the gate width is not desired for uniform and high electrical performance of devices and should be accounted during device. This shows the importance of thermal models especially at high power densities.

Temperature variation along the channel is equally important and was plotted in Fig.52. Maximum temperatures were observed at the gate edge due to high electrical field gradients at this location. As a result of this, the temperature along the channel varied. As the power density of the device increased the variation of the temperature

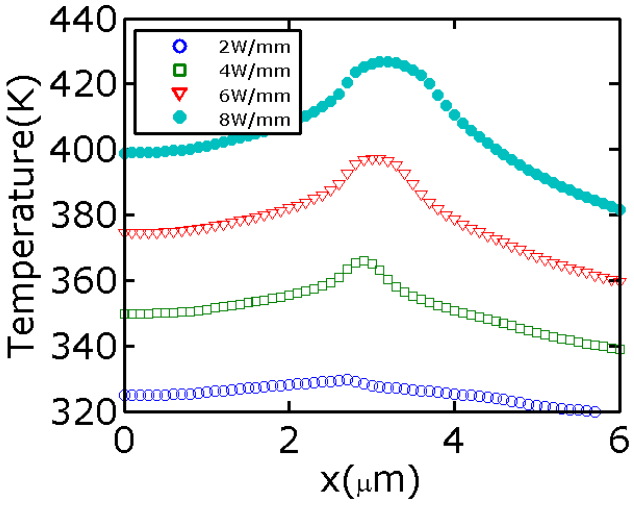

Figure 52: Temperature profile along the channel (+x) on GaN surface at power densities of 2, 4, 6, and 8 W/mm.

along the channel also increased. Moreover, when the ballistic-diffusive effects were also introduced, the temperature became 25K higher at the hotspot area which can be observed by comparing the GaN surface temperature profile obtained by COMSOL and ballistic-diffusive phonon models in Fig.53.

Figure 53 is the GaN surface temperature profile along the channel for a device operating at 3W/mm. Surface temperature profiles obtained by COMSOL and DOM with a phonon mean free path of 500nm were plotted for comparison. There was a significant difference of 25K between COMSOL and DOM at the hotspot as a result of the ballistic heat transport effects. Moving to the right away from the hotspot resulted in the temperature difference becoming negligible as the ballistic-diffuse effects disappeared. The maximum temperature difference between COMSOL and DOM was 25K for this case and this difference increased up to 60K when a longer phonon mean free path was used.

The maximum temperatures obtained using COMSOL and DOM for devices operating at different power densities from 2 to 8W/mm are plotted in Fig.54. Three different DOM plots represent the simulations performed at each power density using

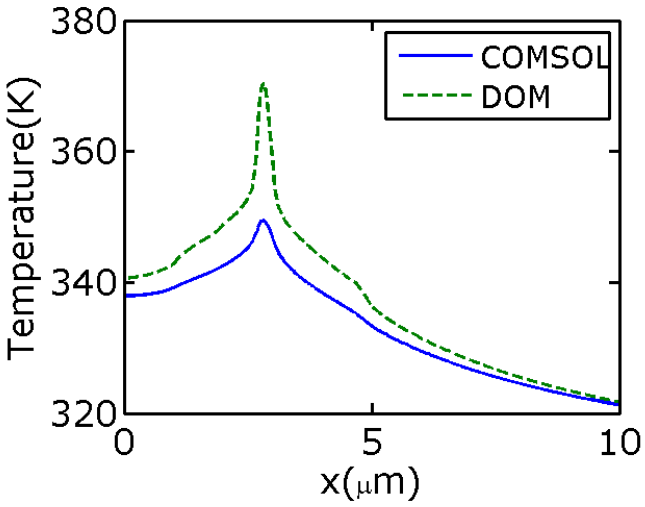

Figure 53: GaN surface temperature profile along the channel for device operating at 3W/mm when $\Lambda = 500nm$.

phonon mean free paths of 50nm, 100nm, and $1\mu m$. The maximum temperatures obtained using DOM were always higher than the maximum temperatures obtained using COMSOL due to the ballistic effects. The ballistic effects became more significant as the phonon mean free path increased. As a result of this the difference between COMSOL and DOM, the maximum temperatures increased from 25K to 60K. This was observed by comparing the three different maximum temperature lines of DOM for DOM cases as shown in Fig.54.

Finally, Fig.54 shows the increasing trend of the difference between DOM and COMSOL temperatures with the power density. This can be due to two main factors:

- The increasing magnitude of heat generation.
- The changing distribution of Joule heating.

Increasing the magnitude of power density causes the ballistic effects of phonons to last longer since it will take longer for them to relax to equilibrium. When a device is operated at higher powers at a given gate voltage distribution of heat is known to be more localized. Change in the distribution of Joule heating is a result of

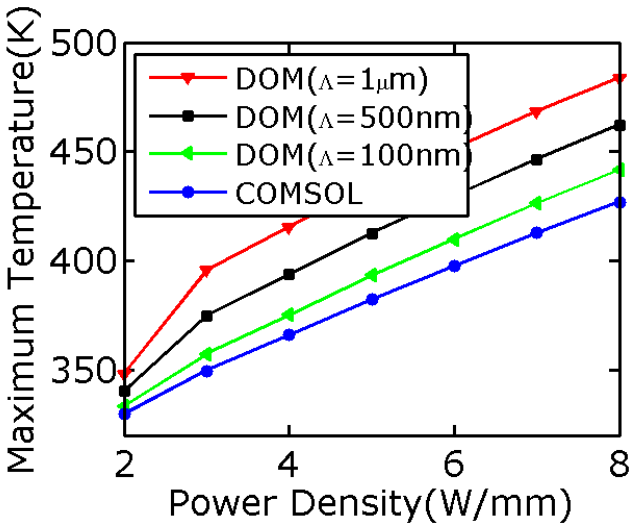

Figure 54: Maximum temperatures observed in devices after COMSOL and ballistic diffusive thermal simulations performed with Λ=100nm, 500nm, and 1μmat different power densities.

the electrical field distribution in the device and it also causes ballistic effects to be higher. Since power density was varied for each case that resulted with a change in Joule heating distribution it is difficult to determine the dominant factor responsible for the increase in ballistic effects.

6.4 Non-Gray Simulations

Non-gray simulations were performed to investigate the effect of energy decay mechanisms between the electrons and phonons on the hotspot temperature. Energy pathway for an AlGaN/GaN HFET was shown in Fig.55. According to this, the high electrical field excites the electrons and electrons transfer most of their energy to optical phonons through Fröhlich interactions. Later these optical phonons relax into other optical and acoustic phonons that move the heat away through substrate and heat sink.

In order to investigate the effect of these transitions, first the electron to phonon energy transfer, then the relaxation of energy between different phonon modes should be modeled in more detail. For this purpose, electrical simulations are performed

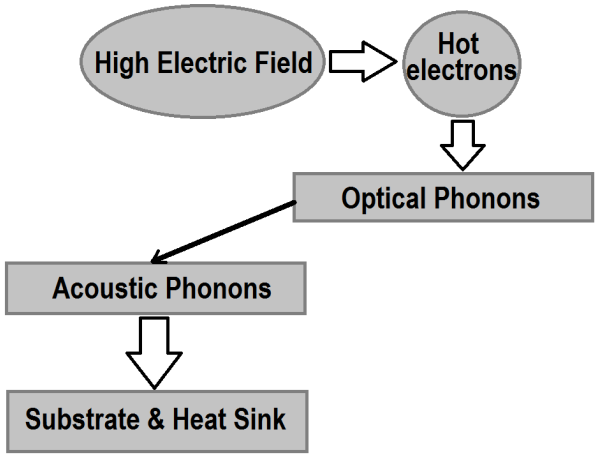

Figure 55: Energy transfer pathway for an operating AlGaN/GaN HFET.

using Monte Carlo simulations and thermal simulations are performed using non-gray multiscale methods.

6.4.1 Electrical Simulations

The hydrodynamic model is based on the moments of BTE. Specifically, zero-order moment conservation of number of particles, first order moment current continuity second moment continuity of energy and third order continuity of energy flux[113]. However, it is known that even the third moment of BTE is not suitable to give accurate results for locations where the gradients are high. Using Monte Carlo techniques, however, partly eliminates these errors. Yet it still has statistical noise associated with it. Full band ensemble Monte Carlo device simulations are performed for a device which has a shorter gate length than the previously modeled device shown in Fig.45. Figure 56 shows this device.

The electronic dispersion for wurtzite III-nitride material was calculated using the empirical pseudopotential method(EPM), for which all relevant effective masses and optical transition energies are found to be in good agreement with values derived from experiment. Electrical self consistency with charge transport was obtained through

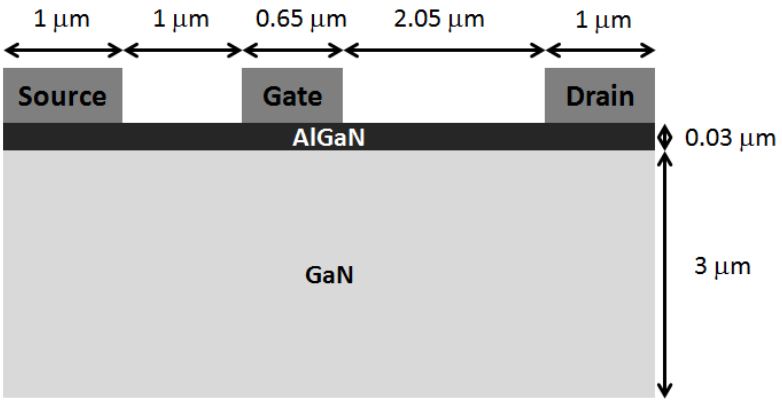

Figure 56: The schematic of the AlGaN/GaN HFET modeled using Monte Carlo Simulations.

synchronous solution of two-dimensional Poisson equation on an irregular grid, using the cloud-in-cell charge assignment scheme[114, 115]. Conduction band electrons may be accelerated or decelerated by the electric field of the device, according to the known electrostatic potential resulting in either a gain or loss of energy and crystal momentum. Similarly, interactions between electrons and phonons may result in the absorption and emission of the latter, and a commensurate gain or loss of electron energy, respectively, in addition to the exchange of crystal momentum. In our simulations, optical phonon modes were treated as dispersionless, and their occupation number was modeled with a position-dependent rate equation. Non-equilibrium phonon populations were used to calculate the strength of various scattering mechanisms in the Monte Carlo simulator.

The scattering mechanisms incorporated were: the Fröhlich and deformation potential interactions with phonons,as well as, ionized impurity scattering, piezoelectric scattering, and impact ionization, as detailed in [76]. The gain and loss of electron energy from and to the various phonon modes was calculated as a function of position within the device, and used as the driving terms for thermal transport equations. All scattering rates were computed in a manner consistent with the tabulated electronic dispersion, in the first Born approximation. The spontaneous and piezoelectric

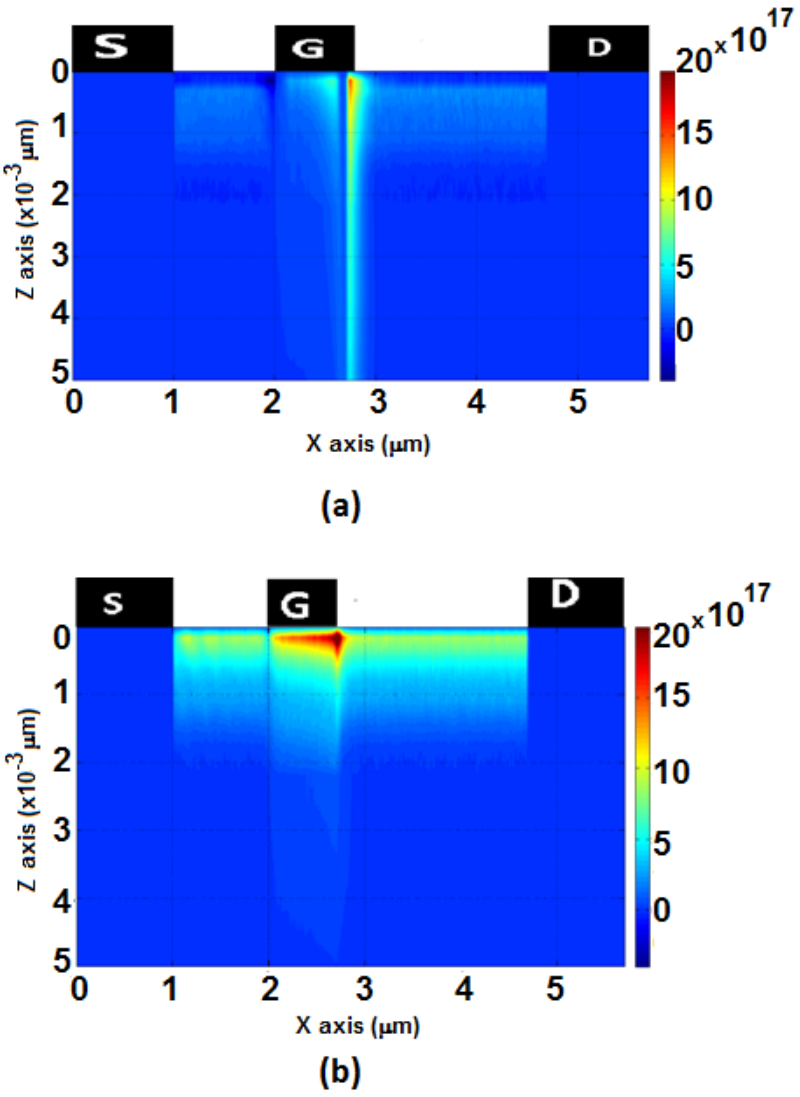

Figure 57: Spatial distribution of the net energy transfer rate (W/m^3) for the case of applied bias in the linear regime. a)VGS=1V, VDS=1.65 V and net output power of entire device 3.280 W/mm. b)VGS=-3V, VDS=5.2 V and net output power of entire device 3.223 W/mm.

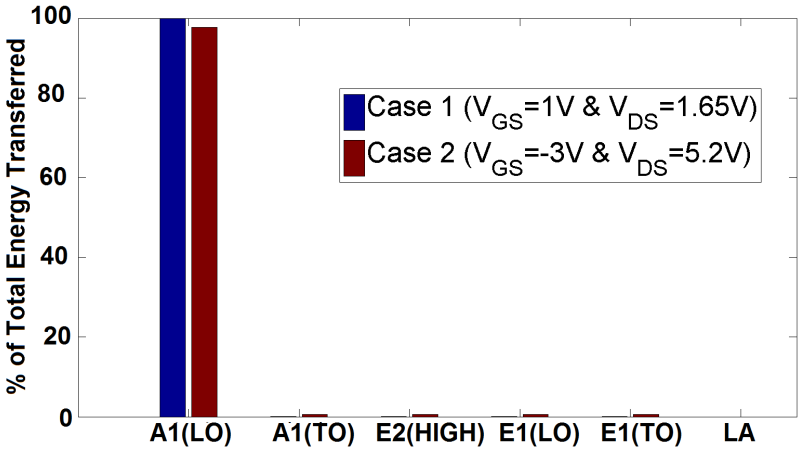

Figure 58: Percentage of the total energy transferred by electrons to different phonon modes.

charges inherent in AlGaN/GaN HFET structures were modeled based on the method outlined in [3], with more recent parameters given by [116].

Synchronous full-band ensemble Monte Carlo simulations were performed to establish the spatial distribution of the net energy transfer rate from the electron system to the phonon system in the HFET device depicted in Fig.56. Results are presented for two different bias conditions: one in the linear regime of operation (VGS=1V, VDS=1.65 V) and the other in the saturated regime (VGS=-3V and VDS=5.2V). The particular choice of bias conditions corresponds to nearly identical power dissipation in both cases, 3.280W/mm in the former, and 3.223W/mm in the latter. At each bias condition, the spatial distribution of net energy transfer rate was resolved for each distinct phonon mode separately, as the various phonons may be driven out of equilibrium with the electron system as well as from equilibrium with each other. For purposes of illustration, Fig. 57(a) and (b) show the aggregate energy transfer rates from the electron system to the phonon system when the device was biased in the saturated and linear regimes, respectively.

When biased in the saturation regime, the lateral component of the electric field underneath the drain end of the gate electrode became quite large, accelerating electrons to high energy above the conduction band edge. Just beyond the region of

this "field spike", these hot electrons transfer their energy to the crystal through the emission of phonons, via both the Fröhlich and the deformation potential interactions. This leads directly to a localized, highly non-equilibrium population of each of the phonon modes in the familiar hotspot clearly visible in Fig. 57(b), where the net energy transfer rate was greatest. Biased in the linear regime, the field spike was considerably less pronounced, and the spatial distribution of Joule heating along the channel was considerably less localized, as reflected in Fig. 57(a).

Figure 58 represents the percentage of the total energy in the active region of the HFET transferred to A1(LO),A1(TO), E2(H), E1(LO), and E1(TO) modes found at the end of Monte Carlo simulations. The highest percentage of the energy given by electrons was transferred to A1(LO) phonons. Nearly all the electron energy was transferred to A1(LO) when the device was operated under linear regime at VGS=1V. Under saturated regime (VGS=-3V) the percentage of the energy exchange from electrons to A1(LO) phonons decreased yet energy exchange to other modes such as A1(TO), E2(H), E1(LO) and E1(TO) increased.

6.4.2 Multiscale Thermal Simulations

Similar to multiscale gray models the thermal performance of a 2 finger device with SiC substrate mounted on CuW package shown in Fig. 48 is investigated this time using non-gray multiscale model. First, COMSOL simulations were performed to obtain the temperature distribution within the device and the package. Later, non-gray DOM simulations were performed at a region shown in Fig.49 with size ($L \times H = 10\mu m \times 3\mu m$)to further include the ballistic thermal effects at hotspot. The non-gray simulations were performed using 1, 3, 5, and 6 band models. In non-gray simulations Joule heating distribution to different phonon modes which is shown in Fig.58 was taken into account.

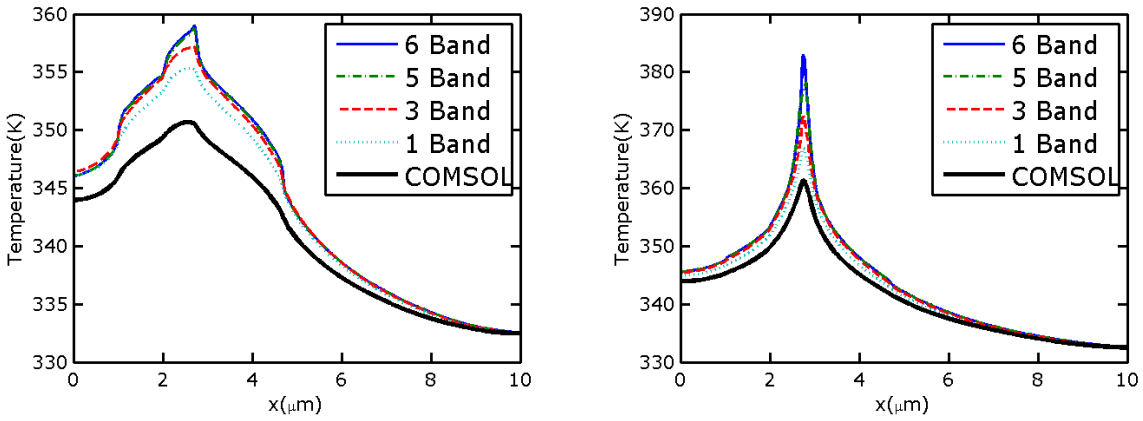

Figure 59: Temperature at the surface of the HFET under an operating condition of (a)VDS=1.65 and VGS=1V (b)VDS=5.2 and VGS=-3V.

6.4.3 Results

Figures 59(a) and (b) are the temperature plots at the AlGaN/GaN interface for Cases 1 and 2 obtained using a 1,3,5, and 6 band non-gray models. In addition to temperatures obtained from the BTB FVDOM solution, temperatures obtained from the Fourier solution are also plotted in Fig. 59. The maximum temperatures obtained by the solution of the non-gray FVDOM were as much as 10K and 20K higher than the temperatures obtained using the Fourier's diffusion equation for Case 1 and 2 respectively. This is due to highly localized heat generation region around the hotspot. Such effects were reduced away from the hotspot and the Fourier and BTE solutions approached each other as can be seen in Fig.59(a) and (b). The localized heating was responsible for the non-continuum heat transport effects around the hotspot. This result emphasizes the importance of the solution of the phonon BTE instead of the continuum approach while determining heat transport at small scales or when extremely small localized heating is present in the devices.

As a higher number of bands used, the DOM temperatures were increased and converged. For example, the maximum temperature difference between a 1-band

model and COMSOL simulations was about 5K. When a higher number of bands were used, this difference increased to 10K for a device operating at VGS=1V. This is shown in Fig.59(a). In Fig.59(b) maximum temperature difference of about 6K was observed between 1-band and COMSOL results. This difference reached more than 20K when a higher number of bands were used. The reason for the higher temperatures with the BTB model was due to electron to lattice energy transfer occurring through high frequency optical phonons with low group velocities and thermal conductivity. Moreover, the difference between the COMSOL and DOM results converged when 6-bands were used. This can be observed by comparing the 5-band and 6-band results in Fig. 59(a) and (b).

We have also observed that the difference between maximum temperatures was higher when a lower gate voltage was used as a result of localization of heat. The difference between the non-continuum and continuum approaches was significantly higher in Fig.59(a) compared to Fig.59(b) since heat was more localized in Case 2 as discussed earlier.

Finally, Fig. 60(a) is the temperature contour plot obtained by 6-band non-gray FVDOM for Case 1 operating at VDS=1.65 and VGS=1V. The integrated energy generation rate in this device was equal to 3.28 W/mm. Figure 60(a) shows that the maximum temperature occurs under the gate edge on the drain side due to highly localized heat generation. The maximum temperature observed in the device was 361K for Case 1. Figure 60(b) shows the temperature distribution in a device obtained by 6-band non-gray FVDOM Case 2 operating at VDS=5.2 and VGS=-3V. The integrated energy generation rate in this device is equal to 3.22 W/mm that is very similar to the total generation of Case 1. Again the hotspot was located near the gate edge but this time the heating is more localized at the hotspot. Due to the localization and although the total energy generated in both cases are very similar, the temperatures were higher for Case 2.

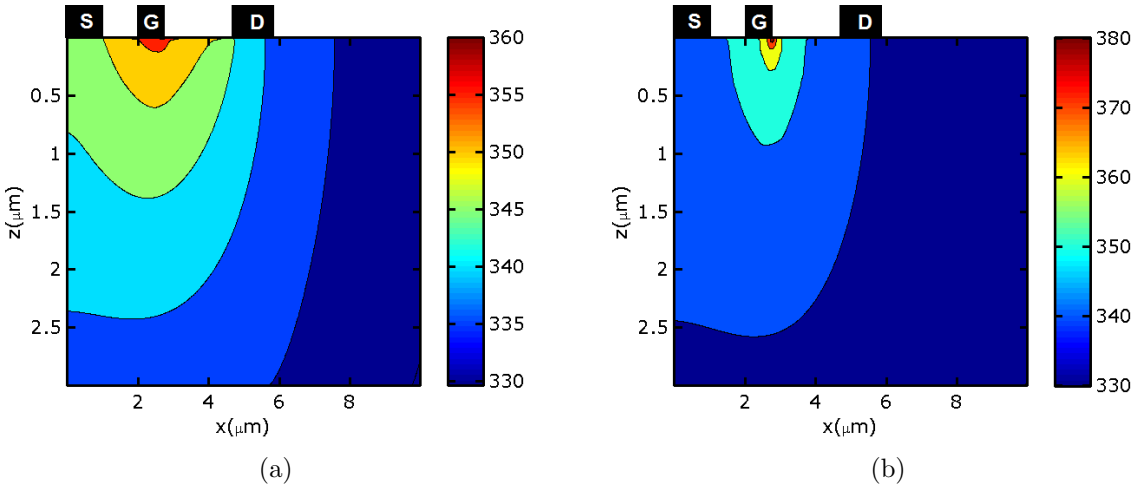

Figure 60: Temperature contour Plot of the HFET under an operating conditions of (a)VDS=1.65 and VGS=1V (b)VDS=5.2 and VGS=-3V.

With the current results it is possible to tell that the BTB approach does reveal insight into the phonon relaxation process and energy transfer within the system.

6.5 Conclusion

As a result of gray simulations the intense heating at the gate edge and the variation of temperature along the gate width were observed. Moreover the ballistic effects became more significant as the device operation power was increased due to increasing magnitude of Joule heating. Finally, it was concluded that as the mean free path of phonons increased the effects of ballistic phonon transport to hotspot temperature increased.

Non-gray simulations were performed for another device powered at constant power at two different gate voltages in linear and saturation regimes. The results show that majority of the Joule heating occurs through A1(LO) phonons through Fröhlich interactions of electrons with phonons. When the operating conditions changed outside of the linear regime, the distribution of energy transfer among different phonon modes changed as other phonon modes were excited by the electron phonon interaction process.

Another important result from the Monte Carlo simulations was the distribution of heat generation in the active region of the device. When the gate voltage was negative although the net power output and total Joule heating was the same the heat generation is more localized near the gate edge. When the generation is more localized ballistic effects become more pronounced. The temperatures obtained from the solution of non-gray DOM were higher than the temperatures obtained from COMSOL simulation. It was also suggested to use maximum 6 bands for non-gray simulations due to non-physicality of phonon group properties when higher number of bands were used. The difference between the COMSOL and DOM temperatures increases as a result of this localization effect when the gate voltage becomes negative.

CHAPTER VII

CONCLUSIONS AND FUTURE RESEARCH DIRECTIONS

7.1 Conclusions

7.1.1 Numerical Solution of Gray and Non-Gray Phonon BTE

In Chapter III, the numerical solution of the phonon BTE was discussed and two popular methods (LBM and DOM) were compared. It was shown that LBM is not a suitable method for modeling ballistic-diffusive heat transport in domains where ballistic effects are present. This was due to two reasons: an insufficient number of phonon propagation directions and inaccurate heat flux prediction in ballistic-diffusive and ballistic regimes. In the same chapter, it was shown that DOM is a better alternative since unlike LBM, the spatial and angular discretization were decoupled and an unlimited number of phonon propagation directions could be used. We suggest using DOM instead of LBM will resolve these issues and will provide better temperature and heat flux estimates in domains where ballistic effects are present. Thus, we perform hotspot modeling of AlGaN/GaN HFETs using DOM numerical solution of phonon BTE.

In Chapter IV, a non-gray phonon model was introduced. A non-gray phonon BTE model was built by discretizing the phonon dispersion into phonon bands and calculating the scattering strengths between these bands. The scattering strengths between the phonon bands were calculated considering only the 3 phonon interactions at constant temperature, $T = 300K$. Thermal properties of each band such as thermal conductivity, specific heat, and group velocity were also calculated and compared with each other. The approach considered 1 band, 3 band, and 6 band models and showed

that as the discretization of dispersion curve is performed by narrower bands the more detailed information was obtained concerning phonon modes present in GaN lattice.

7.1.2 Multiscale Thermal Model

Multiscale models are necessary to explain both the ballistic effects at the hotspot and the far field effects such as substrate, package and thermal boundary conditions. In Chapter V, a multiscale thermal model was built and its limits were discussed. It was shown that multiscale models can be used when proper attention is given to the distance of boundaries where coupling between ballistic and diffusion transport regimes exists. It was observed that ballistic effects that are present in the domain diminishes when moving away from the hotspot. It was also shown that this distance is directly correlated to mean free path of phonons.

Finally, it was suggested usage of a commercial software such as COMSOL for multiscale models should be considered since it provides flexibility such as irregular sized mesh usage, different solver types, and three-dimensional modeling features.

7.1.3 Device Simulations

Electrical and thermal device simulations were performed in Chapter VI. Unlike many previous attempts on modeling temperature of devices, the Joule heating distribution in devices was obtained by using electrical simulations such as hydrodynamic Sentaurus and Monte Carlo simulations. By using the Joule heating distribution obtained at different power densities we investigated the effect of power density on temperature of the device using gray simulations.

Moreover, by using the Joule heating distribution obtained by Monte Carlo simulations, the energy relaxation from electrons to different phonon modes of the lattice were investigated. Using this information and the non-gray model built earlier multiscale thermal simulations were also performed. Using this model, the effect of gate voltage on the hotspot temperature of the devices is investigated. It is concluded

that as the gate voltage decreases heat generation profile becomes more localized and generate more ballistic effects.

7.2 Future Research Directions

Future research directions can be listed as:

- The fundamental issue that drove this dissertation was the need to understand the magnitude of the temperature within the channel of AlGaN/GaN HFETs. At present, methods to directly measure this temperature are lacking due to the location of the hotspot being underneath the gate and source connected field plates. Current optical techniques that can be used for measurement of temperature in devices do not have the resolution to measure the temperature variations at nanometer scale. So experimental validation of hotspot temperatures are difficult. However, are still needed to both validate models such as the one developed in this dissertation in order to help with its acceptance by the broader community. This requires future developments in experimental techniques for thermal metrology in AlGaN/GaN HFETs. Detailed mean free path measurements should also be performed for the phonons in wurtzite GaN. Moreover, the temperature effects on these mean free paths should be analyzed. The results of such experiments will give a good insight for what kind of material properties should be used for phonon dynamic simulations.

- In continuum models of thermal transport in AlGaN/GaN HFETs, temperature dependent properties are used to calculate the thermal response of the devices. Such approaches are found to be necessary to predict the temperature of the devices within the transistor channel (away from the gate). This has not been explicitly done in the current study. Phonon distribution and dynamics in GaN are strong functions of temperature. At high temperatures thermal conductivity of GaN decrease due to slower relaxation of phonons. As the device hotspot

temperature increases the phonon dynamics will change as a result of this. In this study a fitting parameter called Gruneisen parameter was used to match the thermal conductivity of a non-gray model to experimental thermal conductivity. This was done because ab-initio calculations via ABINIT could not provide third order derivatives of energy and this capture the changes in phonon dynamics as a result of temperature. If the change in phonon scattering rates with respect to temperature are included in temperature more realistic device modeling will be possible.

- Up to six phonon bands have been used to study thermal performance of devices in this study. In the future, a more detailed convergence study on the effects of number of phonon bands on hotspot temperature should be performed and the minimum number of phonon bands required for different semiconductor materials should be investigated. Alternatively, since increasing the number of phonon bands increases the computational complexity of the problem, identifying the bands that do not play significant roles in the energy decay may also simplify the problem.

- Wurtzite GaN is known to have high levels of defects in its crystal structure. Additional scattering effects such as impurity and defect scattering should be included in ballistic-diffusive thermal simulations since they are expected to change the relaxation times of phonons within the lattice and change the phonon transport dynamic which will effect the hotspot temperatures.

- Currently our DOM code is limited to model one material. It is suggested to modify the model to perform multilayer simulations to investigate the effects on AlGaN/GaN interface and GaN/substrate interface on ballistic-diffusive heat transport. It is expected to see the effects of boundary scattering on the ballistic thermal transport occurring in devices.

- The one way coupling between electrical and thermal simulations used in this thesis can be used to understand the approximate hotspot temperatures of devices. However, currently these simulations can not be used to understand the electrical changes that will result from the extremely high temperatures of the hotspots. In the future, the effects of the hotspot temperature on the device performance should also be investigated.

- Device simulations should be performed for device with field plates and with gate insulators such as MOSHFETs to compare the differences in hotspot temperature due to change in electrical fields. Moreover, devices with higher number of fingers with various spacings should be modeled to understand the thermal effects that will increase with higher number and density of fingers.

APPENDIX A

SN QUADRATURES

Table 7: Directions and weights of discrete directions in the first octant of quadratures S4, S6, and S8[2].

Quadrature	Direction cosines			Weight
	μ	η	ξ	w
S_4	0.295 875 9	0.295 875 9	0.908 248 3	0.523 598 7
	0.295 875 9	0.908 248 3	0.295 875 9	0.523 598 7
	0.908 248 3	0.295 875 9	0.295 875 9	0.523 598 7
S_6	0.183 867 0	0.183 867 0	0.965 601 3	0.160 951 7
	0.183 867 0	0.695 051 4	0.695 051 4	0.362 646 9
	0.183 867 0	0.965 601 3	0.183 867 0	0.160 951 7
	0.695 051 4	0.183 867 0	0.695 051 4	0.362 646 9
	0.695 051 4	0.695 051 4	0.183 867 0	0.362 646 9
	0.965 601 3	0.183 867 0	0.183 867 0	0.160 951 7
S_8	0.142 255 5	0.142 255 5	0.979 554 3	0.171 235 9
	0.142 255 5	0.577 350 3	0.804 008 7	0.099 228 4
	0.142 255 5	0.804 008 7	0.577 350 3	0.099 228 4
	0.142 255 5	0.979 554 3	0.142 255 5	0.171 235 9
	0.577 350 3	0.142 255 5	0.804 008 7	0.099 228 4
	0.577 350 3	0.577 350 3	0.577 350 3	0.461 717 9
	0.577 350 3	0.804 008 7	0.142 255 5	0.099 228 4
	0.804 008 7	0.142 255 5	0.577 350 3	0.099 228 4
	0.804 008 7	0.577 350 3	0.142 255 5	0.099 228 4
	0.979 554 3	0.142 255 5	0.142 255 5	0.171 235 9

REFERENCES

[1] A. Venkatachalam, WT James, and S. Graham. Electro-thermo-mechanical modeling of GaN-based HFETs and MOSHFETs. *Semiconductor Science and Technology*, 26(8), 2011.

[2] WA Fiveland. The selection of discrete ordinate quadrature sets for anisotropic scattering. *ASME HTD*, 160:89–96, 1991.

[3] O. Ambacher, J. Smart, JR Shealy, NG Weimann, K. Chu, M. Murphy, WJ Schaff, LF Eastman, R. Dimitrov, and L. Wittmer. Two-dimensional electron gases induced by spontaneous and piezoelectric polarization charges in n-and Ga-face AlGaN/GaN heterostructures. *Journal of Applied Physics*, 85:3222, 1999.

[4] J. Joh, J.A. Del Alamo, U. Chowdhury, T.M. Chou, H.Q. Tserng, and J.L. Jimenez. Measurement of channel temperature in GaN high-electron mobility transistors. *Electron Devices, IEEE Transactions on*, 56(12):2895–2901, 2009.

[5] S Singhal, T Li, A Chaudhari, AW Hanson, R Therrien, JW Johnson, W Nagy, J Marquart, P Rajagopal, and JC Roberts. Reliability of large periphery GaN-on-si HFETs. *Microelectronics Reliability*, 46(8):1247–1253, 2006.

[6] P Burgaud, L Constancias, G Martel, C Savina, and D Mesnager. Preliminary reliability assessment and failure physical analysis on AlGaN/GaN HEMTs COTS. *Microelectronics Reliability*, 47(9):1653–1657, 2007.

[7] A. Sarua, H. Ji, M. Kuball, M.J. Uren, T. Martin, K.P. Hilton, and R.S. Balmer. Integrated micro-raman/infrared thermography probe for monitoring of self-heating in AlGaN/GaN transistor structures. *Electron Devices, IEEE Transactions on*, 53(10):2438–2447, 2006.

[8] J.P. Calame, R.E. Myers, F.N. Wood, and S.C. Binari. Simulations of direct-die-attached microchannel coolers for the thermal management of GaN-on-SiC microwave amplifiers. *Components and Packaging Technologies, IEEE Transactions on*, 28(4):797–809, 2005.

[9] Adam Christensen. *Multiscale Modeling of Thermal Transport in Gallium Nitride Microelectronics*. Phd thesis, Georgia Institute of Technology, 2009.

[10] GP Srivastava. The anharmonic phonon decay rate in group-iii nitrides. *Journal of Physics: Condensed Matter*, 21(17):174205, 2009.

[11] KT Tsen, DK Ferry, A. Botchkarev, B. Sverdlov, A. Salvador, and H. Morkoc. Time-resolved raman studies of the decay of the longitudinal optical phonons in wurtzite GaN. *Applied Physics Letters*, 72(17):2132–2134, 1998.

[12] S Narumanchi and J Murthy. Boltzmann transport equation-based thermal modeling approaches for hotspots in microelectronics. *Heat and mass Transfer*, 2006.

[13] S. Volz and R. Carminati. *Microscale and Nanoscale Heat Transfer*. Springer, 2007.

[14] A. Jezowski, BA Danilchenko, M. Bockowski, I. Grzegory, S. Krukowski, T. Suski, and T. Paszkiewicz. Thermal conductivity of GaN crystals in 4.2300 k range. *Solid state communications*, 128(2):69–73, 2003.

[15] N Killat, M Montes, JW Pomeroy, T Paskova, KR Evans, J Leach, X Li, U Ozgur, H Morko, and KD Chabak. Thermal properties of AlGaN/GaN HFETs on bulk GaN substrates. *Electron Device Letters, IEEE*, 33(3):366–368, 2012.

[16] Weili Liu and Alexander A Balandin. Thermal conduction in AlGaN alloys and thin films. *Journal of Applied Physics*, 97:073710, 2005.

[17] C Luo, DR Clarke, and JR Dryden. The temperature dependence of the thermal conductivity of single crystal GaN films. *Journal of Electronic Materials*, 30(3):138–146, 2001.

[18] U.K. Mishra, S. Likun, T.E. Kazior, and Y.F. Wu. GaN-based RF power devices and amplifiers. *Proceedings of the IEEE*, 96(2):287–305, 2008.

[19] L.F. Eastman and U.K. Mishra. The toughest transistor yet [GaN transistors]. *Spectrum, IEEE*, 39(5):28–33, 2002.

[20] K. Gurnett and T. Adams. Considerations for GaN-powered base stations. *III-Vs Review*, 19(7):20–22, 2006.

[21] J. Shealy, J. Smart, M. Poulton, R. Sadler, D. Grider, S. Gibb, B. Hosse, B. Sousa, D. Halchin, and V. Steel. Gallium nitride (GaN) HEMT's: progress and potential for commercial applications. pages 243–246. IEEE.

[22] J A del Alamo and J Joh. GaN HEMT reliability. *Microelectronics Reliability*, 49(9-11):1200–1206, 2009.

[23] J. Joh and J.A. del Alamo. Mechanisms for electrical degradation of GaN high-electron mobility transistors. pages 1–4. IEEE.

[24] R. Vetury, N.Q. Zhang, S. Keller, and U.K. Mishra. The impact of surface states on the dc and RF characteristics of AlGaN/GaN HFETs. *Electron Devices, IEEE Transactions on*, 48(3):560–566, 2001.

[25] R. Stoklas, D. Greguov, J. Novak, A. Vescan, and P. Kordo. Investigation of trapping effects in AlGaN/GaN/si field-effect transistors by frequency dependent capacitance and conductance analysis. *Applied Physics Letters*, 93:124103, 2008.

[26] JA Mittereder, SC Binari, PB Klein, JA Roussos, DS Katzer, DF Storm, DD Koleske, AE Wickenden, and RL Henry. Current collapse induced in AlGaN/GaN high-electron-mobility transistors by bias stress. *Applied Physics Letters*, 83:1650, 2003.

[27] J. Joh and J.A. Del Alamo. Critical voltage for electrical degradation of GaN high-electron mobility transistors. *Electron Device Letters, IEEE*, 29(4):287–289, 2008.

[28] Prashanth Makaram, Jungwoo Joh, Jess A Del Alamo, Toms Palacios, and Carl V Thompson. Evolution of structural defects associated with electrical degradation in AlGaN/GaN high electron mobility transistors. *Applied Physics Letters*, 96(23):233509–233509–3, 2010.

[29] EJ Miller, ET Yu, P. Waltereit, and JS Speck. Analysis of reverse-bias leakage current mechanisms in GaN grown by molecular-beam epitaxy. *Applied Physics Letters*, 84:535, 2004.

[30] K. Wang, J. Simon, N. Goel, and D. Jena. Optical study of hot electron transport in GaN: Signatures of the hot-phonon effect. *Applied Physics Letters*, 88(2):022103–022103–3, 2006.

[31] M.A. Khan, G. Simin, J. Yang, J. Zhang, A. Koudymov, M.S. Shur, R. Gaska, X. Hu, and A. Tarakji. Insulating gate iii-n heterostructure field-effect transistors for high-power microwave and switching applications. *Microwave Theory and Techniques, IEEE Transactions on*, 51(2):624–633, 2003.

[32] M. Marso, G. Heidelberger, K.M. Indlekofer, J. Bernaat, A. Fox, P. Kordos, and H. Luth. Origin of improved RF performance of AlGaN/GaN MOSHFETs compared to HFETs. *Electron Devices, IEEE Transactions on*, 53(7):1517–1523, 2006.

[33] A. Ashok, D. Vasileska, O.L. Hartin, and S.M. Goodnick. Electrothermal monte carlo simulation of GaN HEMTs including electronelectron interactions. *Electron Devices, IEEE Transactions on*, 57(3):562–570, 2010.

[34] P.B.M. Wolbert, G.K.M. Wachutka, B.H. Krabbenborg, and T.J. Mouthaan. Nonisothermal device simulation using the 2D numerical process/device simulator trendy and application to soi-devices. *Computer-Aided Design of Integrated Circuits and Systems, IEEE Transactions on*, 13(3):293–302, 1994.

[35] T. Sadi, R.W. Kelsall, and N.J. Pilgrim. Investigation of self-heating effects in submicrometer GaN/AlGaN HEMTs using an electrothermal monte carlo method. *Electron Devices, IEEE Transactions on*, 53(12):2892–2900, 2006.

[36] B. Benbakhti, A. Soltani, K. Kalna, M. Rousseau, and J.C. De Jaeger. Effects of self-heating on performance degradation in AlGaN/GaN-based devices. *Electron Devices, IEEE Transactions on*, 56(10):2178–2185, 2009.

[37] ER Heller and A. Crespo. Electro-thermal modeling of multifinger AlGaN/GaN HEMT device operation including thermal substrate effects. *Microelectronics Reliability*, 48(1):45–50, 2008.

[38] M Auf der Maur, G Romano, and A Di Carlo. Electro-thermo-mechanical simulation of AlGaN/GaN HEMTs. In *Computational Electronics (IWCE), 2012 15th International Workshop on*, pages 1–4. IEEE.

[39] Ronggui Yang and Gang Chen. Thermal conductivity modeling of periodic two-dimensional nanocomposites. *Physical Review B*, 69(19):195316, 2004.

[40] W.T. James. *Electro-thermal-mechanical modeling of GaN HFETs and MOSHFETs*. Ms thesis, Georgia Institute of Technology, 2011.

[41] MG Ancona, SC Binari, and DJ Meyer. Fully coupled thermoelectromechanical analysis of GaN high electron mobility transistor degradation. *Journal of Applied Physics*, 111(7):074504–074504–16, 2012.

[42] A. Matulionis, J. Liberis, L. Ardaravicius, M. Ramonas, I. Matulioniene, and J. Smart. Hot-electron energy relaxation time in AlGaN/GaN. *Semiconductor Science and Technology*, 17(3):L9, 2002.

[43] M. Ramonas, A. Matulionis, J. Liberis, L. Eastman, X. Chen, and Y.J. Sun. Hot-phonon effect on power dissipation in a biased AlxGaN(1-x)/AlN/GaN channel. *Physical Review B*, 71(7):075324, 2005.

[44] H. Ye, GW Wicks, and PM Fauchet. Hot electron relaxation time in GaN. *Applied Physics Letters*, 74(5):711–713, 1999.

[45] Yuan Taur, Clement H Wann, and David J Frank. 25 nm CMOS design considerations. In *Electron Devices Meeting, 1998. IEDM'98. Technical Digest., International*, pages 789–792. IEEE.

[46] PG Sverdrup, S. Sinha, M. Asheghi, S. Uma, and KE Goodson. Measurement of ballistic phonon conduction near hotspots in silicon. *Applied Physics Letters*, 78:3331, 2001.

[47] E. Pop, S. Sinha, and K.E. Goodson. Monte carlo modeling of heat generation in electronic nanostructures. In *ASME-IMECE*.

[48] Ronggui Yang, Gang Chen, Marine Laroche, and Yuan Taur. Simulation of nanoscale multidimensional transient heat conduction problems using ballistic-diffusive equations and phonon boltzmann equation. *Journal of Heat Transfer*, 127(3):298–306, 2005.

[49] Supriyo Datta. *Quantum transport: atom to transistor*. Cambridge University Press, 2005.

[50] N Mingo and Liu Yang. Phonon transport in nanowires coated with an amorphous material: An atomistic greens function approach. *Physical Review B*, 68(24):245406, 2003.

[51] W Zhang, TS Fisher, and N Mingo. The atomistic green's function method: an efficient simulation approach for nanoscale phonon transport. *Numerical Heat Transfer, Part B: Fundamentals*, 51(4):333–349, 2007.

[52] J.Y. Murthy, S.V.J. Narumanchi, J.A. Pascual-Gutierrez, T. Wang, C. Ni, and S.R. Mathur. Review of multi-scale simulation in sub-micron heat transfer. *Int. J. for Multiscale Computational Engineering*, 3:5, 2005.

[53] SVJ Narumanchi, JY Murthy, and CH Amon. Comparison of different phonon transport models for predicting heat conduction in silicon-on-insulator transistors. *Journal of Heat Transfer*, 127:713, 2005.

[54] JM Ziman. *Electrons and Phonons*. Clarendon Press, Oxford, 2001.

[55] D. Singh. *Frequency and polarization resolved phonon transport in carbon and silicon nanostructures*. Phd thesis, Purdue University, 2011.

[56] S. Sinha, E. Pop, RW Dutton, and KE Goodson. Non-equilibrium phonon distributions in sub-100 nm silicon transistors. *Journal of Heat Transfer*, 128:638, 2006.

[57] B. Benbakhti, M. Rousseau, A. Soltani, and J.C. De Jaeger. Analysis of thermal effect influence in gallium-nitride-based tlm structures by means of a transport and thermal modeling. *Electron Devices, IEEE Transactions on*, 53(9):2237–2242, 2006.

[58] B. Benbakhti, M. Rousseau, A. Soltani, J. Laureyns, and J.C. De Jaeger. Thermal behaviour of gate-less AlGaN/GaN heterostructures. pages 104–107. IEEE.

[59] A.M. Darwish, A.J. Bayba, and H.A. Hung. Thermal resistance calculation of AlGaN-GaN devices. *Microwave Theory and Techniques, IEEE Transactions on*, 52(11):2611–2620, 2004.

[60] F. Bertoluzza, N. Delmonte, and R. Menozzi. Three-dimensional finite-element thermal simulation of GaN-based HEMTs. *Microelectronics Reliability*, 49(5):468–473, 2009.

[61] D. Vasileska and S.M. Goodnick. Computational electronics. *Materials Science and Engineering: R: Reports*, 38(5):181–236, 2002.

[62] A. Asgari, M. Kalafi, and L. Faraone. A quasi-two-dimensional charge transport model of AlGaN/GaN high electron mobility transistors (HEMTs). *Physica E: Low-dimensional Systems and Nanostructures*, 28(4):491–499, 2005.

[63] B. Jogai, JD Albrecht, and E. Pan. Effect of electromechanical coupling on the strain in AlGaN/GaN heterojunction field effect transistors. *Journal of Applied Physics*, 94:3984, 2003.

[64] F. Sacconi, A. Di Carlo, P. Lugli, and H. Morkoc. Spontaneous and piezoelectric polarization effects on the output characteristics of AlGaN/GaN heterojunction modulation doped fets. *Electron Devices, IEEE Transactions on*, 48(3):450–457, 2001.

[65] Synopsys. *Sentaurus Device User Guide, Version A-2008.09*. Synopsys Inc.

[66] M. Rousseau, JD Delemer, JC De Jaeger, and F. Dessenne. Two-dimensional hydrodynamic model including inertia effects in carrier momentum for power millimetre-wave semi-conductor devices. *Solid-State Electronics*, 47(8):1297–1309, 2003.

[67] N. Braga, R. Mickevicius, R. Gaska, X. Hu, MS Shur, M.A. Khan, G. Simin, and J. Yang. Simulation of hot electron and quantum effects in AlGaN/GaN heterostructure field effect transistors. *Journal of Applied Physics*, 95:6409, 2004.

[68] WD Hu, XS Chen, ZJ Quan, CS Xia, W. Lu, and PD Ye. Self-heating simulation of GaN-based metal-oxide-semiconductor high-electron-mobility transistors including hot electron and quantum effects. *Journal of Applied Physics*, 100:074501, 2006.

[69] WD Hu, XS Chen, ZJ Quan, XM Zhang, Y. Huang, CS Xia, W. Lu, and PD Ye. Simulation and optimization of GaN-based metal-oxide-semiconductor high-electron-mobility-transistor using field-dependent drift velocity model. *Journal of Applied Physics*, 102:034502, 2007.

[70] G Baccarani and MR Wordeman. An investigation of steady-state velocity overshoot in silicon. *Solid-State Electronics*, 28(4):407–416, 1985.

[71] C. Jacoboni and L. Reggiani. The monte carlo method for the solution of charge transport in semiconductors with applications to covalent materials. *Reviews of Modern Physics*, 55(3):645, 1983.

[72] C. Jacoboni and P. Lugli. *The Monte Carlo method for semiconductor device simulation*, volume 3. Springer Verlag, 1989.

[73] K. Hess. *Monte Carlo device simulation: full band and beyond*. Springer, 1991.

[74] J.D. Albrecht, P.P. Ruden, S.C. Binari, and M.G. Ancona. AlGaN/GaN heterostructure field-effect transistor model including thermal effects. *Electron Devices, IEEE Transactions on*, 47(11):2031–2036, 2000.

[75] T. Sadi, R.W. Kelsall, and N.J. Pilgrim. Electrothermal monte carlo simulation of submicron wurtzite GaN/AlGaN HEMTs. *Journal of Computational Electronics*, 6(1):35–39, 2007.

[76] S. Sridharan, A. Venkatachalam, and PD Yoder. Electrothermal analysis of AlGaN/GaN high electron mobility transistors. *Journal of Computational Electronics*, 7(3):236–239, 2008.

[77] K. Raleva, D. Vasileska, S.M. Goodnick, and M. Nedjalkov. Modeling thermal effects in nanodevices. *Electron Devices, IEEE Transactions on*, 55(6):1306–1316, 2008.

[78] F.N. Donmezer, D. Singh, W. James, A. Christensen, S. Graham, and J.Y. Murthy. Lattice boltzmann and discrete ordinates methods for phonon transport modeling: A comparative study. In *ASME-IMECE*.

[79] A Christensen and S Graham. Multiscale lattice boltzmann modeling of phonon transport in crystalline semiconductor materials. *Numerical Heat Transfer*, 2010.

[80] A. Nabovati, D.P. Sellan, and C.H. Amon. On the lattice boltzmann method for phonon transport. *Journal of Computational Physics*, 2011.

[81] D.A. Wolf-Gladrow. *Lattice-gas cellular automata and lattice Boltzmann models: an introduction*. Springer Verlag, 2000.

[82] W. Zhang and TS Fisher. Application of the lattice-boltzmann method to sub-continuum heat conduction. In *ASME-IMECE*. ASME.

[83] R.A. Escobar and C.H. Amon. Lattice boltzmann modeling of the thermal response of silicon-on-insulator transistors under joule heating including phonon dispersion. ASME.

[84] R. Escobar, B. Smith, and C. Amon. Lattice boltzmann modeling of subcontinuum energy transport in crystalline and amorphous microelectronic devices. *Journal of electronic packaging*, 128:115, 2006.

[85] H. Xi, G. Peng, and S.H. Chou. Finite-volume lattice boltzmann method. *Physical Review E*, 59(5):6202, 1999.

[86] Gang Chen. Thermal conductivity and ballistic-phonon transport in the cross-plane direction of superlattices. *Physical Review B*, 57(23):14958, 1998.

[87] C.H. Liu, K.H. Lin, H.C. Mai, and C.A. Lin. Thermal boundary conditions for thermal lattice boltzmann simulations. *Computers and Mathematics with Applications*, 59(7):2178–2193, 2010.

[88] S. Chandrasekhar. *Radiative transfer*. Dover Pubns, 1960.

[89] KD Lathrop and BG Carlson. Discrete ordinates angular quadrature of the neutron transport equation. Technical report, Los Alamos Scientific Lab., N. Mex., 1964.

[90] M.F. Modest. *Radiative heat transfer*. Academic Pr, 2003.

[91] S. Jendoubi, H. Lee, and R. Kim. Discrete ordinates solutions for radiatively participating media in a cylindrical enclosure. *Journal of thermophysics and heat transfer*, 7(2):213–219, 1993.

[92] AA Joshi and A Majumdar. Transient ballistic and diffusive phonon heat transport in thin films. *Journal of Applied Physics*, 74:31, 1993.

[93] KD Lathrop. The early days of the Sn method. 1992.

[94] JY Murthy and SR Mathur. Computation of sub-micron thermal transport using an unstructured finite volume method. *Journal of Heat Transfer*, 124:1176, 2002.

[95] Harvey S Price, Richard S Varga, and Joseph E Warren. Application of oscillation matrices to diffusion-convection equations. *J. Math. Phys*, 45(3):303–311, 1966.

[96] SVJ Narumanchi, JY Murthy, and CH Amon. Submicron heat transport model in silicon accounting for phonon dispersion and polarization. *Journal of Heat transfer*, 126:946, 2004.

[97] Jiyuan Tu, Guan Heng Yeoh, and Chaoqun Liu. *Computational fluid dynamics: a practical approach*. Butterworth-Heinemann, 2007.

[98] BP Leonard. A stable and accurate convective modelling procedure based on quadratic upstream interpolation. *Computer methods in applied mechanics and engineering*, 19(1):59–98, 1979.

[99] J.C. Chai, H.O.S. Lee, and S.V. Patankar. Ray effect and false scattering in the discrete ordinates method. *Numerical Heat Transfer, Part B Fundamentals*, 24(4):373–389, 1993.

[100] G.P. Srivastava. *The physics of phonons*. Taylor and Francis, 1990.

[101] Xavier Gonze. A brief introduction to the abinit software package. *Zeitschrift fr Kristallographie*, 220(5/6/2005):558–562, 2005.

[102] Xavier Gonze, B Amadon, P M Anglade, J M Beuken, F Bottin, P Boulanger, F Bruneval, D Caliste, R Caracas, and M Cote. Abinit: First-principles approach to material and nanosystem properties. *Computer Physics Communications*, 180(12):2582–2615, 2009.

[103] Y. Saad and M.H. Schultz. Gmres: A generalized minimal residual algorithm for solving nonsymmetric linear systems. *SIAM J. Sci. Stat. Comput.*, 7(3):856–869, 1986.

[104] Zyad Hassan, Nicholas Allec, Li Shang, Robert P Dick, Vishak Venkatraman, and Ronggui Yang. Multiscale thermal analysis for nanometer-scale integrated circuits. *Computer-Aided Design of Integrated Circuits and Systems, IEEE Transactions on*, 28(6):860–873, 2009.

[105] F.N. Donmezer, W. James, and S. Graham. The thermal response of gallium nitride HFET devices grown on silicon and SiC substrates. *ECS Transactions*, 41(6):13, 2011.

[106] FP Incropera and DP De Witt. Introduction to heat transfer, 1990.

[107] WS Tan, PA Houston, PJ Parbrook, G Hill, and RJ Airey. Comparison of different surface passivation dielectrics in AlGaN/GaN heterostructure field-effect transistors. *Journal of Physics D: Applied Physics*, 35(7):595, 2002.

[108] LS Yu, DJ Qiao, QJ Xing, SS Lau, KS Boutros, and JM Redwing. Ni and ti schottky barriers on n-AlGaN grown on SiC substrates. *Applied Physics Letters*, 73(2):238–240, 1998.

[109] Z Li and Richard C Bradt. Thermal expansion of the hexagonal (4h) polytype of SiC. *Journal of Applied Physics*, 60(2):612–614, 1986.

[110] Philip M Fabis. Reliability of radio frequency/microwave power packages: the effects of component materials and assembly processes. *Microelectronics Reliability*, 39(8):1265–1274, 1999.

[111] Andrea Chen and Randy Lo. *Semiconductor Packaging: Materials Interaction and Reliability*. CRC PressI Llc, 2011.

[112] A. Sarua, H. Ji, KP Hilton, DJ Wallis, M.J. Uren, T. Martin, and M. Kuball. Thermal boundary resistance between GaN and substrate in AlGaN/GaN electronic devices. *Electron Devices, IEEE Transactions on*, 54(12):3152–3158, 2007.

[113] Carlo Jacoboni. *Theory of Electron Transport in Semiconductors: A Pathway from Elementary Physics to Nonequilibrium Green Functions*, volume 165. Springer, 2010.

[114] Charles K Birdsall and Dieter Fuss. Clouds-in-clouds, clouds-in-cells physics for many-body plasma simulation. *Journal of Computational Physics*, 3(4):494–511, 1969.

[115] S.E. Laux. On particle-mesh coupling in monte carlo semiconductor device simulation. *Computer-Aided Design of Integrated Circuits and Systems, IEEE Transactions on*, 15(10):1266–1277, 1996.

[116] J. Piprek, Z.M. Li, R. Farrell, S.P. DenBaars, and S. Nakamura. *Electronic Properties of InGaN/GaN Vertical Cavity Lasers*. Wiley Online Library, 2007.